A QUEST for BEC : An all optical alternative

A THESIS

Presented to

The Academic Faculty

By

Murray D. Barrett

in Partial Fulfillment

of the Requirements for the Degree

Doctor of Philosophy in Physics

Georgia Institute of Technology

May 2002

Summary

This dissertation describes investigations into optical dipole traps formed using a high power CO_2 laser beam, culminating in the first creation of a Bose-condensate by all optical means. CO_2 lasers are ideally suited to the task of atom trapping since their extreme detuning results in a trapping field that is independent of the internal state of the atom with a practically negligible scattering of the trapping light. These traps are then ideal candidates for achieving Bose-condensation as there is little or no intrinsic heating from the trapping beams themselves.

In this work it was found that high densities and phase space densities could be easily established in these traps, giving rise to the possibility of evaporative cooling to the BEC transition. To achieve this a trap was made in which it was possible to achieve densities an order of magnitude higher than previously obtained by others in the field. Bose-condensation is achieved by subsequent forced evaporation in which the highest energy atoms are removed from the trap by adiabatically lowering the trap depth. As the technique involves the most basic of laser cooling and trapping methods, it provides a simple alternative to achieving BEC, and is currently the only alternative to the standard recipe used in magnetic traps today.

Acknowledgments

I would like to take this opportunity to thank the people who have inspired and supported me throughout this endeavour. Their support and encouragement has given me the resolve to endure this undertaking and for this I am eternally grateful.

First, I would like to thank my supervisor Dr. Mike Chapman for allowing me the opportunity of working in his laboratory. The experiences and opportunities he has provided in my time at Georgia Tech will live long in my memories. I am grateful for the tolerance and patience he has shown, and know that my respect for his leadership is well deserved.

Next I would like to extend my gratitude to Professor Brian Kennedy. If it were not for his encouragement and wisdom I would not have seen this thesis to an end, and for this I am forever in his debt. His ability and willingness to discuss a variety of physics has been an inspiration to me, and I feel privileged to have learned from him.

I would also like to thank the many people involved in the arduous and often unrewarding work involved in readying a lab for scientific research. When I started in the lab myself and fellow students Frank Casanova, Jan Leisner and Aparna Prasad Shreenath were faced with bare optics tables and empty shelves and I am grateful to have known and worked with these people in transforming the laboratory into what it has become. I am also grateful to those students who have more direct involvement in the experiments discussed in this thesis, particularly David Zhu, Jacob Sauer and Lily Yang.

I also wish to thank Dr. Li You for a number a stimulating discussions, and for guidance and advice he has given on the more theoretical perspectives involved in this work. I am also indebted to Su Yi for the numerical simulations he has done. These simulations have provided useful insights to the experiments and would not have been available to me were it not for the effort he has given.

On a more personal note I would like to thank my parents Jean and Bernard Barrett and my in-laws Sue and Paul Bonsey for their love and support in all my endeavors through life. In particular I am indebted to Sue for providing a vital ingredient to the writing of

this thesis - Golden Syrup! Ice cream will never be the same again!

Finally, and most importantly I would like to thank my wife Nicola Barrett as her contribution to this endeavor cannot be over-emphasized. She has stood by me in my darkest moments and provided me unyielding support in times of greatest despair and self doubt. She has been my harshest critic, greatest fan, my very best friend and best part of my life. I am happy to have her by my side as we journey through life together and owe her more than she could know. To her I dedicate this work in acknowledgement of her dedication to our marriage.

Murray D. Barrett

Georgia Institute of Technology
May 2002

Table of Contents

List of Figures

Chapter 1

Introduction

The first observation of Bose-Einstein condensates (BEC) in dilute atomic vapors in 1995 [4],[13], [25] has stimulated a tremendous volume of experimental and theoretical work in this field. Condensates are now routinely created in over 30 laboratories around the world, and the pace of theoretical progress is equally impressive [20]. However, the recipe for forming a BEC remains unchanged. The atomic vapor is first pre-cooled using laser cooling techniques to sub-mK temperatures and then transferred to a magnetic trap. Further cooling to BEC is then achieved by evaporative cooling induced by energy selective spin transitions. Well impressive the technique is typically slow requiring background limited lifetimes measured in minutes. This places stringent requirements on the vacuum and a high degree of isolation of the system from stray rf and optical fields. It is thus desirable to have an alternative rapid technique for producing BEC so as to relax these conditions.

All optical methods of reaching the BEC phase transition have been pursued since the early days of laser cooling. Despite the impressive developments made in this field beyond the limits set by Doppler cooling, including polarization gradient cooling [59], velocity selective coherent population trapping [6] , Raman cooling [48], [24], [55] and evaporative cooling in optical dipole traps [1], [39] the best efforts, excluding the results in this thesis, fall short of the BEC transition by an order of magnitude [45]. The principle hurdle bottlenecking progress is in the fact the laser cooling seems to be an inherently density limited process, limited by reabsorption of scattered radiation and photo-associative two-body inelastic collisions. These limitations render laser cooling techniques ineffective at the high densities needed to achieve BEC and give unfavorable starting conditions for evaporative cooling.

When laser cooling into a trap one cannot, indeed should not, neglect the dynamics

of the gas itself particularly when the collision rates between atoms is large. When the trap geometry is non-trivial this is particularly important and one needs to consider the consequences of thermalization as the initial distribution, defined by the loading process, relaxes to a thermal distribution appropriate to the trap. To some extent the importance of this equilibrium process and the importance of strongly deformed traps was touched upon by two experiments by Wolfgang Ketterle's group. In the first experiment [68] a non-equilibrium distribution of atoms was created from which condensation was observed during the subsequent relaxation of the system. In the second experiment [81] a dimple was formed in a cold atomic sample and reversible formation of a condensate was observed. The technique described in this thesis can be considered as a variation of this research. A laser cooled sample is allowed to relax into a strongly deformed trap giving rise to densities considered beyond the reach of laser cooling techniques. These densities allow for subsequent evaporation to BEC in just 2 seconds - currently the fastest method available today and the only alternative to a magnetic trap.

1.1 A brief history

To begin this thesis I start with a brief review of some of the key advances made in the field of laser cooling and trapping. The review is by no means extensive. Its purpose is to illustrate the rapid progress made in this area of research and to give some perspective as to the simplicity of the techniques used in this thesis. More extensive reviews on these topics can be found elsewhere. For laser cooling see [93],[57],[83], for optical lattices see [47], and for optical dipole traps see [37].

In 1986 Steve Chu *et al* demonstrated the first optically confined atoms, trapping a mere 500 hundred atoms loaded from optical molasses. Well a proof of principle, the result was hardly impressive or useful and it was the MOT, first demonstrated in 1987 [75], which gave a readily available large, dense source of cold atoms. This trap provided both trapping and damping forces and proved to be extremely robust, achieving large numbers ($\sim 10^7$), high densities ($\sim 10^{11}/\mathrm{cm}^3$) and sub millikelvin temperatures over a wide range of experimental parameters. Later investigations showed that collision induced losses were

a limiting factor for the MOT [79]. With high intensity trapping beams these losses were dominated by ground-excited-state collisions, whereas the low intensity limit was dominated by hyperfine changing collisions between two ground state atoms. Being density dependent, these loss mechanisms limited the attainable densities to $\sim 10^{11}/\mathrm{cm}^3$. A second limitation was found to be reabsorption of scattered radiation or radiation trapping which gives rise to repulsive forces between atoms [89]. The effect of these mechanisms could be reduced by shelving atoms in a hyperfine ground state which does not interact with the light field. Using this technique, researchers could increase densities by an order of magnitude to $\sim 10^{12}/\mathrm{cm}^3$ [50], being ultimately limited by the same mechanisms present in a normal MOT.

In the earliest days of laser cooling the cooling force was understood to be a Doppler mechanism by which the Doppler shift seen by a moving atom gave rise to a velocity dependent or friction force. Theoretically this gave a limit to the obtainable temperature satisfying $k_b T_D = \hbar\Gamma/2$. This theory was shown to be inadequate when temperatures far below this limit were observed [59]. The mechanisms responsible for this result were later shown to be a consequence of the multi-level structure of the atom [22], [17], [58], [91], [88] which was largely ignored by the Doppler theory. The essential idea was that optical pumping between state dependent micro-potentials gave rise to a Sisyphus type effect. Kinetic energy is first converted to potential energy, through the motion of the atom, and subsequently removed by the scattered radiation via optical pumping.

Since the discovery of sub-Doppler cooling mechanisms, much progress has been made in this field. Free space raman cooling [48],[24] and velocity selective coherent population trapping [6] have been used to cool atoms below the single photon recoil limit. Raman cooling in an optical dipole trap [55] has yielded a 300-fold increase in phase space density. Resolved side band cooling, first demonstrated on a single trapped Beryllium ion [70], has been used to achieve phase-space densities of 1/30 [40]. The level of sophistication reached is best illustrated by the experiment reported in [39]. In this experiment atoms, which are first transiently compressed in MOT, are transferred to a 1-D Far Off Resonant Lattice (FORL). After the untrapped atoms have fallen away the 1-D FORL is converted to a 3-D FORL in which polarization gradient cooling is then implemented. The atoms are then optically pumped to the lowest hyperfine state and a magnetic field to counter

gravity is switched on. The atoms are then adiabatically released into a very shallow cross beam trap. Once in this trap a zoom-type optical set up is used to change the trap size dynamically to compress the sample. In this way researchers were able to achieve phase-space densities of 0.001[1]. It is worth noting that we achieve similar results by loading a cross beam trap directly from the MOT, although the additional sophistication does give an order of magnitude improvement in the number of atoms obtained.

In addition to experimental advances a number of theoretical works are also worth noting. Laser cooling methods for trapped ions are reported in [18], and [66] and similar treatments more applicable to neutral atoms are given in [85]. Ground state cooling methods which utilize dark states decoupled from the light field are discussed in [27] and a side band cooling scheme is given in [69] which operates outside the usual Lambe-Dicke limit. In addition to cooling schemes the limitation imposed by reabsorption of scattered radiation is addressed in [19], and [15]. The basic idea is that by using strongly deformed traps and reducing the scattering rate to below the trap oscillation frequencies reabsorption would be strongly suppressed. This regime, referred to as the *festina lente* limit, was experimentally confirmed as reported in [94]. Limitations imposed by technical sources of heating have also been discussed in [8],[76],[34].

Despite the advances made in this field little or no consideration has been given to the dynamics of atom-trap systems particularly to the relaxation of trapped distributions, imposed by the loading technique, to a Boltzmann distribution appropriate to the trap. Emphasis has always been on the loading and cooling process or on the fundamental and technical limitations relevant to the various systems. Typically the trapping system is chosen for convenience or to compliment the cooling technique. By choosing a geometry in which high densities are a natural consequence of the relaxation process, it is possible to bypass many of the problems encountered in laser cooling today. Indeed the efforts reported in this thesis achieve densities that are an order of magnitude higher than any other reported effort, and it utilizes only the most basic of sub-Doppler cooling methods. It will be argued that this achievement is not through some fortuitous choice of atom and trap combination or meticulous attention to detail but to the fundamental redistribution process

[1] subsequent evaporation lead to phase space densitites of 0.1

that must occur after loading if Mother Nature's desires for a Boltzmann distribution are to be fulfilled.

1.2 Organization of this thesis

In the following chapters I describe the work done in my four years at Georgia Tech under the supervision of Dr. Michael Chapman. My principle focus was in the investigation of dipole force traps derived from a high power CO_2 laser. This work showed that atoms could be trapped at very high densities with extraordinary ease and, through subsequent evaporation, Bose-Condensation could be achieved in a purely optical system: a highly sought after result since the earliest days of atom trapping and laser cooling. In the following chapters I discuss the physics involved, the machine that was built and the experiments that led to this result.

In Chapter 2 I begin with a discussion of the physics which is naturally separated into three sections. The first section deals with the trapping techniques involved. Specifically I discuss the principles of the magneto-optic trap and the optical dipole force trap. The second section concerns laser cooling and a brief description of both doppler and sub-doppler cooling mechanisms is given. Finally the chapter concludes with a discussion of evaporative cooling which is the standard technique used to create BEC.

Chapter 3 focuses on the technical aspects of the experiment, beginning with the stabilization and control of the diode lasers used for cooling and probing. This is followed by sections discussing the implementation of the dipole force traps which, in turn, is followed by a discussion of loading and alignment of the system. The chapter is concluded with a description of the diagnostic techniques, specifically of the imaging, from which number and temperature is obtained, and of parametric excitation, which is used to determine trapping frequencies.

Chapters 4 and 5 are devoted to the experiments themselves. In chapter 4 the initial investigations are discussed which involved a single focus and 1-D lattice trap. Also included is a 3-D lattice system which initiated these investigations. The results obtained from these trapping geometries led to the cross beam geometry in which BEC was finally achieved. Chapter 5 is devoted to this trap.

This thesis is concluded by chapter 6 in which I summarize my work, making some suggestions in regards to improvements to the current system and to future directions that this research may lead to.

Chapter 2

Background

For all of the trap geometries considered in this thesis the basic loading procedure is the same. Atoms are first collected in a magneto-optic trap, more commonly referred to as a MOT, and transferred via laser cooling into a CO_2 laser trap with subsequent thermalization and evaporation determining the final temperatures obtained. In this chapter we review the physics behind the key ingredients of this seemly simple recipe with special emphasis on those aspects most relevant to our system. This discussion is naturally divided into three sections. The first section deals with the trapping aspects in which we discuss the MOT and the optical dipole trap. The second deals with the laser cooling processes and the third section involves evaporation.

2.1 Trapping

2.1.1 The MOT

The most widely used trap for neutral atoms is the magneto-optic trap (MOT) which was first demonstrated in 1987 [75]. It has proven to be an extremely robust and versatile trap in that its operation is somewhat insensitive to the degree of polarization and alignment of the light fields. Providing both cooling and trapping forces simultaneously, the MOT can be loaded directly from a room temperature vapor, and the light required can typically be provided by low cost diode lasers [1]. The MOT is thus a simple inexpensive method to produce dense atomic samples with temperatures below 1 mK. In this section we discuss the basic principles on which the MOT operates, its principle limitations, and the considerations that go into its set up.

[1] This is true for all the alkalis with the exception of sodium

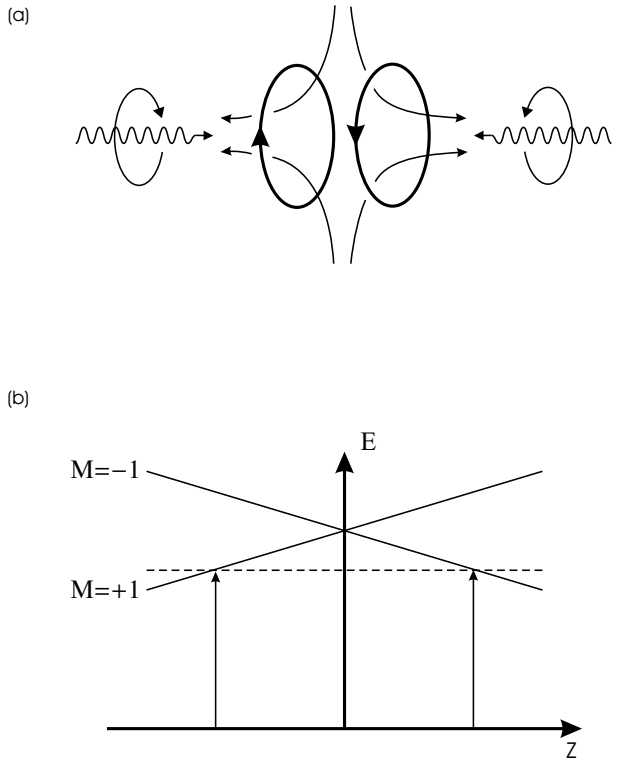

Figure 2.1: (a) 1-D MOT. (b) Energy levels in the spatially varying field

The principle behind the operation of the MOT is most easily explained for the 1-D configuration illustrated in Fig 2.1. Two counter-propagating beams of opposite helicity drive a $J = 0 \rightarrow J = 1$ transition in the presence of a magnetic quadrupole field which Zeeman shifts the excited state energy levels as shown in Fig 2.1. The beams are both red detuned with respect to the zero field resonances as shown. Because of the Zeeman shift, an atom displaced from the center scatters light preferentially from the beam directed towards the origin giving rise to a net force towards the origin. In addition a moving atom experiences a Doppler shift which results in a velocity dependent force that opposes the motion of the atom (we discuss this further in a later section). In the low intensity limit the net force on an atom is simply the sum of the forces from the individual beams. Writing the Zeeman frequency shift as $\omega_z = \beta z$, the net force can be written as

$$F = \frac{\hbar k \Gamma}{2} \left(\frac{s_0}{1 + s_0 + 4(\delta_- / \Gamma)^2} - \frac{s_0}{1 + s_0 + 4(\delta_+ / \Gamma)^2} \right) \tag{2.1}$$

where the detuning $\delta_\pm$ is given by $\delta_\pm = \delta \pm (kv + \beta z)$, $s_0 = I/I_s$ is the saturation parameter and Γ is the transition linewidth. In the limit of small velocities and small Zeeman shifts the force is given by the approximate expression

$$F(v,z) = \frac{4\hbar k s_0 (2\delta/\Gamma)(kv + \beta z)}{(1 + s_0 + (2\delta/\Gamma)^2)^2} \tag{2.2}$$

and thus the motion is that of a damped harmonic oscillator. Typical values used in experiments give trap frequencies of a few kHz and damping rates of a few hundred kHz so that the motion is over-damped.

The scheme can be readily extended to 3-D by using 2 additional beam pairs to provide confinement in the other two dimensions. For multilevel atoms the situation is somewhat more complicated but the basic mechanism remains the same. In Fig 2.2 we show the relevant part of the level structure for ^{87}Rb. Cooling and trapping is achieved using the $F_g = 2 \rightarrow F_e = 3$ transition. Atoms scattering mainly σ_+ light are optically pumped to the $m_g = 2$ substate which forms a closed system with the $m_e = 3$ substate. In practice however, off resonant excitation from $F_g = 2 \rightarrow F_e = 2$ leads to a loss of atoms to the $F_g = 1$ state. Since the ground state hyperfine splitting is large ($\sim$ 6.8GHz), atoms in this state are no longer cooled and trapped. For this reason an additional repump laser tuned to the $F_g = 1 \rightarrow F_e = 2$ is needed to sweep the atoms back into the cooling cycle. The number of atoms captured by the MOT depends on the size, intensity and detuning of the trapping beams and on the strength of the magnetic field gradient. A reasonably in-depth study on the dependence of these parameters can be found in [63]. In [35] it is shown that the number of trapped atoms increases with the fourth power of the beam diameter and shows a much less dramatic increase with intensity. Thus for a given power it is much better to use larger beams even if the intensity is somewhat less than optimal. In our system the beams are limited to a diameter of 2 cm and the beam power limits the intensity to 8 mW/cm^2 $\simeq 5 I_s$ where I_s is the saturation intensity. In this configuration the optimal number of atoms is obtained with a detuning of 15 MHz and an estimated field gradient of 7.4 G/cm. The estimate is based on the known current and geometry of the coils so is only accurate to about 40%.

Although a large number of atoms can be trapped in a MOT, the density is generally limited to $\sim 10^{11}$atoms/cm^3. The principle mechanisms responsible for this limitation

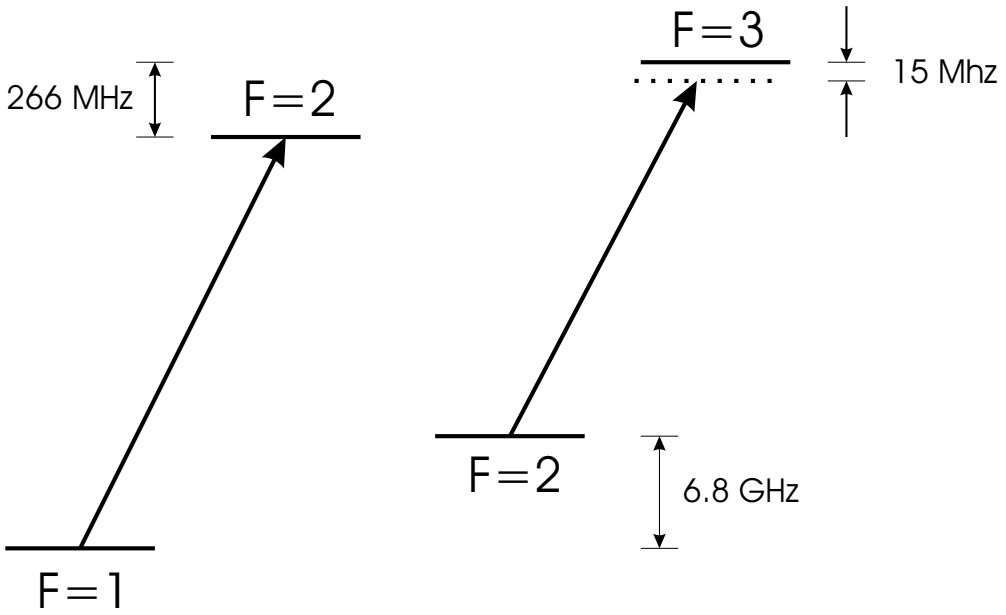

Figure 2.2: Level structure for ^{87}Rb relevant to the MOT operation

are reabsorption of the scattered radiation [89], and inelastic collisions between ground and excited state atoms [79], [90]. For shallow traps hyperfine-changing collisions between ground state atoms can also be important. These limitations can be mitigated to some extent with the so called dark SPOT [50] in which the central region of the MOT is shadowed from the repump light, keeping the atoms in a predominately dark state. Another way of implementing this idea is to apply a depump laser which drives the atoms to the lower hyperfine level or to simply reduce the repump intensity in the final stages of trapping [5], [87]. In any case densities beyond 10^{12}atoms/cm^3 have not yet been achieved in a MOT. However, as we shall see later, these ideas prove to be useful in achieving ultra-high densities in a dipole force trap.

2.1.2 Optical Dipole Traps

An atom in a light field is subjected to a mean force which can be written as a sum of a dissipative component and a reactive component [23]. The dissipative component is associated with spontaneous emission and is responsible for the cooling mechanisms to be

discussed in the next section. The reactive force, also known as the dipole force, can be thought of as a redistribution process involving absorption and stimulated emission. This redistribution process gives rise to a conservative force enabling the atom to be trapped by the light field. In [21], the authors use the dressed-atom picture to described the dipole force. This approach treats both the field and the atom quantum mechanically and uses a semiclassical approximation to treat the motion of the atom. For our purposes it suffices to treat the atom as a simple oscillator in a classical field and our treatment follows that in [37].

The dipole force arises from the interaction of the induced electric dipole moment $\mathbf{p}$ of an atom and the electric field $\mathbf{E}$ of the light field. In terms of the complex polarizability α the induced dipole moment may be expressed as $\mathbf{p} = \alpha\mathbf{E}$ so that the interaction potential can be written as

$$U = -\frac{1}{2}\langle \mathbf{p} \cdot \mathbf{E} \rangle = -\frac{1}{2\epsilon_0 c}\mathrm{Re}(\alpha)\mathrm{I}.$$

Here the angular brackets denote an averaging over optical time scales and we have introduced the intensity I of the field. The factor of one half is due to the fact that the dipole moment is induced and not permanent. The dipole force is given by the gradient of this potential and is thus a conservative force.

The imaginary part of the polarizability results in absorbtion of the power which can be expressed as

$$P_{abs} = \langle \dot{\mathbf{p}}\mathbf{E} \rangle = \frac{\omega}{\epsilon_0 c}\mathrm{Im}(\alpha)I$$

where ω is the angular frequency of the optical field. The absorbed power is re-emitted as dipole radiation and can be interpreted in terms of photon scattering. The associated scattering rate is then given by

$$\Gamma_{sc} = \frac{P_{abs}}{\hbar\omega} = \frac{1}{\hbar\epsilon_0 c}\mathrm{Im}(\alpha)I.$$

In order to completely determine the dipole force and associated scattering rate it remains to find an expression for the polarizability. To this end we consider the Lorentz model of a classical oscillator.

In the Lorentz model the equation of motion for the electron driven by an external

field is given by

$$\ddot{x} + \Gamma_\omega \dot{x} + \omega_0^2 = -eE(t)/m_e$$

where Γ_ω is the classical damping due to radiative energy loss and is given by the Larmor formula

$$\Gamma_\omega = \frac{e^2\omega^2}{6\pi\epsilon_0 m_e c^3}$$

Integration of the equation of motion gives the expression

$$\alpha = 6\pi\epsilon_0 c^3 \frac{\Gamma/\omega_0^2}{\omega_0^2 - \omega^2 - i(\omega^3/\omega_0^2)\Gamma}$$

for the polarizability where $\Gamma \equiv \Gamma_{\omega_0}$ When saturation effects can be neglected, as in the case of large detunings, this result agrees with a semiclassical treatment in which the atom is treated as a two level system in a classical field with one modification: The linewidth, Γ, is replaced by the expression

$$\Gamma = \frac{\omega_0^3}{3\pi\epsilon\hbar c^3} \left|\langle e|\mu|g\rangle\right|^2 .$$

The actual atoms used in experiments have a multilevel structure and some consideration should be given to the consequences of this fact. In general the structure of the atom gives rise to state dependent polarizabilities resulting in a trapping potential which depends on the polarization of the light field and the internal state of the atom. However for linear polarizations and large detunings, as considered in this thesis, these dependencies become negligible and the two level result still applies. For smaller detunings the reader is referred to [37] and [26] for further information.

The above expression for the polarizability can be substituted into the equations for the scattering rate and trapping potential with the result

$$U(\mathbf{r}) = -\frac{3\pi c^2}{2\omega_0^3}\left(\frac{\Gamma}{\omega_0 - \omega} + \frac{\Gamma}{\omega_0 - \omega}\right) \mathrm{I}(\mathbf{r}) \tag{2.3}$$

$$\Gamma_{sc} = \frac{3\pi c^2}{2\hbar\omega_0^3}\left(\frac{\omega}{\omega_0}\right)^3 \left(\frac{\Gamma}{\omega_0 - \omega} + \frac{\Gamma}{\omega_0 - \omega}\right)^2 \mathrm{I}(\mathbf{r}) \tag{2.4}$$

where we have assumed that the detuning, $\Delta \equiv \omega_0 - \omega$, is much greater than the linewidth, Γ. Typically the additional assumption that $\Delta \ll \omega_0$ is made and one obtains the expressions

$$U(\mathbf{r}) = -\frac{3\pi c^2}{2\omega_0^3}\frac{\Gamma}{\Delta}\mathrm{I}(\mathbf{r}), \tag{2.5}$$

$$\Gamma_{sc} = \frac{3\pi c^2}{2\hbar\omega_0^3}\left(\frac{\Gamma}{\Delta}\right)^2 \mathrm{I}(\mathbf{r}) = \frac{\Gamma}{\hbar\Delta}U \tag{2.6}$$

which are relevant to the so called far off resonant trap or FORT. These expressions illustrate the fact that by increasing both the intensity of the trapping beam and the detuning one can maintain the trap depth and decrease the scattering rate.

In the case of a CO_2 laser, the detuning is no longer small relative to the atomic resonance and the approximations leading to equations (2.5) and (2.6) are no longer valid. In this case the driving frequency, ω, is negligible relative to ω_0 so that the potential takes the simple form

$$U = -\frac{\alpha_s}{2\epsilon_0 c}\mathrm{I} \tag{2.7}$$

where α_s is the static polarizability. In this quasi-electrostatic limit the scattering rate can be written as

$$\Gamma_{sc} = \frac{2\Gamma}{\hbar\omega_0}\left(\frac{\omega}{\omega_0}\right)^3 U. \tag{2.8}$$

which is a factor $2(\omega/\omega_0)^3$ beyond that for a FORT. For a well depth of 300μK the scattering rate is approximately $5 \times 10^{-4}\mathrm{s}^{-1}$ justifying the statement that the quasi-electrostatic trap (QUEST) is, for all practical purposes, a conservative trap.

2.2 Laser Cooling

Since the CO_2 trap is a practically conservative trap it is necessary to either cool the atoms into the trap or to snap the potential on suddenly after the MOT has been extinguished, thus capturing those atoms spatially overlapped with the trapping beam. As noted in the first demonstration [86], best results are obtained by cooling into the trap as one could well expect. Due to the difference in light shifts of the excited and ground state the resonance frequency of an atom located within the trap is red-shifted. For this reason the detuning of the MOT beams is typically shifted further into the red [86], [32],[33]. However, we find, as in [32],[33] that the best results are obtained when the detuning is far greater than the Stark shift induced by the trapping beam. Furthermore, in our experiments the MOT is loaded with the MOT beams typically detuned $\sim 5\Gamma/2$ from resonance and the expected Stark shift from the single focus trap would be at most $\sim \Gamma$. Loading with these detunings gives inferior results than those obtained with larger detunings indicating that the Stark shift induced by the trap plays a secondary role in the loading dynamics. With the detunings

being as large as they are under optimum loading it would seem that sub-Doppler cooling mechanisms indeed play a role. In this section we review some of the basic principles of laser cooling. The field of laser cooling has a very broad scope and we limit our discussion to the Doppler and sub-Doppler cooling mechanisms most relevant to this work.

2.2.1 Doppler Cooling

The scattering force

The easiest force to understand is that of the scattering force. When an atom absorbs or emits a photon it recoils so that momentum is conserved. In a laser beam the recoil from absorption is always in the same direction whereas the recoil from spontaneous emission is random. Thus, if the atom scatters many photons the momentum transfer from emission averages to zero leaving only the contribution from absorption. This momentum transfer can be expressed as a force which may be written as

$$F_{sp} = \frac{\hbar k \Gamma}{2} \frac{I/I_s}{1 + I/I_s + (2\Delta/\Gamma)^2} \tag{2.9}$$

where Γ is the line-width of the transition, Δ the laser detuning, I the intensity, and $I_s = 1.6\text{mW/cm}^2$ the saturation intensity. The equation simply states that the force is given by the momentum kick of a single photon multiplied by the rate at which photons are scattered and so is referred to as the scattering force. Note that the force saturates at large intensity. While increasing the intensity increases the absorption rate it also increases the rate of stimulated emission. Since the momentum kick from stimulated emission exactly cancels that due to absorption, the forces saturates with the spontaneous emission rate.

Cooling of a moving atom

To understand the cooling nature of the scattering force consider an atom subjected to two counter-propagating beams detuned from resonance. If the atom is stationary it scatters equally from both beams resulting in a average force of zero. However if the atom moves it experiences a Doppler shift moving it closer to resonance with one beam and further from the other. This results in a net force associated with the imbalance of the scattering force from each beam. When the beam is red-detuned, i.e. is detuned below the atomic

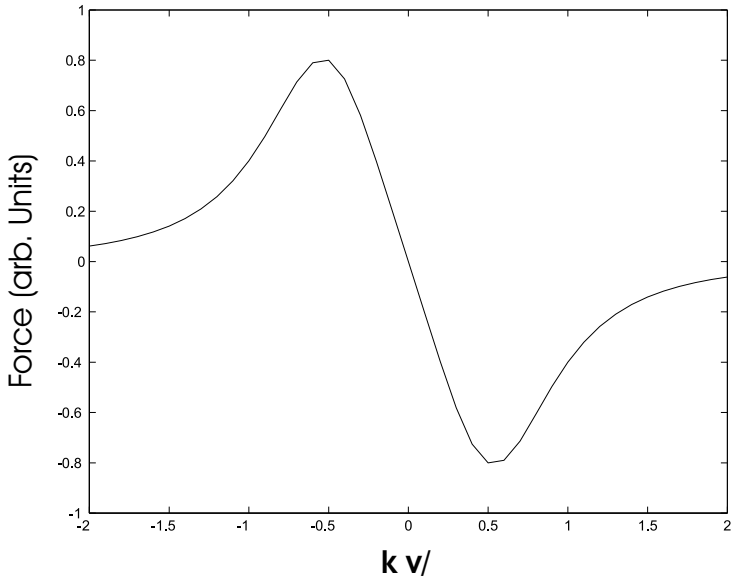

Figure 2.3: Scattering force for two counter-propagating beams as a function velocity

frequency, the force acts to oppose the motion of the atom and is thus a cooling force. This is precisely the mechanism providing cooling in the MOT and in Fig 2.3 we show its dependence on velocity. Cooling in 3 dimensions, as in the MOT, can be achieved by providing cooling beams in all three directions. It should be noted that the cooling power is limited. Since the force derives from discrete momentum kicks, there is an inherent diffusion in momentum space. This diffusion results in a limiting temperature given by $k_b T \sim \hbar\Gamma/2$ (see, for example, [36], [93], [83]). For ^{87}Rb this limit is about 140μK. Experimentally, it was soon realized that temperatures well below this limit could be achieved [59]. To explain this fact a more sophisticated description involving the multilevel structure of the atom was needed, which we now discuss.

2.2.2 Sub-Doppler Cooling

In the previous section on dipole traps we briefly alluded to the fact that the trapping potentials induced by a light field depended on the internal state of the atom. When polarization gradients are present optical pumping between the different potentials can give rise to new cooling mechanisms, which turn out to be much more efficient than the Doppler

cooling just discussed. Here we consider two possibilities which differ only in the choice of polarization for the two counter-propagating beams. The first uses linear polarizations that are orthogonal to each other, and is referred to as lin $\perp$ lin cooling. The second also involves orthogonal polarizations. However they are circularly polarized and is referred to as $\sigma^+ - \sigma^-$ cooling. In what follows we do not attempt to give an in-depth treatment of the cooling mechanisms as such a treatment can be found in [22] or [23, Course1]. We simply give the physical picture to illustrate the mechanisms of interest.

lin $\perp$ lin configuration

When the polarizations of the counter-propagating beams are orthogonal and linear the resulting field can be expressed as

$$\begin{aligned} E &= E_0 \left(\cos(kz - \omega t)\hat{x} + \cos(kz + \omega t)\hat{y}\right) \\ &= \frac{E_0}{\sqrt{2}} e^{-i\omega t} \left(\cos(kz)\frac{\hat{x} + \hat{y}}{\sqrt{2}} + i\sin(kz)\frac{\hat{x} - \hat{y}}{\sqrt{2}}\right) + c.c. \end{aligned} \tag{2.10}$$

Thus the field describes one in which the polarization spatially varies over the length scale of the wavelength as illustrated in fig 2.4. To illustrate the cooling nature of this configuration we consider a $J_g \rightarrow J_g + 1$ transition and take the simplest example with a degenerate ground state namely $J_g = 1/2$. The light shifts for the ground states can be written as

$$\Delta E_g = \frac{\hbar\delta I / I_s C_{ge}^2}{1 + (2\delta/\Gamma)^2}, \tag{2.11}$$

where C_{ge} is the Clebsch-Gordon coefficient describing the coupling of the atom to the light field. This coefficient depends on the magnetic state of the atom and on the polarization of the light field so the light shift is spatially varying due to the polarization gradient of the field. In fig 2.4 we show schematically the light shift for the two magnetic sub-states. To discuss the origin of the cooling consider an atom in the $M = +1/2$ state starting at the origin where the light shift is maximum with the light field being σ^+. As the atom moves along the z axis its potential energy increases and its kinetic energy decreases so as to conserve energy. When the atom has moved a distance $\lambda/4$ the light shift is a minimum and the field is σ^-. Thus the atom is optically pumped to the $M = -1/2$ state where it finds itself back at the bottom of the hill. Thus cooling arises from the kinetic energy

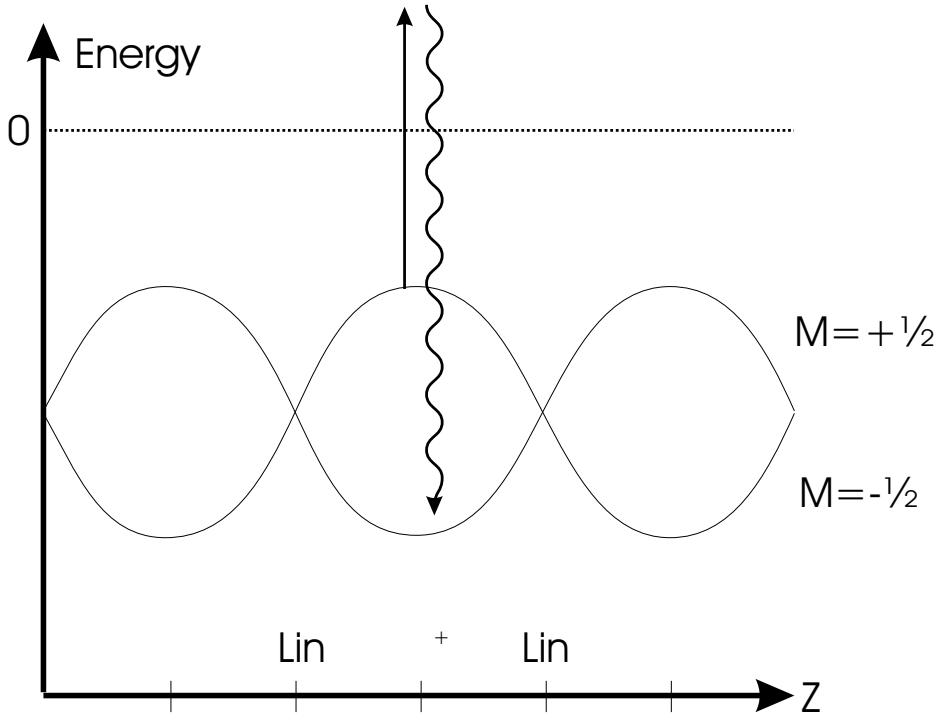

Figure 2.4: Schematic of the light-shift potentials involved in sub-doppler cooling

being converted to potential energy which is subsequently carried away by the field. As this process brings to mind the Greek myth in which Sisyphus was condemned for eternity to push a stone up a mountain, this process is often referred to as Sisyphus cooling. It was shown in [22] that the temperature decreases with increased detuning and decreased intensity but, being dependent on photon scattering, the temperature is limited to $\sim 10T_r$ where T_r is the recoil temperature which, for ^{87}Rb is 360nK. Thus one can expect the minimum temperatures obtained to be a few μK which is far below the doppler limit.

$\sigma^+ - \sigma-$ configuration

In this case the field can be written as

$$E = -i\sqrt{2}E_0 Exp{-i\omega t}(\cos(kz)\hat{x} - \sin(kz)\hat{y}) + c.c. \tag{2.12}$$

which is everywhere linearly polarized but the direction of polarization rotates about the z axis over the length scale of the wavelength. Since there are no spatially varying light shifts associated with this field the cooling mechanism in this configuration cannot rely on a Sisyphus type effect. Instead the force derives from a ground state orientation and so requires at least $J_g = 1$. In general it works for any $J_g \rightarrow J_e = J_g, J_g \pm 1$, and here we specifically consider a $J_e = 2$.

Let us now consider a stationary atom. Since the field is linear the population is shifted with the $M = 0$ state more heavily populated that the $M = \pm 1$ states. In contrast when the atom moves it experiences or 'sees' a rotation of the quantization axis and, as a result and the population distribution shifts. As shown in [22], when the atom moves towards the σ^+ beam the population shifts to the $M = +1$ state. Since this state couples most strongly to the σ_+ the resulting scattering force tends to oppose the motion. Moving in the other direction results in a similar effect. Well the force here derives from differential scattering from the laser beams it should not be confused with the Doppler mechanism described earlier. Here the difference arises from an imbalance in the population. As shown in [22] similar final temperatures to the previous case of lin $\perp$ lin are expected.

It is worth noting the specific case of $J_g = 1 \rightarrow J_e = 1$ as discussed in [6]. In this case a zero velocity dark state exists such that for atoms rest there is a superposition state

not coupled to the light. Thus if an atom, through spontaneous emission, finds itself at rest in this state it no longer interacts with the light so that there will be an accumulation of atoms in this zero velocity dark state. This is a powerful technique by which to cool atoms below the photon recoil limit, however it is limited to low density samples. At high densities reabsorption of scattered light becomes important and the scattered light can couple to the dark state.

2.3 Evaporative Cooling

Evaporation is a naturally occurring process in which atoms with the highest energy leave the trap. Since these atoms have a larger than average share of the energy, this process lowers the average energy, and thus the temperature, of the remaining atoms. Intra-trap collisions invoke a continuous thermalization process so that the high energy tail of the Boltzmann distribution is replenished. However, as one might expect, the probability that an atom is ejected from the trap decreases as η, the ratio of trap depth to temperature, increases so that the evaporation process eventually stagnates. Thus, for efficient cooling, the effective depth of the potential needs to be lowered so as to maintain efficient removal of the highest energy atoms.

In magnetic traps removal of high energy atoms is accomplished with a radio frequency magnetic field. Because the higher energy atoms sample the trap regions with higher magnetic field, their spin-flip transition frequencies are shifted due to the Zeeman effect. Thus the RF field can be set to selectively drive these higher energy atoms to an untrapped spin state. Cooling continues by ramping down the RF frequency and thus lowering the effective trap depth. In this way the temperature decreases while simultaneously increasing both the density and collision rate. This is the standard technique used to create BEC today and for a detailed review of evaporative cooling of trapped atoms see [52].

In optical dipole traps the situation is somewhat simpler. Since the trapping potential is state independent there is no obvious analog to the RF knife used in magnetic traps. The simplest alternative is to ramped down the power in the beam so as to lower the trap depth. In this way we have been able to produce, for the first time, a Bose-condensate in a

purely optical system. In this section we review the techniques used to model this process. We begin with the simple scaling laws developed in [71] to illustrate the limitations of our technique and, more importantly, obtain an estimate for the initial conditions needed to obtain condensation via our approach. We then discuss a more sophisticated approach as described in [64] and generalized in [11]. In this approach we approximate the trapping potentials by truncated harmonic oscillators. While this approximation is somewhat crude the model can incorporate non-evaporative losses so as to gain insight as to the role these play in the evaporation process.

2.3.1 Scaling Laws

While the evaporation process is most accurately modelled using the Boltzmann equation, this description does not easily answer the two most pressing questions asked by the experimentalist: Can it be done? and, if so, what needs to be done to make it possible? The answer to these questions is provided by a simple "back of the envelope" type calculation, given in [71], which we outline here.

We begin by noting that the evaporation process stagnates when η becomes large and in this regime the trapped gas is confined to a region in which the potential is well approximated by a harmonic oscillator. Thus the energy is given by $E = 3Nk_bT$ from which we can obtain the rate equation

$$\begin{aligned} \dot{E} &= \frac{\partial E}{\partial T}\dot{T} + \frac{\partial E}{\partial N}\dot{N} \\ &= 3Nk_b\dot{T} + 3k_bT\dot{N}. \end{aligned} \tag{2.13}$$

This change in energy comes from two contributions: energy is carried away by evaporated atoms and the energy decreases due to the adiabatic lowering of the potential. The average energy carried away by the evaporated atoms is given by $(\eta + \kappa)k_bT$, where κ is a small number usually between 0 and 1 and depends on η and the details of the trapping potential [52, pg 185]. As we are principally concerned with large η we can ignore it and we find that the rate of change of the internal energy due to evaporation is then given by $\dot{E_{ev}} = \dot{N}(\eta k_bT)$. To find the rate due to the changing potential we note that the action is an adiabatic invariant so that E/ν is a constant where ν is the (geometrically averaged) trap frequency.

Since $\nu \propto \sqrt{U_0}$ we find that change in energy associated with the decreasing potential is thus $(3Nk_bT/2)\dot{U}_0/U_0$. Therefore, we have

$$\eta k_b T\dot{N} + \frac{3}{2}\frac{\dot{U}_0}{U_0} = 3Nk_b\dot{T} + 3k_bT\dot{N}. \tag{2.14}$$

By definition we have $U_0 = \eta k_b T$ so that, if we assume η remains constant, we may write $\dot{U}_0 = \eta k_b \dot{T}$. This expression can then be used to eliminate $\dot{T}$ from equation (2.14) and we obtain the result

$$\frac{\dot{N}}{N} = \frac{1}{2}\frac{3}{\eta - 3}\frac{\dot{U}_0}{U_0}. \tag{2.15}$$

This expression can be trivially integrated to obtain the scaling law

$$\frac{N_i}{N_f} = \left(\frac{U_i}{U_f}\right)^{\frac{1}{2}\frac{3}{\eta-3}}. \tag{2.16}$$

We are, of course, principally concerned with the increase in phase space density. For the harmonic oscillator approximation used here the phase space density is given by[2]

$$\rho = N\left(\frac{h\nu}{k_bT}\right)^3 \tag{2.17}$$

Since $\nu \propto \sqrt{U_0}$ and $U_0 = \eta k_b T$ we can then write

$$\frac{\rho_f}{\rho_i} = \left(\frac{U_i}{U_f}\right)^{\frac{1}{2}\frac{\eta-4}{\eta-3}} \tag{2.18}$$

This equation gives us a rough estimate for the initial phase space density we need to achieve in order to cross the BEC transition. Typically we have $\eta \sim 10$ and its reasonably straightforward to change the trap depth by a factor of 100. Thus in order to achieve a unity phase space density we require $\rho_i \sim 0.001$.

As yet we have not considered the speed of the evaporation process. In assuming constant η we have implicitly assumed that the relaxation time of the trapped gas is much faster than the timescale over which the potential changes. This relaxation time is determined by the elastic collision rate so one needs to consider how this quantity evolves during the process. This rate is given by $\gamma = 4n_0\sigma\bar{v}/\sqrt{3\pi}$ [67, pg 173] where $\bar{v} = \sqrt{3k_bT/M}$ is the

[2]The expression given is not strictly the phase space density but is valid provided it is much less than one. Nevertheless it is a useful parameter approaching the value of 1.202 as one approaches criticality.

average velocity of the trapped atoms, n_0 is the peak density, and σ is the cross-section for elastic collisions. Thus $\gamma \propto N\nu^3/T$ so we may write

$$\frac{\gamma_f}{\gamma_i} = \left(\frac{U_f}{U_i}\right)^{\frac{1}{2}\frac{\eta}{\eta-3}} \tag{2.19}$$

Using the numbers above we expect the collision rate to change by a factor of about 25.

2.3.2 Modelling Evaporation

The scaling laws given in the previous section provide very simple estimates for the conditions one needs to create in order to achieve quantum degeneracy. However they fail to provide any insight as to the effects of background losses or inelastic collisions on the evaporation process. For these purposes a more sophisticated approach is called for. It is not our intention to provide a model which accurately depicts our experimental system. Rather we seek a simple model that can account for the qualitative features we see, provide some insight as to the effectiveness of a non-ideal system, and can run on a home computer with a similar run time as the actual experiment. The approach we take follows that found in [64] and an in-depth discussion can be found in [71]. Here we merely summarize the main features and discuss the assumptions made.

Basic Assumptions

The model we describe here assumes that the thermodynamics of the evaporating gas is well described by a truncated Boltzmann distribution and that the atomic motion is sufficiently ergodic so that this distribution depends solely on their energy. Furthermore the model assumes that every atom with energy ϵ greater than the trap depth ϵ_t is removed before colliding with another atom so that the evaporation is considered to be complete and fully 3D. The use of a truncated Boltzmann distribution was validated by comparison with a numerical solution to the Boltzmann equation [64] and by a Monte Carlo technique given in [3]. However the assumption of 3D evaporation is deserving of some discussion.

In [30] the authors noted that, due to gravity, evaporation predominately occurs in only one spatial dimension, which slows down the cooling process citing the work done in [74]. However this work illustrated the difference between 1D and 3D evaporation. Evapo-

ration is considered one dimensional if the energy of motion in only one direction determines the escape criteria and evaporation under these conditions was shown to be significantly reduced. This is easy to understand: The phase space volume associated with loss is obviously smaller. While gravity causes atom loss predominately along one direction, the condition for escape is not necessarily based on the energy associated with this direction. If the energy of the atom is large enough it will leave independent of the direction its heading. In the absence of gravity the escape energy is independent of direction so the evaporation is 3D. Gravity changes the directional dependence of the escape energy but no so much so as to effect a dimensional change in the evaporation. If, for example, no integral of the motion exists, an atom with a given energy will ergodically explore the entire energy surface it's on. If part of this surface leads to escape then the entire surface does. Of course it may take some atoms longer than others and this can lead to reduced evaporative power. To illustrate this we take a closer look at the single focus trap.

In magnetic traps the trap depth is controlled using an RF knife which cuts away the atoms from the outermost regions of the cloud. In our system the trap depth is determined by gravity and in Fig 2.5 we show two equipotential surfaces for the single beam trap. We have chosen a beam waist of 75μm and a depth of 100μK although the exact values are inconsequential to this discussion. The first surface has an energy slightly above the trap depth (by a fraction of a percent). Since atoms with this energy cannot cross this potential surface their only avenue of escape is through the small regions at either ends of the trap. We thus expect there to be a low probability of escape. The second surface shown has a potential energy a mere 5% above the trap depth. Integration of 5000 randomly chosen initial conditions consistent with this energy reveals that $\sim 60\%$ of the atoms with this energy escape within 3 longitudinal oscillations [3]. Increasing the energy to 10% above the trap depth increases the escape rate to $\sim 80\%$. Thus it would seem that the effect of gravity is better described as an increase in the effective trap depth, not to alter the dimensionality of the evaporation. Well this increase in effective trap depth would serve to decrease the evaporation rate it would not be to the extent expected by a reduction in dimensionality.

Finally, we would like to remark on the assumption that the evaporation is complete

[3]For the typical conditions we create in this particular trap this time scale is on the order of one collision time

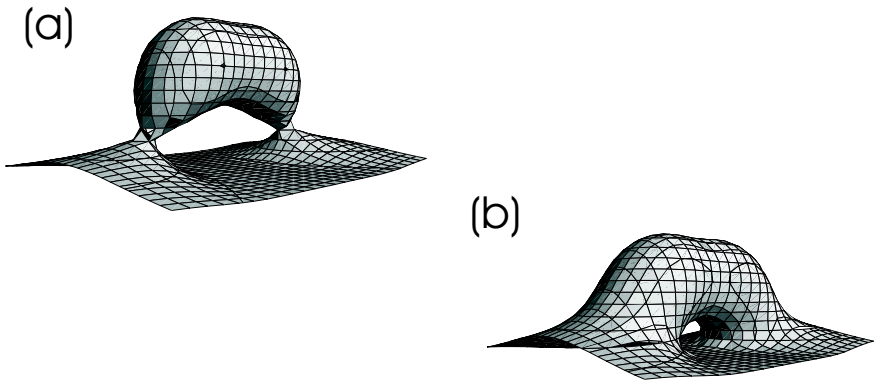

Figure 2.5: Equipotential surfaces of the single focus trap relevant for escape energies - see text

in the sense that atoms with sufficient energy escape without any further collisions taking place. This assumption requires that the trapped gas be well within the Knudson regime, that is, the mean free path of the atoms should be much larger than the dimensions of the trapped gas. Equivalently, the trap frequencies should be much larger than the collision rate. This is a standard assumption which is well satisfied by most experiments. However, in the case of the single focus trap this criteria is just barely satisfied, in the 1D lattice trap the collision rate is on the order of the transverse frequencies and in the cross beam configuration the collision rate actually exceeds the trap frequencies. Intuitively one would expect that this wouldn't stop the evaporation process but rather slow it down. Atoms with sufficient energy in this direction would most likely undergo a collision preventing the escape. Presumably the effect is to increase the effective trap depth since the collisions themselves would provide the mixing required to assume 3D evaporation. We do not attempt to justify this statement. We leave this as an open problem noting that our work clearly establishes conditions which warrants a more detailed consideration of evaporation in this regime.

ODE's for the evolution of the gas

Under the assumption of sufficient ergodicity all relevant information about the trapping potential is given by the density of states which can be written

$$\begin{aligned}\rho(\epsilon) &\equiv (2\pi\hbar)^{-3}\int \delta(\epsilon - U(\mathbf{r}) - p^2/2m)\, d^3r\, d^3p \\ &= \frac{2\pi(2m)^{3/2}}{(2\pi\hbar)^3}\int \sqrt{\epsilon - U(\mathbf{r})}\, d^3r.\end{aligned} \tag{2.20}$$

With the assumption of a truncated Boltzmann form the distribution over these states is given by

$$f(\epsilon) = n_0\Lambda^3 e^{-\epsilon/k_bT}\Theta(\epsilon_t - \epsilon), \tag{2.21}$$

where Θ is the Heaviside step function, n_0 is a reference density, and $\Lambda = (2\pi\hbar^2/mk_bT)^1/2$ is the thermal de Broglie wavelength. With these simplifications the time evolution of the trapped gas can be described by two differential equations [64], [11], [74],

$$\dot{N} = \dot{N_{ev}} + \dot{N_\theta} + \dot{N_{3B}} \tag{2.22}$$

$$C\dot{T} = \dot{E_{ev}} + \dot{E_\theta} + \dot{E_{3B}} - \left(\frac{3}{2} + \gamma\right) k_bT\dot{N} - \left(\frac{\partial\gamma}{\partial\theta}\right)_T Nk_bT\dot{\theta}. \tag{2.23}$$

These equations simply reflect the fact that the rate of change of number and energy is just the sum of the independent contributions due to evaporation, trap changes, and three body recombination. Since we trap only the $F = 1$ ground state, no two body inelastic losses are present [52] and we have neglected any possible heating due to trap instabilities as we have not seen any evidence of such heating in our experiments. At this point we have not included losses due to background collisions. This simply adds an additional term $-\Gamma_bN$ to the number equation with no change to the temperature equation if heating effects of such losses are neglected. In the above expressions θ represents the set of parameters which controls the potential. In our system this is just the power in the trapping beams. We now summarize the forms for each of the contributions mentioned. For now we retain generality by keeping the density of states unspecified.

Evaporation terms

As derived in [64] the contributions due to evaporation can be written as

$$\dot{N_{ev}} = -n_0^2 \sigma \bar{v} e^{-\eta} V_{ev} \tag{2.24}$$

$$\dot{E_{ev}} = \dot{N_{ev}} \left(\eta + 1 - \frac{X_{ev}}{V_{ev}} \right) k_b T. \tag{2.25}$$

In these expressions σ is the elastic cross-section, $\bar{v} \equiv (8k_bT/\pi m)^{1/2}$ is the average velocity of the trapped atoms, $\eta = \epsilon_t/k_bT$ and n_0 is the reference density which is related to the number of trapped atoms via $n_0 = N/V_e$ where V_e is given by

$$V_e = \Lambda^3 \int_0^{\epsilon_t} \rho(\epsilon) \exp(-\epsilon/k_bT)\, d\epsilon \tag{2.26}$$

The volumes V_{ev} and X_{ev} can be similarly expressed in terms of the density of states. Specifically

$$V_{ev} = \frac{\Lambda^3}{k_bT} \int_0^{\epsilon_t} \rho(\epsilon) \left[(\epsilon_t - \epsilon - k_bT) e^{-\epsilon/k_bT} + k_bT e^{-\eta} \right] d\epsilon \tag{2.27}$$

$$X_{ev} = \frac{\Lambda^3}{k_bT} \int_0^{\epsilon_t} \rho(\epsilon) \left[k_bT e^{-\epsilon/k_bT} - (\epsilon_t - \epsilon + k_bT) e^{-\eta} \right] d\epsilon \tag{2.28}$$

Terms involving trap changes

Changes in the trapping potential results in a loss of atoms and a change in the energy of the remaining atoms. These changes are independent of evaporation as they occur even in the absence of collisions. Using the total number of states $\mathcal{N} = \int_0^{\epsilon_t} \rho(\epsilon)\, d\epsilon$ it was shown in [74] that the terms due to changes in the trapping potential are, for 3D evaporation, given by

$$\dot{N_\theta} = n_0 \Lambda^3 e^{-\eta} \dot{\mathcal{N}} \tag{2.29}$$

$$\dot{E_\theta} = (1+\eta) k_bT \dot{N_\theta} - \frac{N k_bT}{V_e} \left(\frac{\partial V_e}{\partial \theta} \right)_T \dot{\theta}. \tag{2.30}$$

Three body recombination

In the case of the cross beam geometry we are able to achieve densities of 10^{14}atoms/cm^3. At these densities losses due to three body recombination are expected to play a role. Furthermore, since such losses predominately occur at the core of the distribution atoms

lost by this mechanism give rise to an effective heating. To include these effects we follow the approach used in [74] to include dipolar relaxation. We thus have

$$\dot{N_{3B}} = -n_0^3 L V_{3e} \tag{2.31}$$

$$\dot{E_{3B}} = \left(\frac{3}{2} + \frac{T}{3V_{3e}}\frac{\partial V_{3e}}{\partial T}\right) k_b T \dot{N_{3B}} \tag{2.32}$$

where L is the three body recombination rate coefficient and $V_{3e} = \int (n(\mathbf{r})/n_0)^3 \, d^3r$ is the effective volume for trinary collisions.

Density of states

As yet we have not specified the density of states $\rho(\epsilon)$ which is determined by the geometry of the trap. Using the true potential can give rise to problems as in the case of a single focus trap. For a focussed gaussian beam, the density of states exhibits a simple pole at an energy given by the trap depth and since many of the expressions above involve an integral over ρ the results are meaningless. In [30] the authors replace the potential with a three dimensional gaussian for which the density of states remains integrable. Another approach would be to include gravity which serves to truncate the potential below the energy at which the divergence occurs. In either case simple expressions for ρ cannot be obtained and one has to resort to numerical techniques. For the three geometries we are interested in this can become quite tedious, and we adopt a somewhat more simplistic approach by approximating the potential by a harmonic oscillator truncated at the trap depth. This is a very crude approximation but it has the advantage that analytic expressions for all the above expressions can be obtained. With this approximation the density of states can be trivially calculated with the result

$$\rho(\epsilon) = \frac{1}{2(\hbar\bar{\omega})^3}\epsilon^2 \tag{2.33}$$

where $\bar{\omega}$ is the geometrically averaged frequency of the system. With this expression all of the above terms can be evaluated in terms of generalized gamma functions most of which are given in [64]. For completeness these expressions can be found in appendix A.

The parameters that appear in the model above can either be measured directly or obtained from published data with the exception of the trap depth. This can of course be

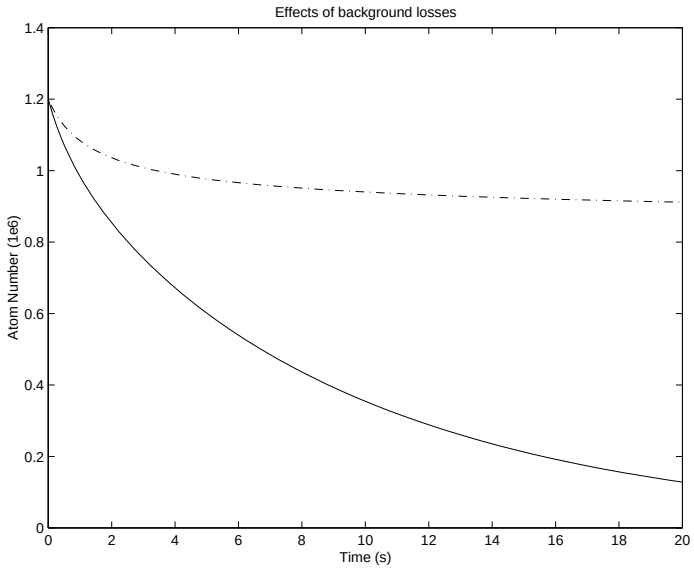

Figure 2.6: Evolution of number of trapped atoms in a single focus trap illustrating the effect of background losses. Solid curve includes background losses whereas the dashed curve does not.

estimated from the measured frequencies but in view of the earlier discussions regarding the roll of gravity and high collision rates in the evaporation process, we leave this as an adjustable parameter to obtain the best fit to the data. We defer the comparison to the data to later chapters where we discuss the actual experiments. For now we illustrate features of the model by illustrating the effects of the various terms.

Features of the model

We begin with the single focus trap. In Fig 2.6 and 2.7 we show the number and phase space density as a function of time. The parameters chosen are appropriate to the single focus trap. Specifically we have $\bar{\omega} = 750\text{rad/s}$ and $U_0 = 100\mu\text{K}$. The plots show results with and without background losses with the background loss rate chosen to be 0.1s^{-1}. Clearly the loss causes an eventual decay of the phase space density but note that the effect sets in after only a few seconds. In the cross beam configuration the densities are typically above $10^{14}\text{atoms/cm}^{-3}$ where three body losses become significant. Since these losses occur at the densest part of the cloud it very much opposes evaporation since it is the coldest

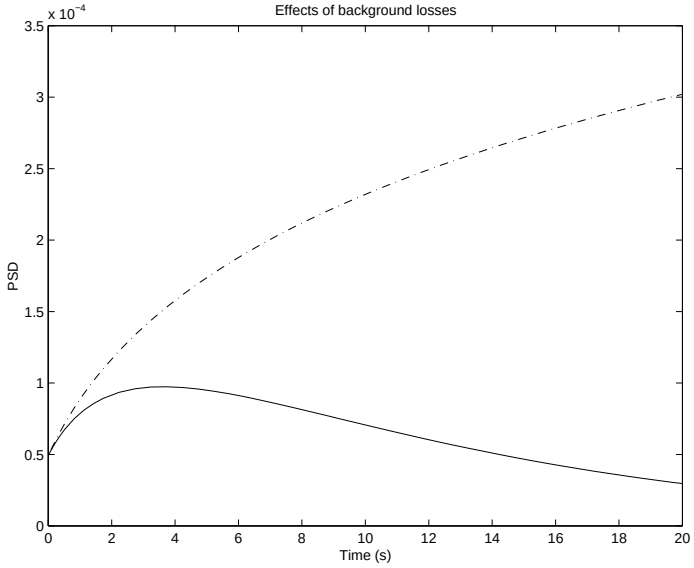

Figure 2.7: Evolution of phase space density in the single focus trap. Solid curve includes background losses whereas the dashed curve does not

atoms that are lost. The effect is illustrated in Fig 2.8 and Fig 2.9. Here we have chosen $\bar{\omega} = 9100$, $U_0 = 650\mu$K and a three body loss coefficient given by the theoretical value [31], $L = 1.15 \times 10^{-28}\text{cm}^6\text{s}^{-1}$. The background loss is as for the previous example. The initial conditions are consistent with an initial density of $1.5 \times 10^{14}\text{atoms/cm}^{-3}$ which gives an initial loss rate of 4.7s^{-1}. In order to better illustrate the effects of each term we have given four plots, which from top to bottom, correspond to no losses, background losses only, three-body losses only, and finally both losses together. Clearly three-body recombination dominates the lifetime curve.

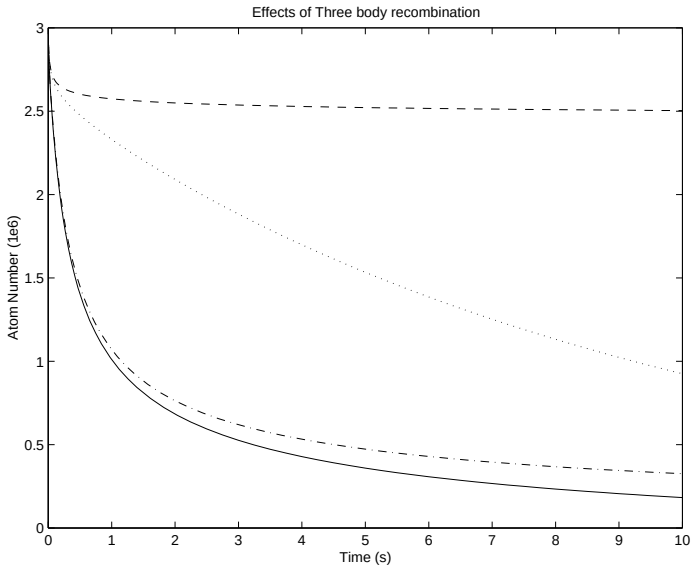

Figure 2.8: Evolution of number of trapped atoms in the cross beam trap. The different curves illustrate the effects of background and three body losses - see text for detail.

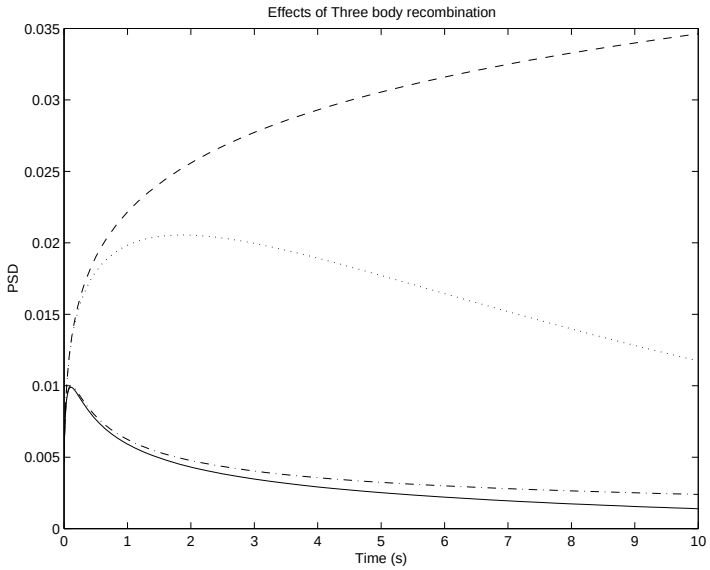

Figure 2.9: Evolution of phase space density in the cross beam trap. The different curves illustrate the effects of background and three body losses - see text for detail.

Chapter 3

Experimental Setup

We now turn our attention to the technical details of the experimental setup. We begin with a discussion of the diode lasers and their setup which is followed by a brief description of a typical setup for a dipole force trap. In section three we discuss the alignment of the system and the loading procedure for the dipole force traps. The final section deals with diagnostic techniques used to characterize the traps and the atomic sample.

3.1 The Diode Lasers

Trapping and cooling rubidium atoms is greatly simplified by the availability of the inexpensive diode laser producing up to 100mW of 780nm light. With a little work on the electronics, housing, and external optics these lasers can be made to lase with the frequencies and sub-MHz line-widths required for most atom trapping and cooling experiments. Reference [92] gives a practical guide to using these lasers and outlines the various methods that can be used to tune and narrow their output spectra. Our setup is similar to the setups described in [65], [61], and we briefly outline the main features.

3.1.1 Frequency Stabilization

Since the diode laser output spectra is sensitive to both temperature and injection current, precise regulation of these quantities is required for long term stable operation. To this end the laser is housed inside an aluminium block which is temperature stabilized to ~ 1 mK and the diode current is provided by the controller described in [62]. As in [65] the output frequency is controlled using optical feedback from a diffraction grating. The position of the grating, and thus the frequency of the laser, can be finely controlled using a piezo-electric

transducer (PZT).

For long term frequency stability the laser needs to be actively stabilized. This is done by locking the laser to a saturated absorption spectra [2],[43] using a lock-in technique [42, pg 1032-1034]. A schematic of the setup is shown in Fig 3.1. The injection current to the laser, and thus the laser frequency, is modulated by a small amplitude high frequency ($\sim$ 6 MHz) signal and the saturated absorption signal is then phase-detected relative to the modulating signal. The result is an error signal proportional to the slope of the saturated absorption signal allowing one to lock the laser to a resonance peak. This is accomplished by feeding the error signal through a PI controller [29] with the output of the integrator controlling the grating position and the proportional output controlling the injection current to the laser. If both signals controlled the grating position the bandwidth of the lock would be limited by the ability to drive the PZT ($\sim$ 1 kHz). If both were used to control the injection current the DC component needed to compensate drift of the laser frequency would cause the laser to mode hop and lose lock due to the limited range over which the current can be changed. Splitting the signal in this fashion allows us to lock the laser for many hours or even days with a bandwidth up to 10 kHz.

3.1.2 Frequency Control

For our experiments it is imperative that we have online control of the laser frequency. The frequency of the light can be controlled externally with an acousto-optic modulator (AOM) however the beam is deflected at an angle proportional to the frequency shift. Such beam steering is highly undesirable particularly if the light is fibre coupled as in our case. In order to overcome this problem the AOM can be set up in a double pass configuration as shown in Fig 3.2. Here the modulator is placed at the center of a one to one telescope and is thus at the focal plane of each lens. In this configuration the deflected beam is perpendicular to the retro mirror independent of the angle of deflection and thus independent of the frequency shift. This set up has the advantage of doubling the range over which the frequency can be swept although this comes at the cost of reduced power output due to the efficiency of the AOM. Even if this reduced power is tolerable the efficiency of the AOM depends on the frequency shift so that the power in the beam becomes frequency dependent. To avoid this,

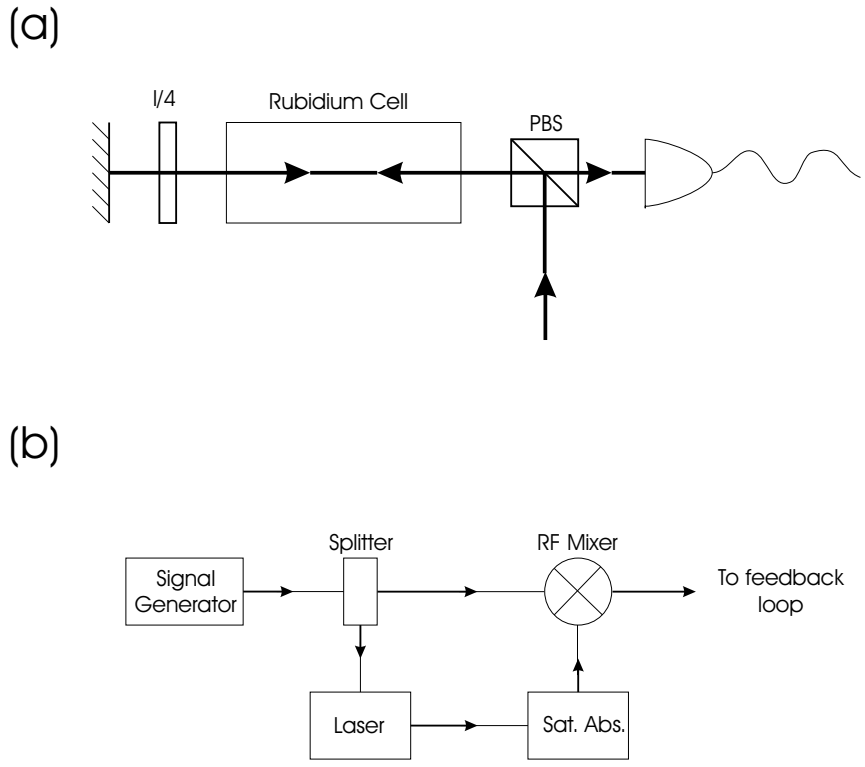

Figure 3.1: (a) Saturated absorption set up. (b) Schematic of the lock in technique

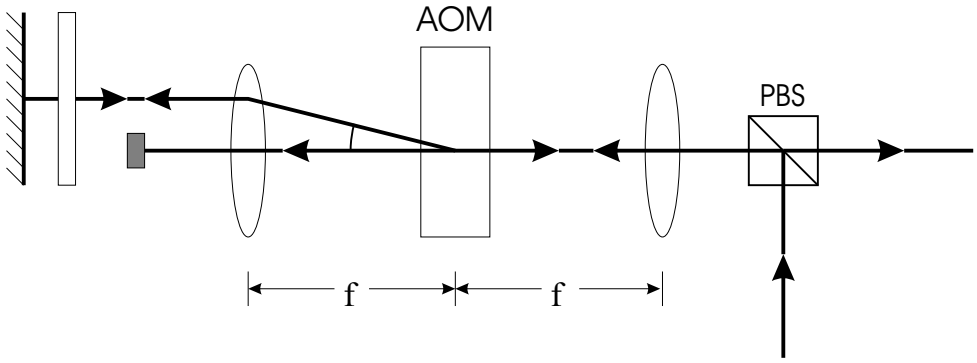

Figure 3.2: Double pass configuration used in experiment - see text

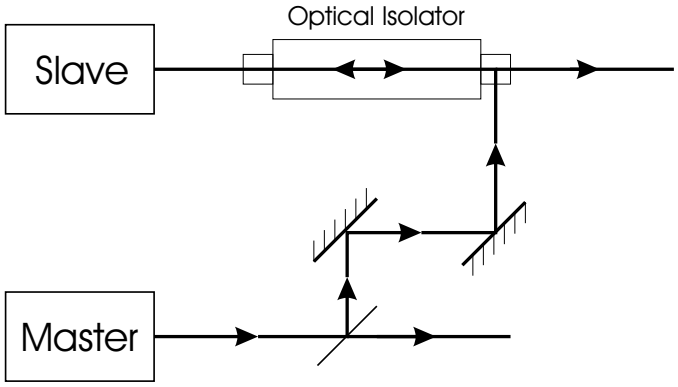

Figure 3.3: Basic master-slave configuration. Not shown is the frequency shift of the injection signal

we use the double passed beam to injection lock three slave lasers.

A detailed discussion on injection locking can be found in [80, Ch. 29]. The basic idea is that an un-stabilized laser can be locked to a stabilized master laser by coupling a small amount of power from the master into the slave. The basic setup is shown in Fig 3.3. The light from the master is coupled to the slave through an optical isolator so that the master laser is isolated from the slave output. In this way the number of slaves is limited only by the available power from the master. In our set up the injection light is double passed through a 200 MHz center-band frequency deflector with a 100 MHz bandwidth thereby allowing us to sweep the frequency of the slaves over 200 MHz.

3.2 The Dipole Traps

The dipole force traps investigated in this thesis were all formed from a single CO_2 laser outputting up to 30W of power with a wavelength of 10.6μm. The setup used for the 3D lattice is shown in Fig 3.4 with the other setups being somewhat similar. Each beam is sent through an AOM which is used to control the power and provide isolation to the laser from the return beam when working with lattice traps. The beam is then passed through a one to one telescope formed using two 2.5 inch focal length ZnSe lenses. The beam then enters the chamber through a ZnSe window where it is focused and then recollimated by a pair of aspheric 1.5 inch focal length ZnSe lenses inside the chamber. A lattice can be formed by simply retro-reflecting the beam. The purpose of the external telescope is to correct the beam divergence before entering the chamber so that the output beam from the chamber is well collimated. While such collimation is not so crucial for the single focus and cross traps, the formation of a lattice requires that the focus of the input beam be well overlapped with the focus of the return beam. In addition the external telescope also provides a point at which to spatially filter the beam if required. The power is controlled by controlling the power in the 40MHz RF signal which drives the AOM. This power is generated by an HP signal generator and passed through an RF switch to a variable gain pre-amp. It is then passed to a high power amplifier which drives the AOM. This setup allows us to control the beam power in three distinct ways. Firstly, the beam can be shut off in $< 1\mu s$ by simply cutting the power with the RF switch. This is useful for time of flight measurements where rapid switching is needed to maintain the integrity of the measurement. Secondly, the power from the generator can be modulated directly at up to $\sim$ 80 kHz with an external signal. This is used to determine the trap frequencies by parametric excitation. Finally, the gain of the pre-amp can be modulated up to $\sim$ 1 kHz. This is used to set the dc component of the beam power and to ramp down the power for forced evaporation.

When ramping down the power one needs to bear in mind that both the modulators and the pre-amp are inherently nonlinear so that the control voltage is in no way proportional to the beam power. Thus accurate control of the ramp down requires one to correct this nonlinearity which is easily achieved by the LabView software used to interface the experiment. Essentially all one needs to do is measure the beam power at a range of

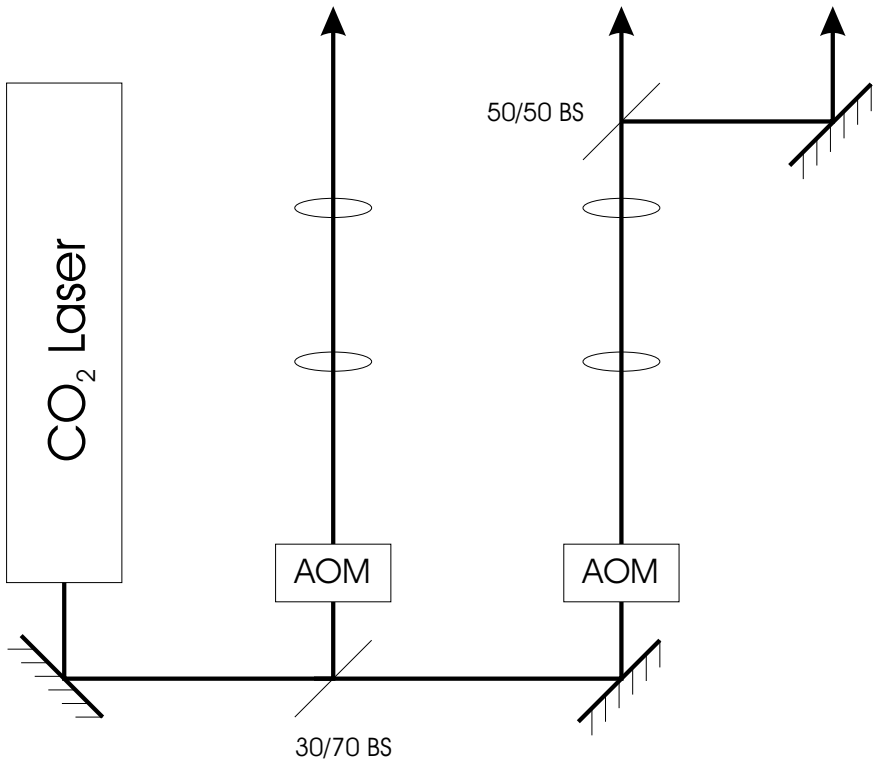

Figure 3.4: Basic set up of the CO_2 laser optics

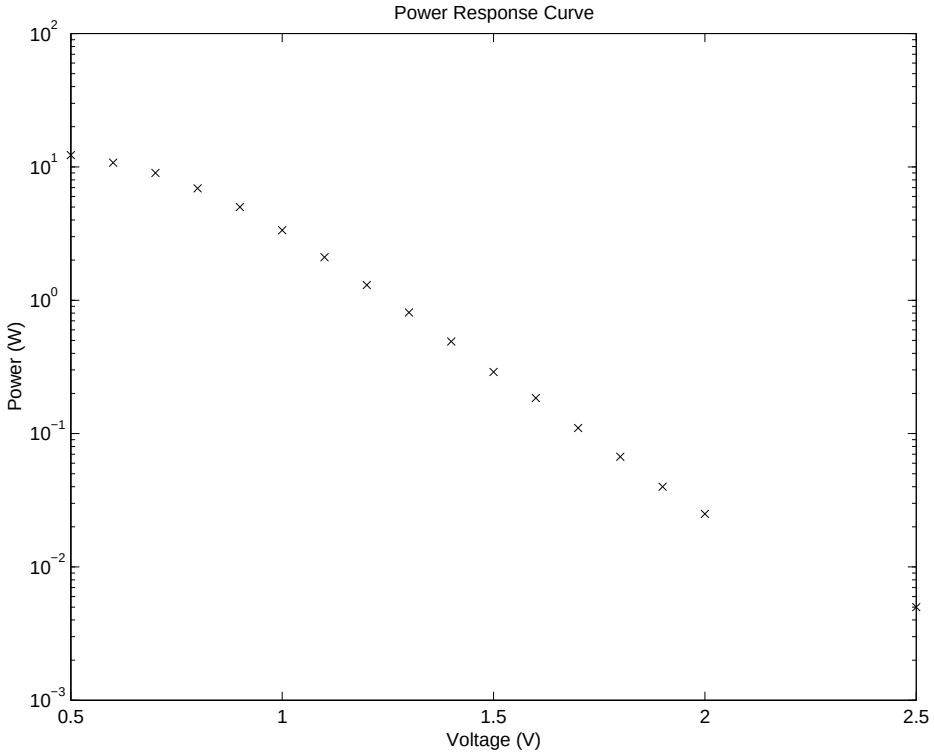

Figure 3.5: Typical response curve showing laser power vs control voltage. For clarity plot is shown on a semi-log plot.

voltages and use an interpolation function to find the voltage required to achieve a desired power. Fig 3.5 shows a typical response curve.

3.3 The MOT

In chapter two we discussed the operation of the MOT, and here we outline the details of the setup. The level structure of ^{87}Rb is shown in Fig 2.2. The MOT beams used to drive the $F = 2$ to $F' = 3$ transition come from the slave lasers whose setup was described above. Off resonant excitation of the $F = 2$ to $F' = 2$ transition pumps the atoms into the $F = 1$ state and so a repump laser, locked to the $F = 1$ to $F' = 2$ transition, is used to pump the atoms back into the MOT cycle. The power in each beam is controlled with an AOM and is delivered to the chamber via a single mode, polarization maintaining fibre, with the repump

light sharing the same fibre as one of the MOT beams to ensure good spatial overlap. Each MOT beam has a peak intensity of $\sim 8\text{mW/cm}^2 = 5\text{I}_{\text{sat}}$ and its gaussian profile with a waist of 1.4 cm is clipped to a diameter of $\sim$ 2 cm. The repump laser, being overlapped with one of the MOT beams, has the same spatial characteristics but has a peak intensity of about 3.4I_{sat}. The master laser, used to control the slaves, is locked to a frequency such the the MOT beam detuning, Δ, can be swept from resonance to 200 MHz to the red of the $F = 2$ to $F = 3$ transition.

3.4 Loading and Aligning

Loading ^{87}Rb into a dipole force trap is a relatively straight-forward procedure and is described in [9]. Briefly, atoms are collected in a MOT for 5 seconds, and then the repump intensity is reduced to $\sim 2.5\mu\text{W/cm}^2$. After a 20 ms delay, the detuning of the MOT beams is shifted $\sim$ 140 MHz to the red for a duration of 40ms at which time all beams and magnetic fields are extinguished. While this procedure is straight-forward, successful loading requires the MOT to be carefully aligned with the CO_2 laser beams and, in the case of multiple beam geometries, these beams must intersect at their focal points to within the resolution limits of the imaging system ($\sim 10\mu$m). As these beams are focused by lenses located inside the chamber, at least 5 inches from the ports, alignment of the beams can become a rather tedious exercise. Although procedures for alignment can be found in the literature, these procedures tend to be needlessly complicated and we adopt a more pragmatic approach.

Initial alignment begins by ensuring the CO_2 beams are centered and perpendicular to the focussing optics. This is accomplished using a HeNe beam tracer which is overlapped with the CO_2 beams. Since ZnSe is not AR coated for 633nm each surface of the lens reflects the tracer giving rise to interference rings in the reflected light. Only when the beam is correctly centered will these rings be centered on the optic axis. Once this is done the MOT is then centered on the travelling wave dipole trap. This is done by monitoring the position of both from two orthogonal directions and positioning the MOT coils so that the center of both MOT and trap coincide. In the extreme case in which the MOT is so poorly aligned that the trap cannot be loaded, the MOT can be imaged along the axis of the CO_2 beam [1].

[1] This is only possible if the lenses are made of ZnSe which has a reasonable transmittance at 780nm

When the image is centered in this fashion we have always found sufficient overlap to allow the dipole trap to be loaded.

The next step in the alignment is to intersect the dipole traps which can be done by monitoring their positions from two orthogonal angles and walking the trap using two external mirrors. This is not exactly ideal as it results in off axis propagation through the lenses introducing unwanted beam aberrations. Unfortunately this is unavoidable with the lenses being located inside the chamber.

3.5 Diagnostics

We now turn our attention to the diagnostic techniques used throughout this work. We begin with a discussion of the imaging system. This has evolved throughout the duration of this work, but the resolution of any imaging system used is limited by the chamber to $\sim 5\mu$m. Since this is typically larger than the size of a trapped sample *in situ* imaging is not feasible and so we rely on time of flight techniques. Furthermore fluorescent and absorptive imaging techniques have been sufficient for our purposes. Well number and temperature are readily extracted from images of ballistic expansion, density and phase space density have to be inferred. For these we require a knowledge of the trap oscillation frequencies which may be obtained via parametric excitation. We finish the section with a discussion of this technique.

3.5.1 Imaging

The principle difference between fluorescent and absorptive imaging techniques is the manner by which the scattered photons are detected. In fluorescent imaging, atoms are typically driven to saturation and the scattered photons are imaged onto the detector. Using the known solid angle subtended by the imaging optics the total number of scattered photons can be deduced from the number collected. In contrast, absorptive techniques measure the number scattered photons more directly by illuminating the atoms with a laser beam and imaging the shadow cast by the atoms. In either case the imaging optics remain the same and a typical set up is shown in Fig 3.6. In this set up a one to one imaging relay is made

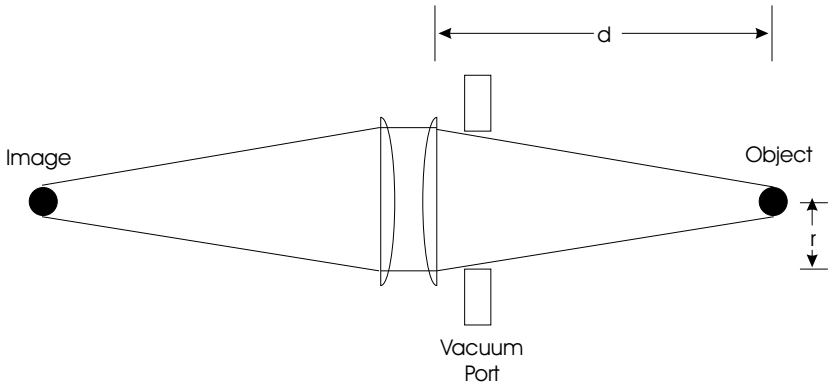

Figure 3.6: Diagram illustrating a typical imaging setup.

using two 200mm achromatic. This is typically following by a second imaging system to provide magnification.

Fluorescence imaging

In our system fluorescence imaging is implemented by pulsing both the trapping and repump beams on for a time $\tau = 100\mu$s with the MOT beams shifted into resonance with the $F = 2 \rightarrow F = 3$ transition. The resulting fluorescence is then imaged onto an ICCD camera. The use of an intensifier reduces the resolution by about a factor of three but the increase in gain more than makes up for this drawback. Since the MOT beams each have a maximum intensity of $5I_{sat}$ the atoms are driven well into saturation and the signal is thus insensitive to intensity fluctuations in the beams. The total counts accumulated on the CCD array is then given by

$$n = N\frac{\Gamma\tau}{2}\left(\frac{r}{2d}\right)^2\eta \tag{3.1}$$

where N is the number of atoms, r and d are as shown in Fig 3.6 so that the term in brackets is just the collection efficiency of the imaging optics. We note that if the chamber limits the collection efficiency then r and d are determined by the vacuum port. η is the efficiency of the camera expressed in units of counts per incident photon which can be measured directly by determining the count rate from a known power source. Thus the integrated signal is a direct measure of the number of atoms and the dominant source of error comes from the

estimation of the collection efficiency of the optics.

Temperature measurements can also be extracted from the same images. As shown in [91] the ballistic expansion of a thermal cloud with an initially gaussian density profile results in a gaussian distribution with an rms spread given by

$$\sigma_t^2 = \sigma_0^2 + \frac{kT}{m}t^2 \tag{3.2}$$

where t is the expansion time. Since the initial spread is given by $\sigma_0 = \sqrt{kT/(m\omega^2)}$ this equation can be written as

$$\sigma_t^2 = \frac{kT}{m}t^2\left(\frac{(\omega t)^2}{1+(\omega t)^2}\right) \tag{3.3}$$

Thus if $t > T_{osc}$ where T_{osc} is the trap oscillation period then the initial size of the cloud can be neglected, and this is always the case in our experiments. In measuring temperature this way one should bear in mind that the probing induces a blurring of the image given by $\sqrt{N_p/3}v_{rec}\tau$ where v_{rec} is the recoil velocity, and N_p is the number of photons scattered per atom, see [51, pg 29]. This is typically less than the resolution of the imaging system and, as such, can be neglected.

Absorptive imaging

As the signal to noise levels from fluorescence images decreases it becomes necessary to move to absorptive imaging. The following discussion closely follows that found in [51]. As the probe beam passes through the cloud the intensity diminishes according to Beer's law

$$\frac{dI}{dz} = -n\sigma_0 I \tag{3.4}$$

where n is the density profile, and σ_0 is the scattering cross-section. It is implicitly assumed that the probe intensity is less than the saturation intensity so that saturation effects can be neglected. Thus the intensity profile of the probe after propagation through the cloud is given by

$$I(x,y) = I_0(x,y)\exp(-\tilde{n}\sigma_0) \tag{3.5}$$

where $\tilde{n}$ is the integrated density or column density. This profile gives rise to an image profile given by

$$S(x,y) = S_0(x,y)\exp(-\tilde{n}\sigma_0) + S_b(x,y) \tag{3.6}$$

where $S_b(x, y,)$ is the contribution of background light not associated with the probe and we have neglected the small contribution due to probe scatter. Generally useful information cannot be extracted from this single image since multiple reflections in the beam path and flawed optical elements can severely distort the quality of the image. Thus two additional images are used in the processing: a bright field image $S_0(x, y)$ where the probe is imaged without the presence of the trapped atoms, and a dark ground image $S_b(x, y)$ with no atoms or probe. These three images are then combined to give the transmission $\tilde{T}$ via

$$\tilde{T} = \frac{S(x, y) - S_b(x, y)}{S_0(x, y,) - S_b(x, y)} \tag{3.7}$$

We have found that the dark ground need only be taken once over many runs whereas reliable results require a bright field image to be taken immediately after every absorptive image[2]. This minimizes the effects of vibration and movement responsible for degradation of image quality.

The number of atoms can be obtained by integrating over the column density which is given by $\tilde{n} = -\ln(\tilde{T})/\sigma_0$. In terms of the digitized image we thus have

$$N = -\frac{A}{\sigma_0} \sum_{pixels} \ln(\tilde{T}) \tag{3.8}$$

where A is the scaled pixel size. Temperature measurements can be extracted from $\tilde{n}$ as done for fluorescence imaging above. We note at this point that we have not included the effects of Bose-statistics on the data analysis. Nearing critically the distribution deviates from a gaussian distribution as discussed in [82]. We defer a discussion of this effect to chapter 5 where we discuss the cross trap in which condensation is achieved.

3.5.2 Parametric Resonance

Once number and temperature have been obtained a simple calculation involving the trap frequencies gives reasonably fair estimates of density and phase space density. In order to measure these frequencies we use a standard technique in which the trap depth is modulated sinusoidally [32]. Since the frequencies of the trap scale as $\omega \propto \sqrt{U_0}$, the governing equation in the harmonic oscillator limit is

$$\ddot{x} = -\omega^2(1 + \epsilon \sin(\omega_m t))x \tag{3.9}$$

[2]immediately means as fast as possible which, for a slow scan CCD camera this is about 0.5 seconds

where ϵ denotes the strength of the perturbation. It is well known that such a system exhibits parametric resonances in which the energy of the system grows exponentially when the driving frequency ω_m satisfies $\omega_m = 2\omega/n$ where n is a positive integer [54]. Thus one would expect trap losses when the trap depth is modulated at these frequencies. However, it can be shown that the widths of these resonances scale as $\epsilon^n\omega$ so that in practice only the first two are typically seen. Furthermore it has been shown [46] that the anharmonic nature of the trap can give rise to a slight discrepancy between the measured resonance frequencies and those expected from the harmonic approximation. This is simply a consequence of the oscillation frequency being a function of energy as shown in Fig 3.7. As this frequency shift is typically less than 10% we generally find reasonable agreement between the measured spectra and that expected from the harmonic oscillator model. For this reason we do not concern ourselves with this small correction. Experimentally, modulation of the trap depth is achieved by directly modulating the power in the beam. Since this is achieved by modulating the power to the AOM one needs to consider the nonlinearity of the device. Obviously one cannot modulate the power sinusoidally when operating at maximum deflection efficiency of the device. Thus measurements are performed at a reduced power such that the device operates in an approximately linear fashion. Results for other powers are typically inferred from the fact that $\omega \propto \sqrt{P}$.

As an illustration of the technique we consider parametric excitation in a 1D lattice which has a potential given by

$$U = \frac{U_0}{1 + (z/z_r)^2} \exp\left(-2\frac{r^2}{w_0^2(1 + (z/z_r)^2)}\right) \cos^2(kz) \tag{3.10}$$

where w_0 is the waist of the beam, $z_r = \pi w_0^2/\lambda$ is the Rayleigh range or collimation distance, and $k = 2\pi/\lambda$ is the wave number. The potential is thus a 1 dimensional array of minima with a spacing of approximately $\lambda/2$ and the divergence of the beam gives rise to a variation of the frequencies across the array. Specifically the minimum located at $z = 0$ is characterized by the frequencies

$$\omega_L^0 = \sqrt{\frac{4U_0}{mw_0^2}} \quad \text{and} \quad \omega_H^0 = \sqrt{\frac{2U_0k^2}{m}}. \tag{3.11}$$

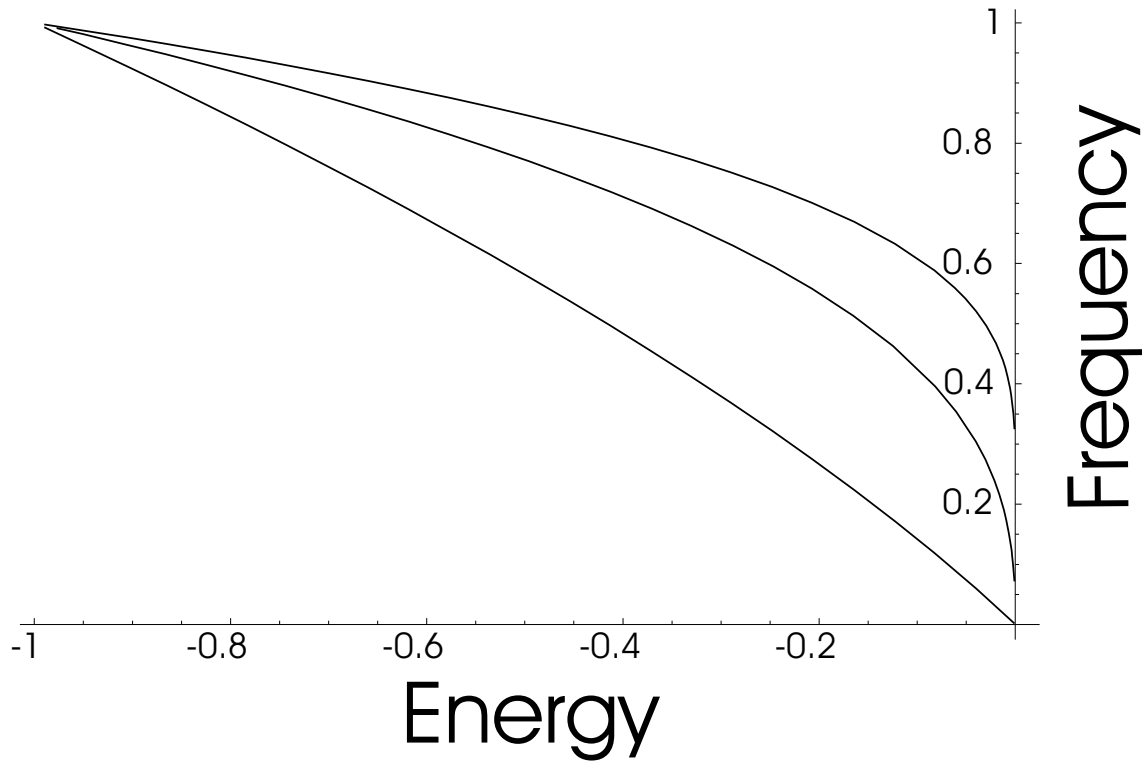

Figure 3.7: Curves showing variation of oscillation frequency with energy. Energy is normalized to the trap depth and frequency is normalized to that at the bottom of the trap. Curves shown from top to bottom are for gaussian, sinusoidal and lorentzian potentials.

whereas the minima located at $z = z_j$ has frequencies given (approximately) by

$$\omega_L^j = \frac{\omega_L^0}{1 + (z_j/z_r)^2} \quad \text{and} \quad \omega_H^j = \frac{\omega_H^0}{\sqrt{1 + (z_j/z_r)^2}} \tag{3.12}$$

It should be noted that these expressions differ from those given in [32] which are obviously incorrect. By spatially resolving the fluorescence from the trap we can observe this dispersion directly and Fig 3.8 shows typical series of images. These images can be integrated transversely to obtain the number of atoms as a function of position along the trap and, by taking images over a range of modulation frequencies, we can obtain atom number as a function of both position and frequency. Fig 3.9 illustrates the low frequency results and Fig 3.10 illustrates the high frequency. For the low frequency steps of 10Hz was used between 200Hz and 800Hz and 20Hz steps between 800Hz to 2000Hz. For the high frequencies 500Hz steps were used for the entire 10kHz to 40kHz range. The frequency dispersion is clear and, in addition, the smaller width associated the $n = 2$ resonance is also evident.

From the above expressions for the central frequencies it is easily shown that the ratio of these frequencies is a direct measure of the beam waist. For the data shown we obtain $\omega_L^0 = 2\pi\,550\,\text{Hz}$, $\omega_H^0 = 2\pi\,16\,\text{kHz}$, giving $w_0 = 69\mu\text{m}$ and $z_r = 1.43\text{mm}$ in good agreement with the values expected from the 4W beam used in the experiment. By way of comparison in Fig 3.11 and Fig 3.12 we show the spectrum based on total atom loss as done in [32]. For the purposes of clarity we have plotted the high and low frequency components on separate plots and used a linear scale. The difference in frequencies obtained via the two methods is $\sim 10\%$. Given the technical simplicity of monitoring total fluorescence this is clearly the better technique although resolving the frequency spread aids in alignment of the return beam. Essentially if the return beam is not well overlapped the symmetry seen in the figures is broken. This is particularly true for the low frequencies where even a small discrepancy in alignment can split the degeneracy of the lowest frequencies. As a final remark on parametric excitation we would like comment on the strength of the modulation needed to induce the effect as a large range of strengths are mentioned throughout the literature. Generally we have found a modulation strength of only a few percent is needed to induce significant trap loss at 2ω which suffices to determine the frequency of the trap. If the intent is to observe the resonance at ω a stronger modulation is needed to compensate the reduced resonance width mentioned above. The situation for multiple traps, such as in the 1-D

Figure 3.8: Typical series of images taken after parametric excitation. Excitation frequencies start at 12kHz and increase from left to right in 2kHz steps.

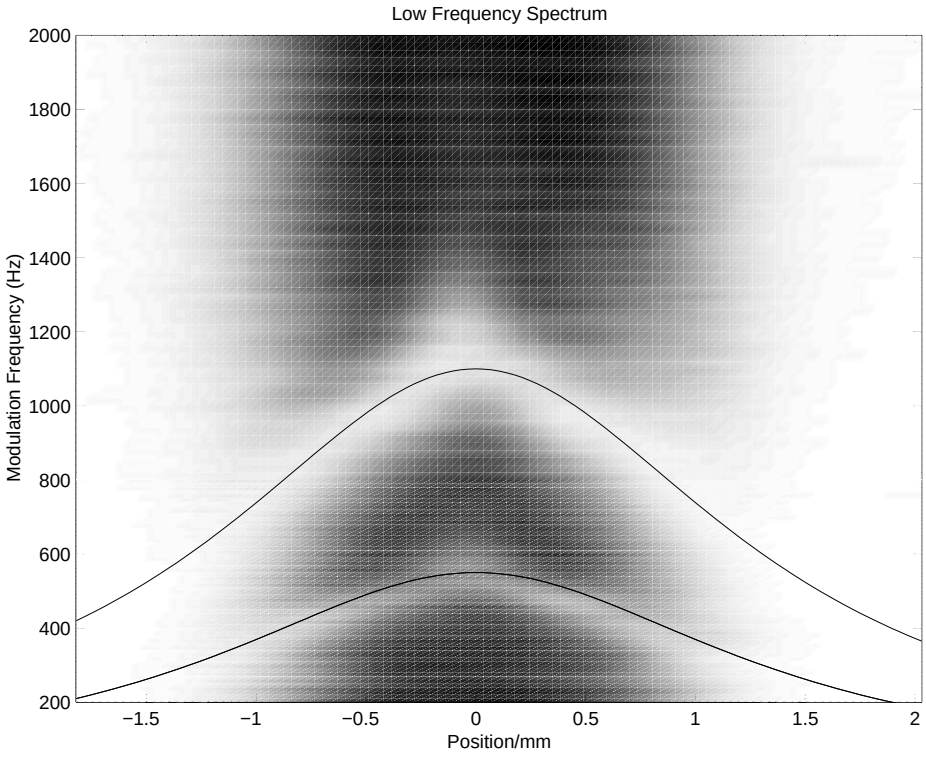

Figure 3.9: Density plot illustrating frequency dispersion of the transverse frequencies. Curves are the expected dispersion based on the measured central frequencies - see text.

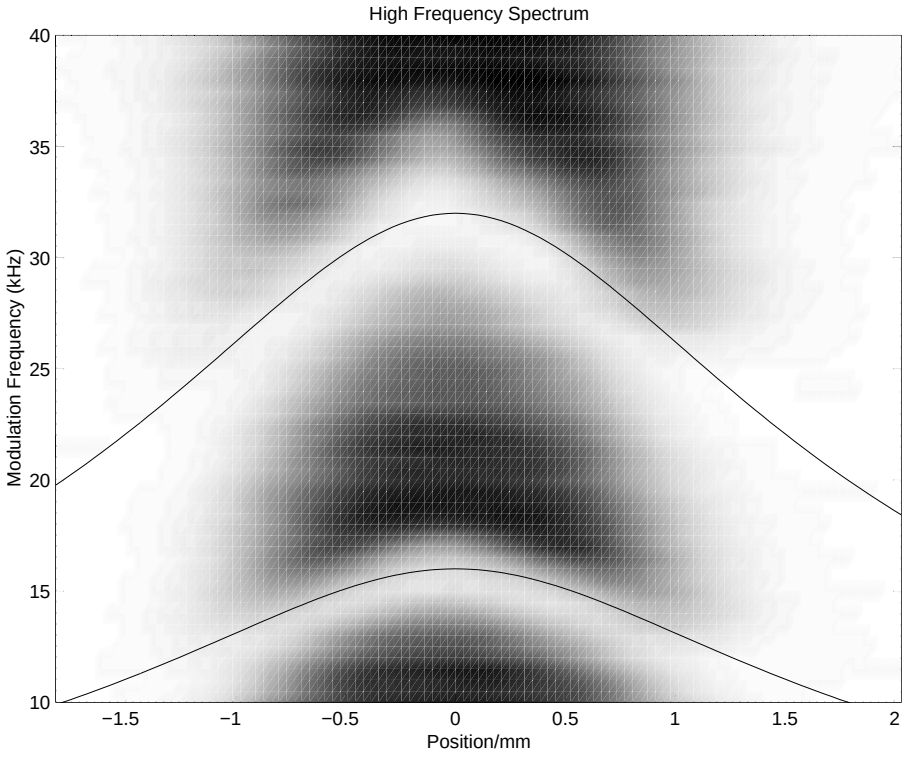

Figure 3.10: Density plot illustrating frequency dispersion of the longitudinal frequencies. Curves are the expected dispersion based on the measured central frequencies - see text.

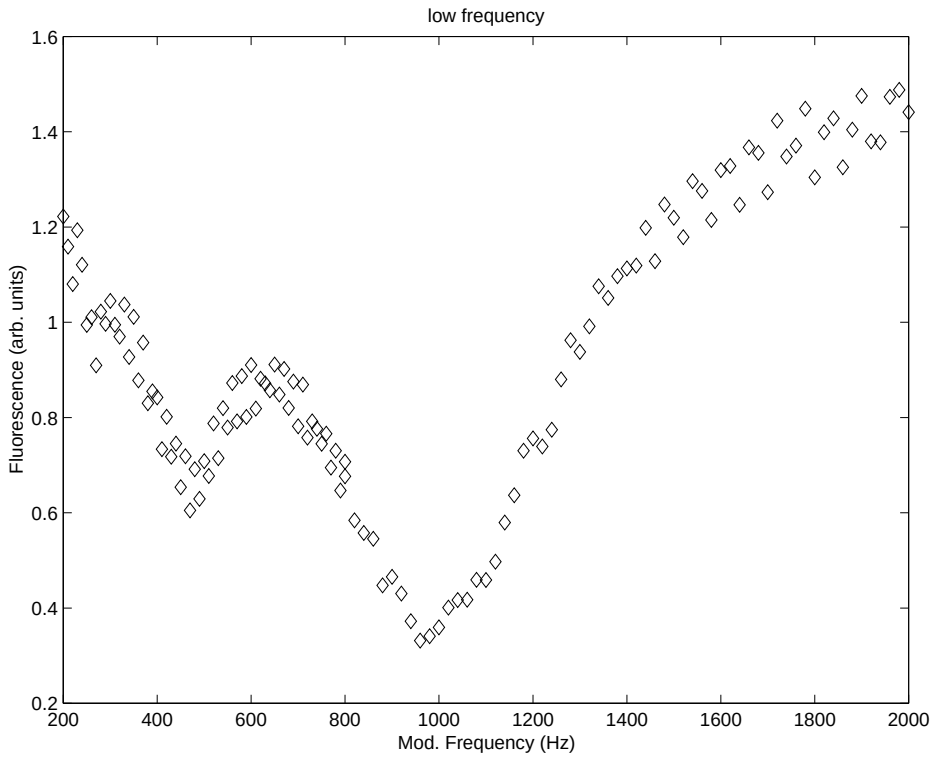

Figure 3.11: Low frequency spectrum based on total fluorescence.

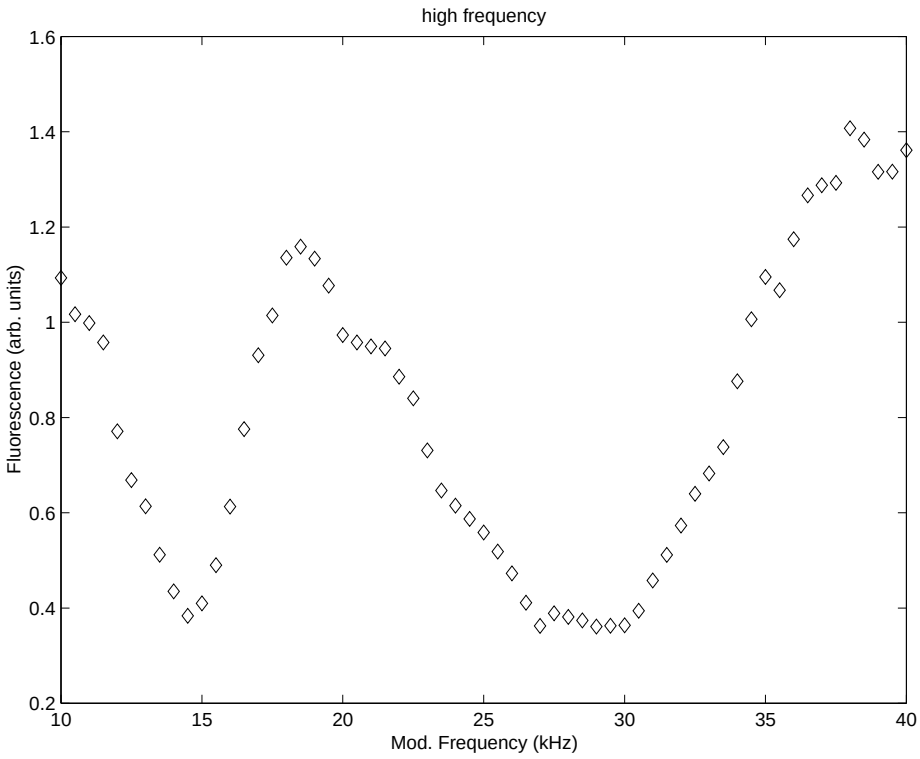

Figure 3.12: High frequency spectrum based on total fluorescence.

lattice case discussed above, the situation is complicated by the limits of ones resolution. Basically, if the modulation is too small, trap losses may only occur in a limited number of traps such that the finite resolution of the imaging obscures the effect. To illustrate, consider the above experiment. The band of frequencies $\Delta\omega$ present in a region of spatial extent Δz, centered at z, can be found by considering the differential of the expressions for frequency given above. We find

$$\frac{\Delta\omega_H}{\omega_H} = -\frac{z}{z_r}\frac{1}{1+(z/z_r)^2}\frac{\Delta z}{z_r} \tag{3.13}$$

and

$$\frac{\Delta\omega_L}{\omega_L} = -\frac{2z}{z_r}\frac{1}{1+(z/z_r)^2}\frac{\Delta z}{z_r}. \tag{3.14}$$

Thus in order to observe losses a stronger modulation (by a factor of two) is evidently needed for the lower frequencies. Furthermore the resolution of the imaging system used at the time was very poor ($\sim 300\mu$m ~ 0.25z$_r$) so that fairly strong modulation would be needed to see the effect. Indeed the in the above experiment a 50% modulation was needed at low frequency and a 30% modulation at high frequencies. In the work that follows we use a greatly improved imaging system and we are solely concerned with the determination of trap frequencies. Thus we typically use a modulation strength of a few percent.

Chapter 4

Initial Experiments

The experimental setup described in the previous chapter has allowed us to explore a variety of trap geometries. In this chapter we discuss our initial investigations that led us to the cross beam geometry used to create the condensate. We begin with a 3-D lattice structure created by intersecting 3 1-D intensity lattices. This trap provides tight confinement ($\sim$ 30kHz) in all directions lifting the ground state energy to approximately 1μK. Furthermore the level spacing associated with these frequencies exceed the photon recoil energy making it a plausible candidate for resolved raman side-band cooling. For reasons to be discussed, this idea was abandoned in favor of evaporative cooling. In sections 2 and 3 we present our initial studies of a single focus trap and a 1-D lattice, and in section 4 we make a comparison of the two geometries and speculate on the quantitative features of the data.

For the single focus and 1-D lattice geometries two sets of data will be presented: one set corresponding to a set up in which the maximum power available is 15W and the second set corresponding to a set up in which the maximum power is 24.5W. The reason for the difference is due to problems encountered with the lattice configuration particularly at high powers as illustrated by the striking example in Fig 4.1. No power modulation was applied and no satisfactory explanation for the structure has been found. Furthermore such effects were intermittent making it impossible to study the problem systematically. Two possible causes are mode hopping due to the poor temperature stability of the laser cavity and feedback due to the retro-reflected beam. The return beam is double shifted by the AOM and thus the AOM provides a reasonable degree of isolation due to the fact that the laser cavity is not resonant with the frequency shifted beam. However when operating at high powers the power isolation is pretty much non-existent and it is not clear that frequency isolation is all that is needed.

Figure 4.1: Image taken during a data run. No modulation to the laser power was applied and the observed structure was attributed to feedback.

In an initial attempt to alleviate the problem, (rough) temperature stabilization of the cooling water for the laser was implemented, and data relevant to this set up includes the highest powers available of 24.5W. We will refer to this as configuration A. While this alleviated the problem to some extent, intermittent problems still occurred making data collection a rather frustrating and tedious task. To further alleviate the problem a Michaelson interferometer was used to direct the return power away from the laser and we will refer to this as configuration B. It could be argued that deliberate misalignment of the return beam would suffice but the lattice requires fairly stringent requirements on alignment and so the retro-reflected beam inevitably finds its way back to the laser. The use of an interferometer gave more satisfactory long term performance but at the cost of a reduction in available power.

4.1 3-D Lattice

As we saw in chapter one, the potential energy in a QUEST is proportional to the intensity profile. In the case of a standing wave (1-D lattice) trap one can easily obtain frequencies on the order of ($\sim$ 30kHz) along the beam propagation axis and ($\sim$ 1kHz) transversely. By intersecting 3 mutually orthogonal lattices one can thus achieve $\sim$ 30kHz in all directions.

Neglecting the divergence of the beam, the potential energy for this 3-D structure is given by

$$U(x,y,z) = U_x^2 + U_y^2 + U_z^2 + \alpha U_x U_y + \beta U_y U_z + \gamma U_z U_x \tag{4.1}$$

where U_k is the square root of the potential energy due to the beam propagating along the k axis. The first three terms are just the contributions from the individual 1-D lattices and the remaining terms are due to interference effects and depend on the relative polarizations and phases in each beam. Since the wavelength is large (10.6μm) we initially relied on passive stability to keep the magnitude of the interference terms fixed. The polarizations were chosen for convenience [1] having the diagonal beams orthogonally polarized and the horizontal beam vertically polarized and all polarization vectors lie in a plane perpendicular to the propagation direction of the horizontal beam. With the diagonal beams being orthogonally polarized, one of the interference terms in the above expression vanishes.

In order to establish that one has a three dimensional lattice structure one needs to look for features unique to this geometry. With the presence of the interference term one such feature is the existence of a frequency larger than the maximum frequency exhibited by any one or two beam configuration. A typical result of a high frequency parametric excitation is shown in Fig 4.3 which shows the result both with and without modulation. With all beams present the central feature is removed by the modulation where as no such losses are seen if one or two of the beams are removed. However the spectrum, as shown in Fig 4.2, is broad band extending down to the lowest frequencies associated with the individual beams. And worse, a slow drift of the maximum frequency was noted indicating a drift in the relative phases.

The drift problem can be easily fixed simply by shifting the frequency of the horizontal beam relative to the others. This causes the interference terms to beat at the difference frequency of 80 MHz and are thus time averaged away. However the broad band nature of the spectrum still persists and some explanation is needed. To this end, consider the potential with the interference terms averaged away. Since the potential depends on the field strength from each beam it should be obvious that the frequency of any given trap

[1] Wave plates for this wavelength are not readily available and the polarization can only be changed by a judicious mirror arrangement

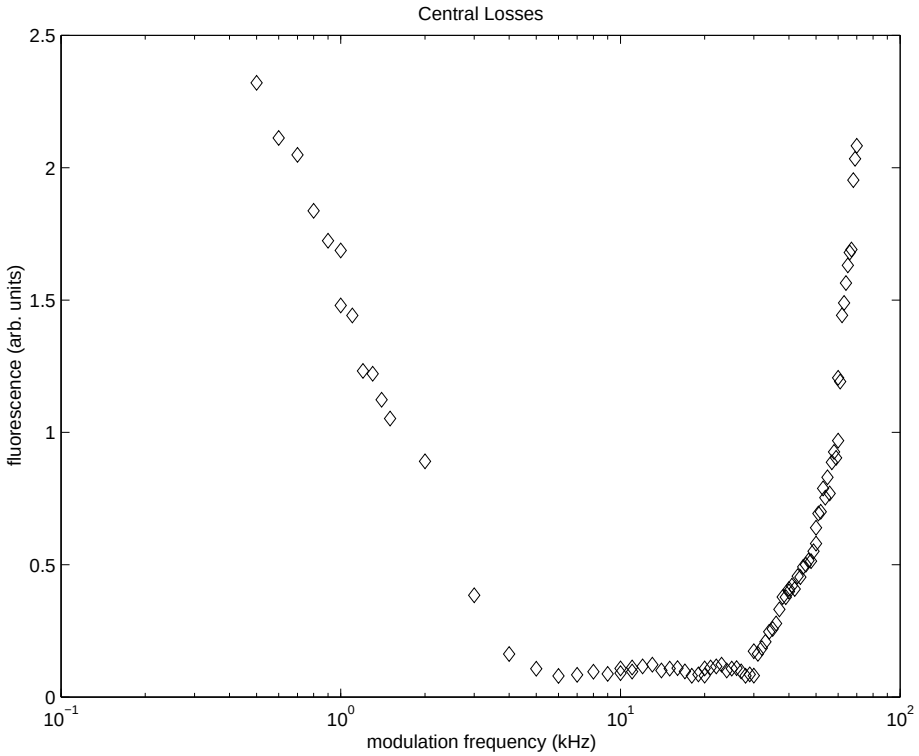

Figure 4.2: Spectrum of the 3-D lattice geometry. Trap inhomogeneity gives rise to a broad band loss

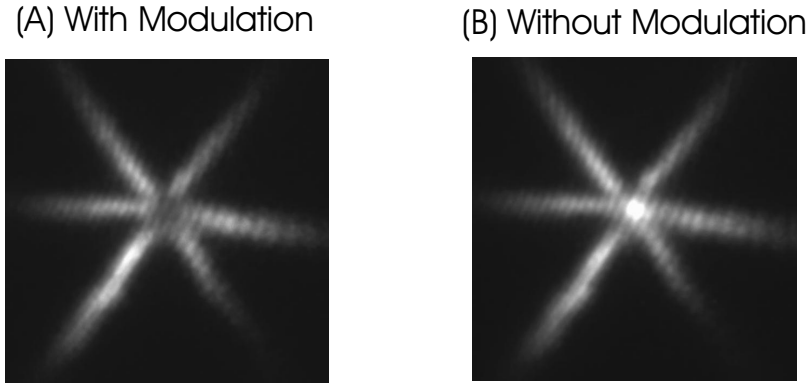

Figure 4.3: Images showing evidence of the 3-D structure. Image (A) shows the result after parametric excitation and image (B) shows the result without.

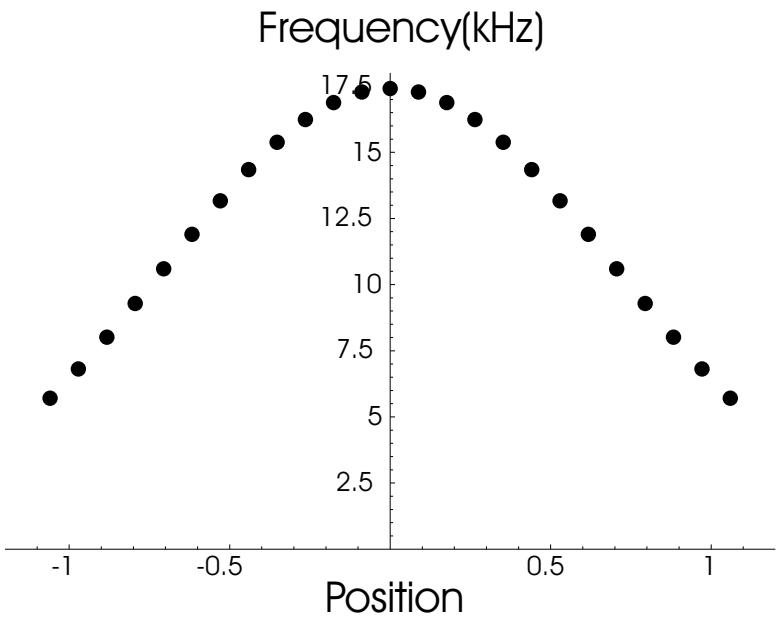

Figure 4.4: Plot illustrating the variation of trapping frequencies over length scales of the waist. Position is scaled by the waist of 60 microns and frequencies are in kHz.

varies considerably over length scales of the beam waist. In Fig 4.4 we show this effect by computing the minimum frequency for traps located along the axis of one beam. In addition we show in Fig 4.5 the contrast of these traps which we define as the depth of the well relative to the depth of the potential at the well minimum. The problem is almost obvious. Well the potential does describe a 3-D structure of tightly binding locations, the associated frequencies cover a broad band spectrum. Furthermore, the poor contrast means that an appreciable part of a thermal distribution will not be bound to these sites, but free to move over length scales of the waist. Under a low frequency excitation these atoms can gain sufficient energy to escape as verified by numerically integrating the classical trajectories. To more firmly establish this as a loss mechanism one needs to estimate the collision rate. In the absence of collisions only the weakly bound atoms would be removed whereas if the gas is collisionally dense the energy gained by these atoms would be constantly redistributed to the entire ensemble. Such an estimate is complicated by the presence of the wings and so they need to be removed. This is achieved by slowly and sequentially switching each beam off and then back on leaving only the intersection region from which number and

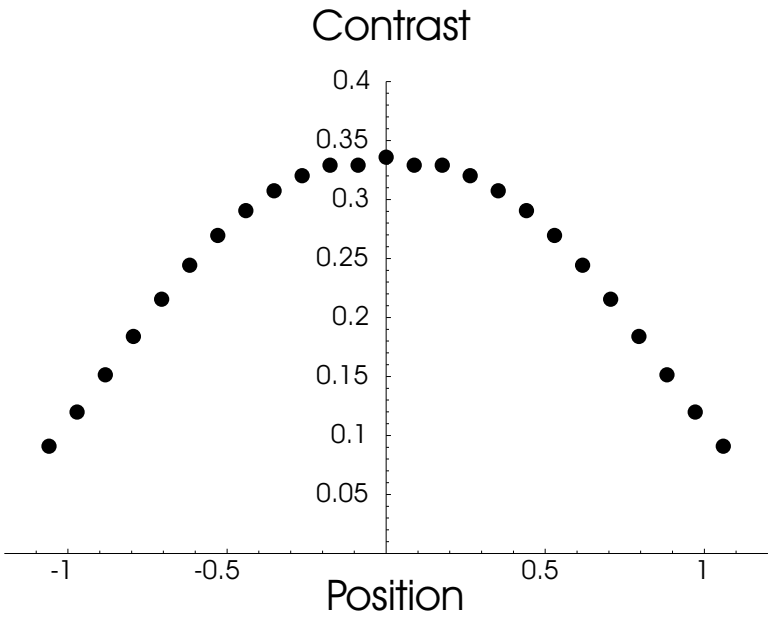

Figure 4.5: Plot illustrating the poor contrast of the 3-D lattice structure.

temperature measurements can be made in the usual fashion. We find that we have about 20000 atoms at a temperature of 25(2) μK and from the frequency measurements we can obtain a crude estimate of 10^{13}cm^{-3} for the density which gives a collision time of about 3 ms. Thus atoms would typically experience a collision before escaping serving to heat the entire ensemble.

At this point we decided to abandon the 3-D geometry and look for evaporation in simpler geometries that were somewhat easier to characterize.

4.2 Single Focus

The most simple trap to make is that of a single focus beam. A gaussian beam with a waist w_0, and Rayleigh range z_r gives a potential

$$U = \frac{U_0}{1+(\frac{z}{z_r})^2}\exp\left(-2\frac{x^2+y^2}{w_0^2(1+(\frac{z}{z_r})^2)}\right) \tag{4.2}$$

with frequencies

$$\omega_r = \sqrt{\frac{4U_0}{mw_0^2}}, \qquad \omega_z = \sqrt{\frac{2U_0}{mz_r^2}} \tag{4.3}$$

These frequencies can be measured using parametric resonance as discussed in the previous chapter. In configuration A we measured frequencies of $\omega_r = 2\pi 700(50)$Hz and $\omega_z = 2\pi 26(4)$Hz at a beam power of $19W$ and in configuration B we measured frequencies of $\omega_r = 2\pi 375(20)$Hz and $\omega_z = 2\pi 12(2)$Hz. The errors reflect the experimental uncertainty in determining where minimum loss occurs and not the uncertainty associated with the frequency shift caused by trap anharmonicity. The expressions in equation 4.3 can be easily rearranged to give the trap depth and the waist in terms of the measured frequencies and in this way we estimate a beam waist of 64μm and a trap depth of 210μK in configuration A and for configuration B a waist of 75μm and a trap depth of 80μK. These estimates are consistent with the independent expression

$$U_0 = \frac{\alpha_s}{2\epsilon_0 c}\frac{2P}{\pi w_0^2} \tag{4.4}$$

for the potential depth.

4.2.1 Trap Loading

Our loading procedure is essentially the same as that used by the Hänsch group in their investigations of a 1-D lattice geometry [32],[33], [77]. It begins by collecting approximately $40 \sim 100$ million atoms during a MOT loading period of $2 \sim 5$s. After this time the repump intensity is reduced to approximately $3 \sim 4\mu$W/cm^2 for 20 ms before detuning the MOT beams 140 MHz ($\sim 23\Gamma$) to the red of the $^2S_{1/2}$, F=2 - $^2P_{3/2}$, F=3 transition for a load time of typically 40 ms. At the end of the load time the repump light is shuttered and the MOT beams extinguished in 1ms. The 1 ms delay ensures all atoms are pumped to the F=1 ground state and the shutter ensures no further repumping occurs. Without the shutter we have found that stray light due to the finite extinction ratio of the AOM's is enough to drastically reduce the lifetime of the trap. The CO_2 laser remains on during the entire loading process.

The loading dynamics of an optical dipole trap has been extensively studied in a FORT detuned 4 nm to the red [53]. Well the scattering rate for such a trap is far greater than that in a CO_2 trap, the physics involved in the loading process remains the same. Essentially the loading was described by a loading rate determined by the MOT and a loss

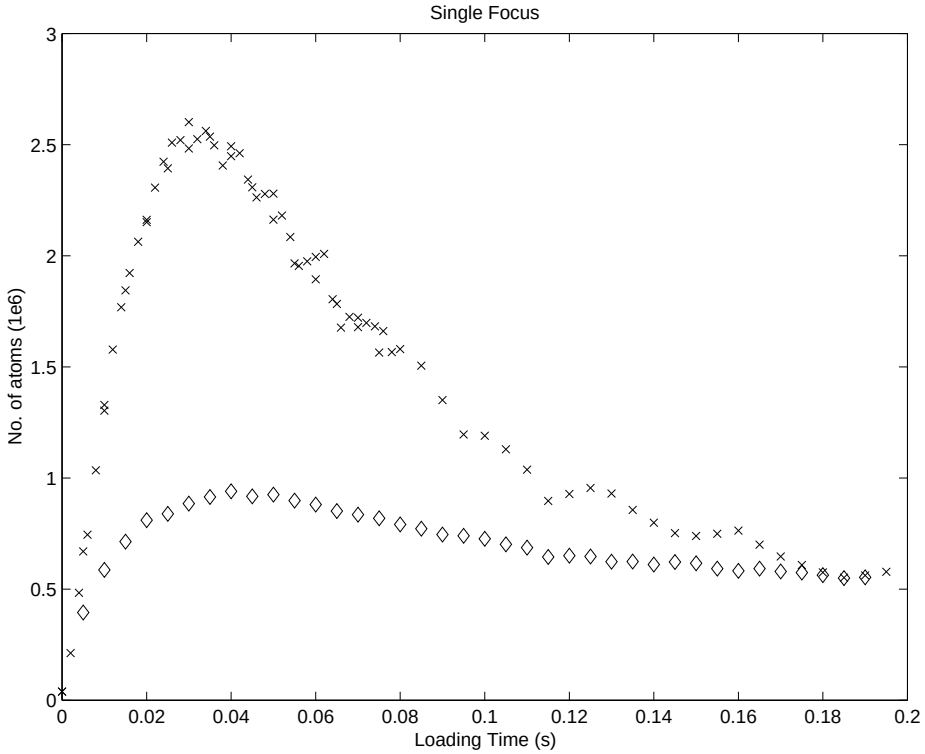

Figure 4.6: Plots showing number as a function of load time. Measurements were made 2 seconds after loading. Crosses correspond to data taken under configuration A and diamonds correspond to data taken under configuration B.

rate which was attributed to light assisted collisions induced by the MOT beams. The loss rate can be reduced by increasing the detuning of the MOT beams and reducing the repump intensity although this causes the MOT to dissipate resulting in a decay of the loading rate. Optimum loading thus requires a careful choice of repump intensity, MOT detuning and load time. We illustrate this in Fig 4.6 and Fig 4.7 by plotting the number and temperature of the atoms as a function of load time for a fixed detuning and repump intensity. The optimum load time is seen to be approximately 40ms and we note this to be somewhat independent of trap depth.

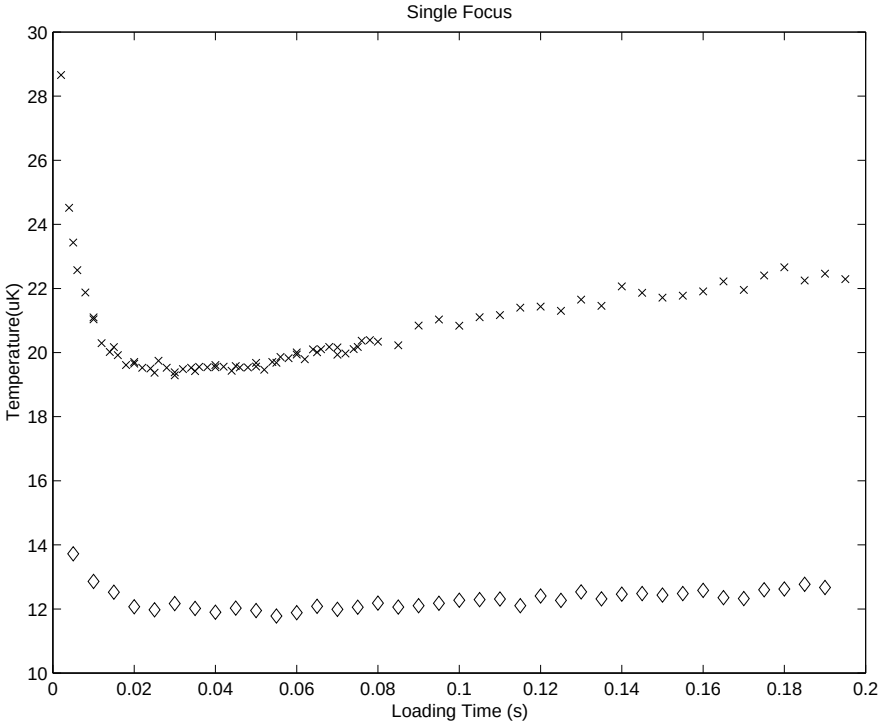

Figure 4.7: Plots showing temperature as a function of load time. Measurements were made 2 seconds after loading. Crosses correspond to data taken under configuration A and diamonds correspond to data taken under configuration B.

4.2.2 Lifetime and free evaporation

An important consideration for any trap is its lifetime as it determines the timescale over which experiments can be performed. An extensive discussion on the limiting factors for a CO_2 trap can be found in [71]. Essentially the major factors limiting the lifetime are background vacuum pressure and laser fluctuations in both amplitude and position. An ultra-stable laser design is used in [72] to obtain lifetimes of 5 minutes although very respectable results using the same model laser as used in this work is reported in [30]. Our modest vacuum setup limits our lifetime to a humble 10 seconds and a typical lifetime measurement is shown in Fig 4.8 taken under configuration B. The number and temperature measurements can be combined with the measured frequencies to determine the density, n and phase space density, ρ using the the harmonic approximations

$$n = N(\frac{m\omega^2}{2\pi k_b T})^{3/2}, \text{ and } \rho = N(\frac{\hbar\omega}{k_b T})^3 \tag{4.5}$$

In appendix B we give the exact expressions for these quantities and discuss the validity of the harmonic oscillator approximation. Essentially the true density is always smaller and, for the depths and temperatures discussed here, the difference could be as much as a factor of two. From these plots we can see clear evidence of evaporation in the first few seconds. Free evaporation has been seen in this type of trap before [72] but only on timescales exceeding a minute. It is a worthwhile exercise to apply the model discussed earlier. As we noted then the trap depth U_0 is treated as a free parameter and chosen to optimize the fit to the data. The curves given in Fig 4.8 uses a trap depth of $U_0 = 105\mu$K. This is not so different from the estimated 80μK mentioned earlier and the fit is surprisingly good considering the simplicity of model.

4.2.3 Properties vs. Trap Depth

The densities and phase space densities achieved in a single focus trap are not sufficient to warrant forced evaporation, particularly in view of the limited lifetime, but it is of interest to see how these quantities scale with power or equivalently trap depth. The measurements shown in Fig 4.9 to Fig 4.10 were obtained by shifting the power in the beam 250ms before loading commenced and probing the sample 2 seconds later. Of course properties we are

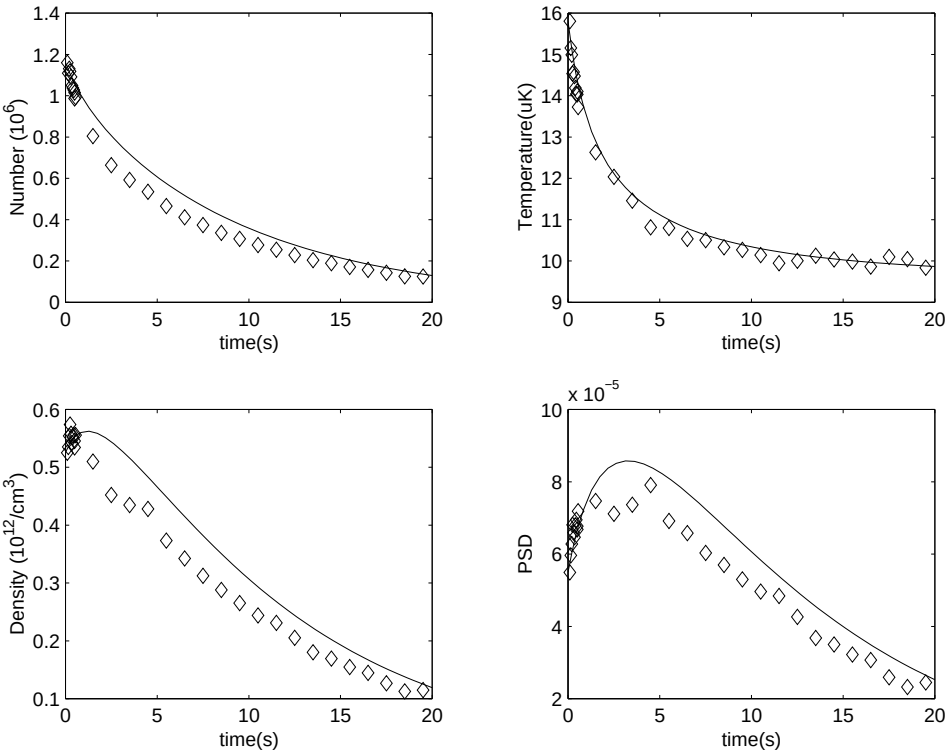

Figure 4.8: Plots showing the evolution of various quantities of interest with time. Data was taken under configuration B at 11W. The solid curves were obtained using the SHO model developed in an earlier chapter.

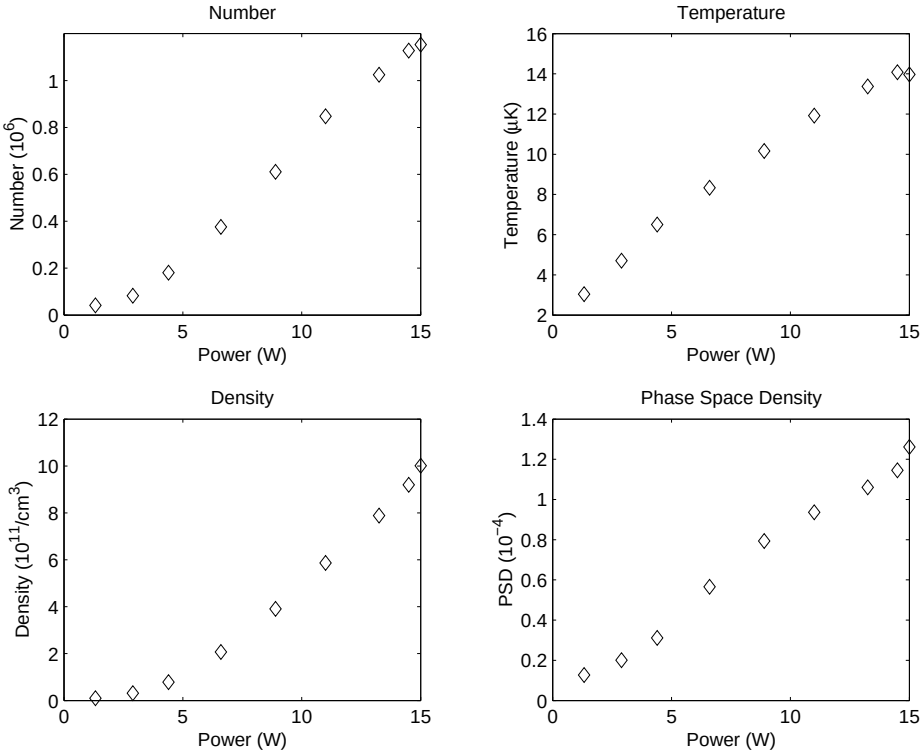

Figure 4.9: Plots showing the dependence of various properties on power. Data here is taken under configuration B.

measuring are dynamical as the lifetime curve above shows. However they do not change that dramatically on the 2 second timescale which was chosen so as to ensure thermal equilibrium at the lowest powers. In estimating the density and phase space density, the frequencies at different powers were inferred from the measurements at 19W and 11W for configurations A and B respectively, using the fact that the frequencies are proportional to the square root of the power.

Given the similarity in the number and temperature between the two data sets the larger difference in density and phase space density seems somewhat surprising. However these quantities are derived and depend on the third power of the mean frequency so at least some of the discrepancy can be attributed to modest errors in the measured frequencies. We also note the saturation of phase space density at the highest powers.

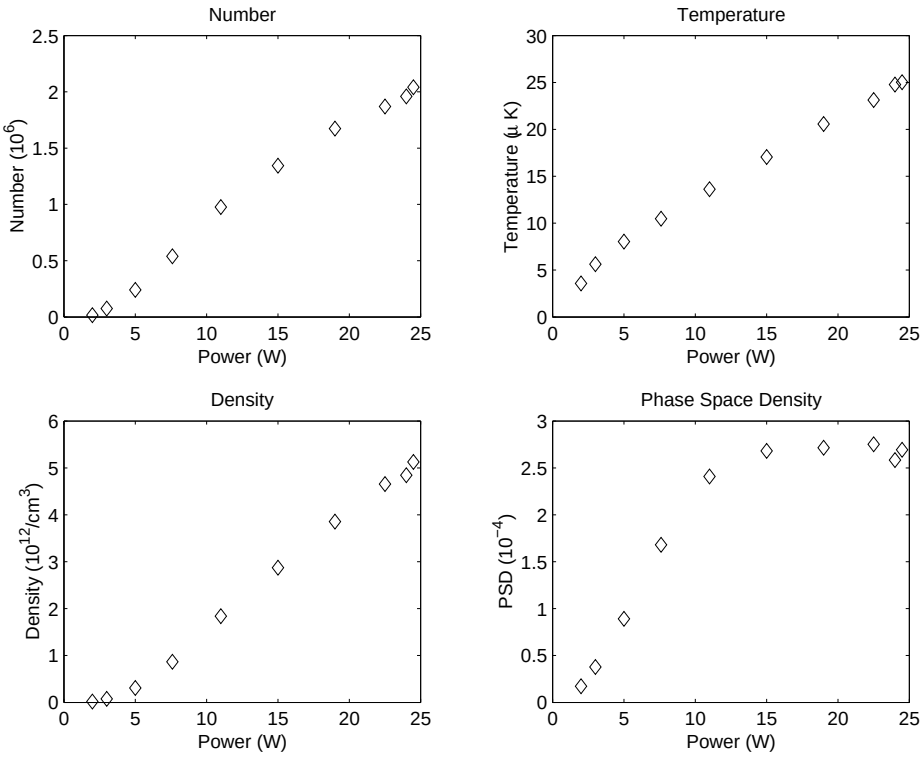

Figure 4.10: Plots showing the dependence of various properties on power. Data here is taken under configuration A.

4.3 1-D Lattice

By way of comparison, and in an attempt to generate greater trap depths and tighter confinement, the single focus trapping beam can be simply retro-reflected to generate a 1-D array of micro-traps. These traps have a depth four times greater than the single focus geometry, and the potential is given by

$$U = \frac{U_0}{1+(\frac{z}{z_r})^2} \exp\left(-2\frac{x^2+y^2}{w_0^2(1+(\frac{z}{z_r})^2)}\right)\cos^2(kz) \tag{4.6}$$

As seen in the previous chapter, the frequencies for each trap vary with position due to the divergence of the beam, and the central trap has frequencies

$$\omega_r = \sqrt{\frac{4U_0}{mw_0^2}}, \qquad \omega_z = \sqrt{\frac{2U_0k^2}{m}} \tag{4.7}$$

Using parametric resonance, the frequencies in this central region are measured to be 1.5 kHz and 39.5 kHz at a beam power of 19W in configuration A. For configuration B we measured frequencies of 800 Hz and 24 kHz at a power of 11W. Since these traps were formed by simply retro-reflecting the beam a number of consistency checks can be made. Firstly, the ratio of highest to lowest frequency should be the same for both single focus and lattice traps, and this ratio is a measure of the beam waist as mentioned earlier. Secondly, the ratio of the highest frequency of the lattice trap to the lowest frequency of the single focus trap is also a direct measure of the waist. Finally the trap depth for the lattice is expected to be four times as deep as the single focus so that lowest frequency of the lattice should be twice the highest frequency of the single focus trap. The three different estimates of the waist based on the frequencies all agree to within 5%.

4.3.1 Loading and lifetime

Details of the loading are exactly the same as for the single focus geometry and for comparison the number and temperature as a function of load time is shown in Fig 4.11 and Fig 4.12. The repump intensity and detuning is the same as that used in Fig 4.6 and Fig 4.7.

As one can see the optimum load time is essentially the same as for the single focus case despite the fact that the trap geometry is substantially different. This indicates that

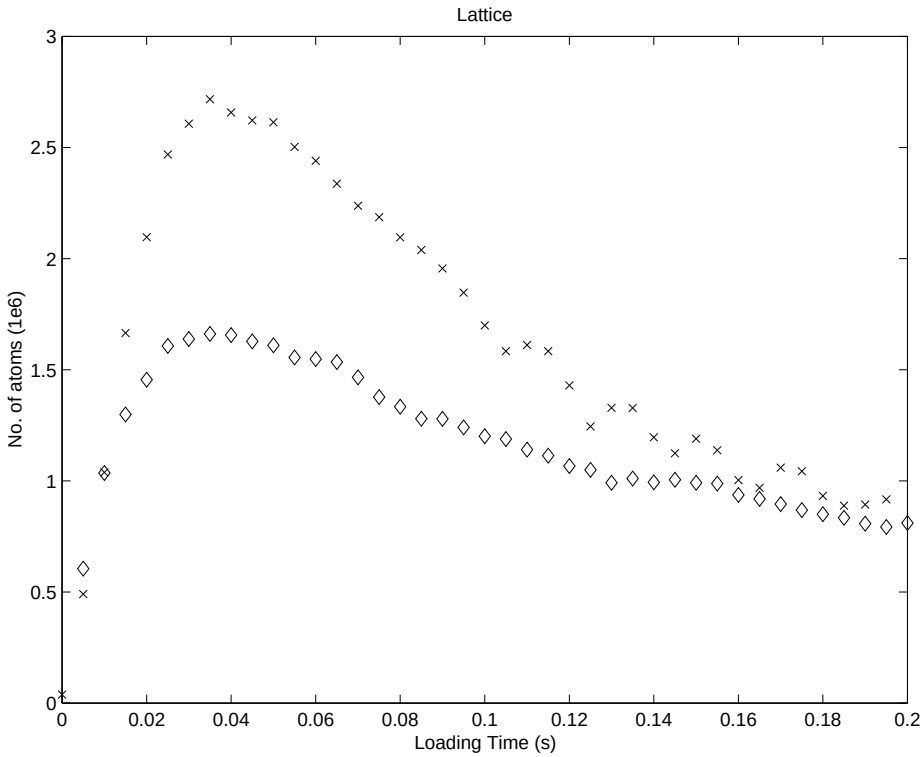

Figure 4.11: Plots showing number as a function of load time. Measurements were made 2 seconds after loading. Crosses correspond to data taken under configuration A and diamonds correspond to data taken under configuration B.

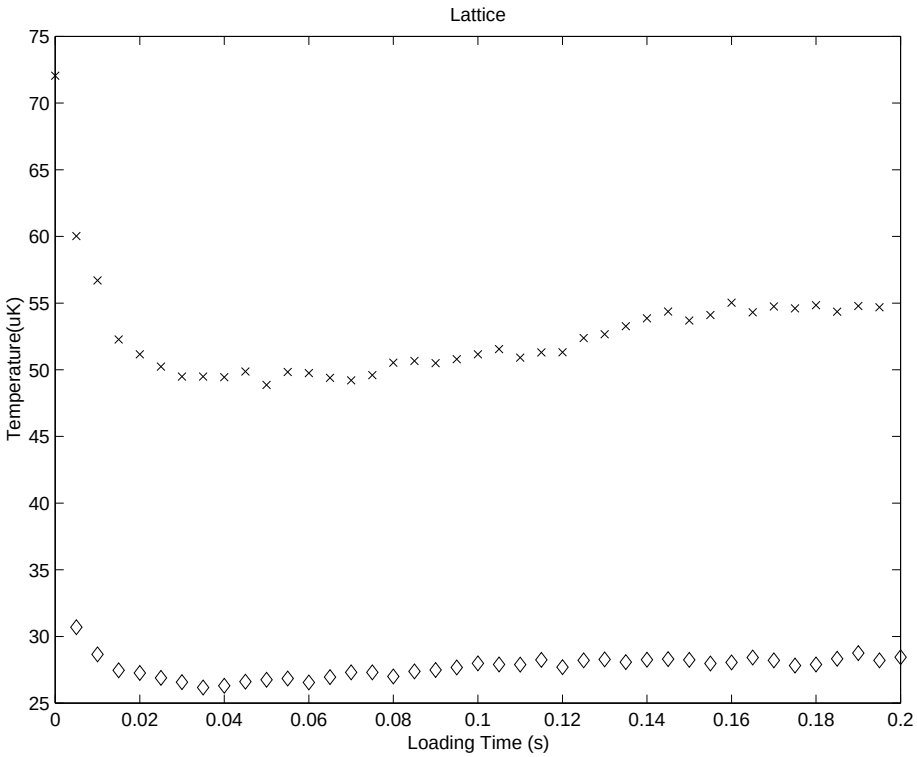

Figure 4.12: Plots showing temperature as a function of load time. Measurements were made 2 seconds after loading. Crosses correspond to data taken under configuration A and diamonds correspond to data taken under configuration B.

the loading mechanism is largely dependent on the MOT characteristics and not on trap geometry. Indeed the 40 ms is consistent with estimates of the MOT damping time.

We find a similar lifetime of $\sim$ 10 seconds and the analogous curves are given in Fig 4.13. Here we have shown data taken under configuration A as this was the only time we took measurements of the number per site during the lifetime measurement. Once again free evaporation is clearly evident and occurs on slightly shorter time scales due to the enhanced density and collision rate obtained using this geometry. As for the single focus case we have applied the model developed in the previous chapter. As the densities are significantly higher we have included the three body loss term[2], and best results are obtained using $U_0 = 630\mu$K which we note is significantly different than the estimated trap depth of 900μK. Much of this difference could be accounted for by modest errors made in the frequencies or beam mismatch between the input and return beam. Nevertheless the fit of the model is quite reasonable.

4.3.2 Properties vs. Trap Depth

In the interest of comparison between the single focus and lattice geometry we have investigated the dependence of the various properties on power as in the single focus case. In this case however the situation is complicated by the fact that the depth and frequencies associated with any given micro-trap depends on its position. In the previous section we saw that the temperature was approximately proportional to trap depth and so it would seem likely that the temperature would not be uniform across the entire array of traps. While it is found that most ($\sim 80\%$) of the atoms are located within the Rayleigh range of the beam where the trap geometry doesn't change substantially, the temperature measurements made in this section should perhaps be treated as a weighted average over the entire ensemble. As we are only interested in general trends at this point we do not concern ourselves overly with this technicality.

In order to estimate densities and phase space densities the expressions given in 4.5 require a knowledge of the number of atoms in an individual trap. As we are unable to resolve individual sites this quantity cannot be measured directly, and it is estimated from

[2]We note that the inclusion of this term makes only a slight difference to the fit.

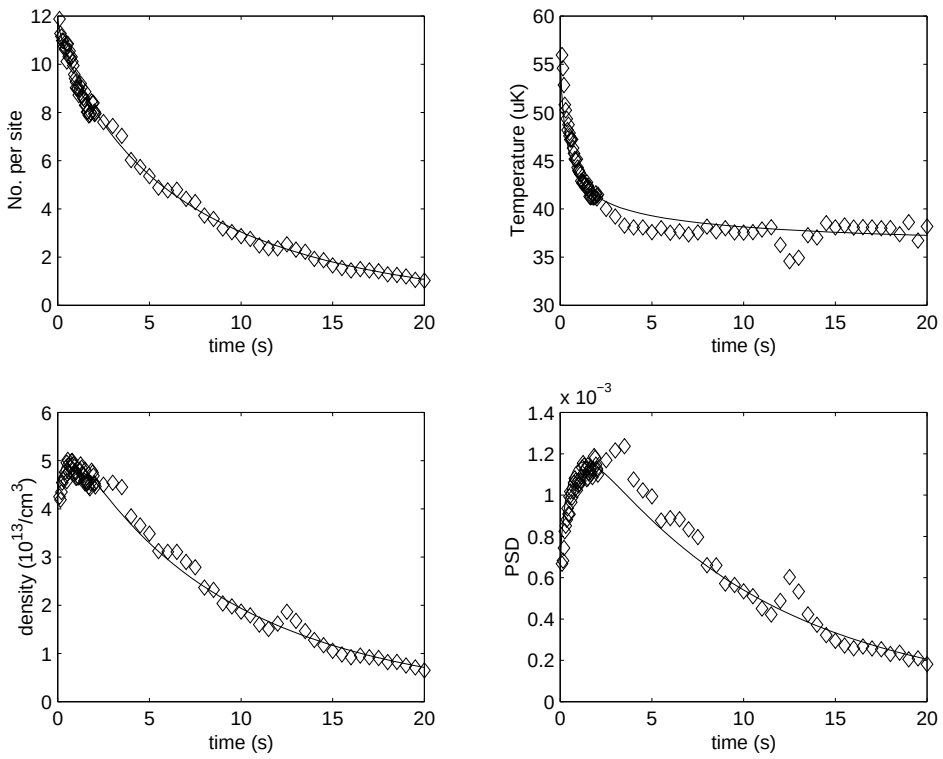

Figure 4.13: Plots showing the evolution of various quantities of interest with time. Data was taken under configuration A at 19W. The solid curves were obtained using the SHO model developed in an earlier chapter.

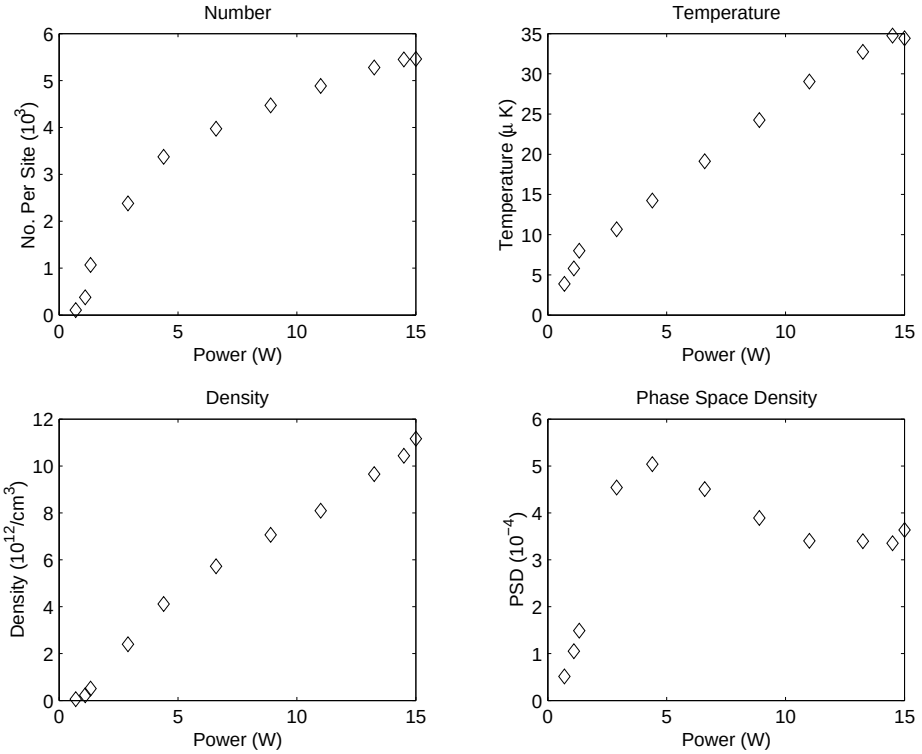

Figure 4.14: Plots showing the dependence of various properties on power. Data here is taken under configuration B.

the spatial distribution of the imaged fluorescence. This estimate is thus an average over the resolution of the imaging system which we estimate, for these data sets, to be $\sim 80\mu$m. Since this is much less than the Rayleigh range of the trapping beam we believe it to be a fair estimate of the number contained in the central trap. As in the single focus case we infer the frequencies at different powers by scaling the measurements made at a single fixed power. The results are shown in Fig 4.14 and Fig 4.15

The most notable feature is the saturation of the site occupation and the roll over of the phase space density. As in the single focus case we note the striking similarity in number and temperature measurements made between the two configurations. With regards to the temperature measurements it may well be argued that the waists of the beams relevant to the two different configurations were in fact equal (so that trap depths are equal at equal powers) and that the disparity in density and phase space density inferences is solely

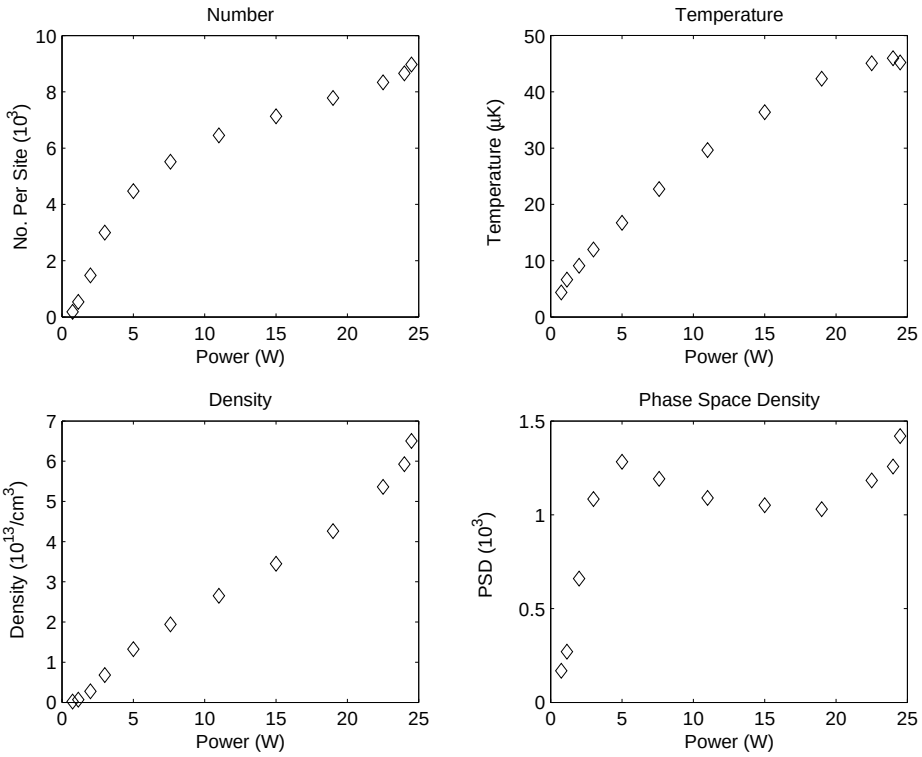

Figure 4.15: Plots showing the dependence of various properties on power. Data here is taken under configuration A.

due to systematic errors in the frequency measurements. However it would be strange that such a systematic error would show the degree of consistency seen in comparing the measured frequencies between the two trapping configurations as discuss at the beginning of the section. Ultimately the discrepancy is only a factor of two and as we are concerned more with trends and relative differences between geometries we do not concern ourselves further with this issue.

4.4 Discussion

At this point it is worthwhile to compare results from the single focus and 1-D lattice geometries considered above. In order to make a reasonable comparison some consideration as to what ultimately determines these quantities is needed. In [71] a simple model for the number of trapped atoms is derived assuming that the MOT comes into thermal and diffusive equilibrium with the CO_2 trap and predicts that the number of trapped atoms would rise exponentially with trap depth and that the peak density would scale as $n_0 = n_{MOT} \exp(U_0/k_bT)$ where n_{MOT} is the MOT density, U_0 is the trap depth and T is the MOT temperature. In our system the temperature of the MOT after the loading sequence is implemented has been measured at 20μK giving an estimated peak density in the lattice at high powers of $10^{17}/\text{cm}^3$ illustrating that a reasonable model needs to include the effect of density limitations imposed by the loading procedure. We are not interested in developing a sophisticated or even simple model to correctly predict the number of atoms we obtain in the trap. Our goal is to identify key elements dictating the main features in the data. Since the density and phase space densities are derived we may focus on the number and temperature.

The obvious limitation bottle-necking progress is the laser cooling process by which atoms are loaded into the trap. Since this process is understood to be density limited there are two immediate consequences to be expected. The first is the intuitively obvious fact that the number of atoms loaded will be limited by the volume of the trap itself and if the density limit is largely independent of depth the number of atoms could well be expected to scale with volume. The second consequence is in regards to the temperature

of the atoms. If the distribution of atoms obtained during loading is density limited then there will be an excessive amount of potential energy present when the cooling light is on. When the cooling light is extinguished the energy will redistribute to a Maxwell-Boltzmann form giving larger kinetic energies and therefore larger temperatures. One can therefore expect the temperature to rise with potential depth and this fact would be preserved by any subsequent evaporation.

The data does show a rising temperature with trap depth consistent with this simple argument, but it could well argued that this trend is consistent, to some degree, with evaporation which clearly plays a role over the 2 seconds delay before probing. However evaporation alone does not explain the highest temperatures which exceed that obtained using the same cooling scheme in free space. We note that in [77] larger temperatures seen in deeper traps was attributed to the induced stark shift interfering with the laser cooling process. Here the cooling lasers are detuned by $\sim 23\Gamma$ which is far greater than any stark shift induced by the trapping beams ($< 4\Gamma$) so it is hard to believe that this could be a plausible explanation. Since evaporation clearly plays a role in determining the temperatures measured we do not elaborate on this further but simply note that the rising temperature is qualitatively consistent with the simplistic picture given above.

In regards to the number of atoms it is worthwhile elaborating on the simple idea mentioned above. We begin by noting that, in the extreme limit in which the temperature of the MOT atoms is completely negligible and the trap is uniformly filled with a constant density, the number of trapped atoms would simply be proportional to the volume. For a gaussian trap the volume is of course infinite however gravity serves to truncate the trap at a finite volume. In Fig 4.16 we plot these volumes as a function of power where we have approximated gravity by truncating the trap as in Appendix B. The dashed line is that for the lattice trap, normalized by $\frac{1}{2}\mathrm{w}^2\lambda$ and the solid curve is that for the single focus trap normalized by $\pi \mathrm{w}^2 \mathrm{z_r}$. Well these curves show the same qualitative behavior seen in the data for the number of atoms there are two features that should be accounted for to maintain some degree of credibility. Firstly, the temperature of the MOT atoms (20μK) is not always small relative to the trap depth and secondly the MOT does not, in the case of the single focus trap, completely cover the longitudinal extent of the trap. To include these effects we

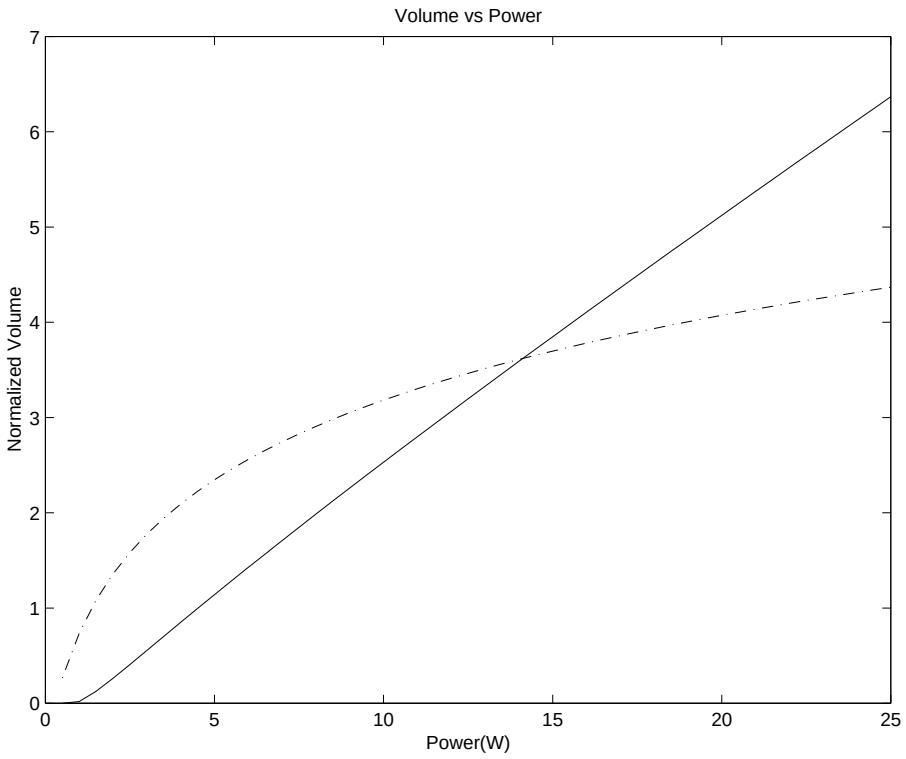

Figure 4.16: Plots illustrating the dependence of volume on power as discussed in the text.

thus consider a phase space distribution given by

$$\rho(\mathbf{r}) = \frac{1}{(2\pi m k_b T_R)^{3/2}} n_0 \exp(-\frac{z^2}{2\sigma^2}) \exp(-\frac{p^2}{2mk_bT_R}) \tag{4.8}$$

where n_0 is the fixed density, $T_R = 20\mu$K is the thermal energy obtained during loading, and $\sigma \sim 600\mu$m is the rms spread of the MOT. Typically a MOT is not, in general, well described by a gaussian profile but during the loading phase the MOT density profile does indeed take on such a form. We also note that we have neglected the variation transverse to the beam as the trap dimensions are much less than that of the MOT. To determine the number of trapped atoms we integrate over that part of phase space in which the energy is less than the potential depth taking the zero point energy to be the trap minimum. We find that the number of trapped atoms is given by

$$N_t = \iiint E < U_0 \rho \, d^3\mathrm{r} \, d^3\mathrm{p} \tag{4.9}$$

$$= n_0 \int_V P(3/2, \eta(\beta - u)) \, d^3\mathrm{r} \tag{4.10}$$

where V is the volume of the trap, $\eta = U_0/(k_bT)$, and β is the depth of the trap in the presence of gravity normalized by U_0. Gravity is included for the single focus trap since it is estimated to play a significant role for much of the data particularly at low power. However, it is typically negligible for the lattice traps and is therefore neglected with the integration region extended to infinity. In addition, the z dependence is dropped when considering the lattice trap as this dimension is much smaller than the MOT. In Fig 4.17 we plot this estimated number together with the measured values for all four traps considered. The density n_0 is chosen to given the best fit and for all four data sets is on the order of $10^{11}/\mathrm{cm}^3$ consistent with the MOT density. This fact can be viewed as somewhat fortuitous since evaporative and background losses have not been accounted for and it is known from absorptive images taken during loading that there is an enhancement of the (column) density within the trap. However, as mentioned above, we are not trying to predict the final number. To do so would require a complex analysis incorporating the exact nature of the trapping process, redistribution of the kinetic and potential energies after the cooling light is extinguished and subsequent evaporation. Here we are simply illustrating the intuitively obvious fact that larger traps trap more atoms and that the roll-off of number

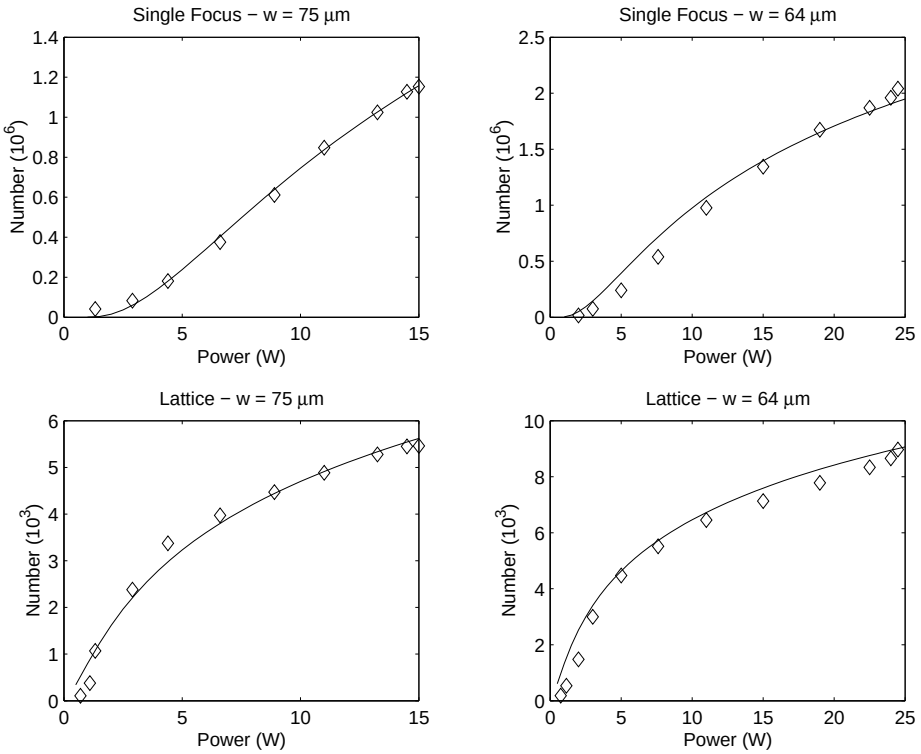

Figure 4.17: Plots illustrating the dependence of number on the volume of the trap for the lattice trap. Solid curves are calculated as described in the text.

for the lattice trap is consistent with a limitation imposed by the lattice geometry itself. In our system it is not practical to investigate the effects of spot size but for completeness we show the dependence on waist using the method above in Fig 4.18. Gravity has been included for both since it will clearly dominate for larger waists. Both plots use a power of 11W and a MOT temperature of 20μK and have been normalized arbitrarily to fit on the same graph. The optimum waist comes from a trade-off between trap size and depth and has been observed in [39]

Finally since evaporation processes clearly play a role in the results it is worth considering this and two quantities relevant to this process are the elastic collision rate k_{el} and $\eta = U_0/k_bT$. In Fig 4.19 we plot k_{el} vs. η for all four traps considered. Apart from a few outlying points which are associated with measurements made at the lowest powers the curve illustrates the universal fact that the higher the elastic collision rate the longer

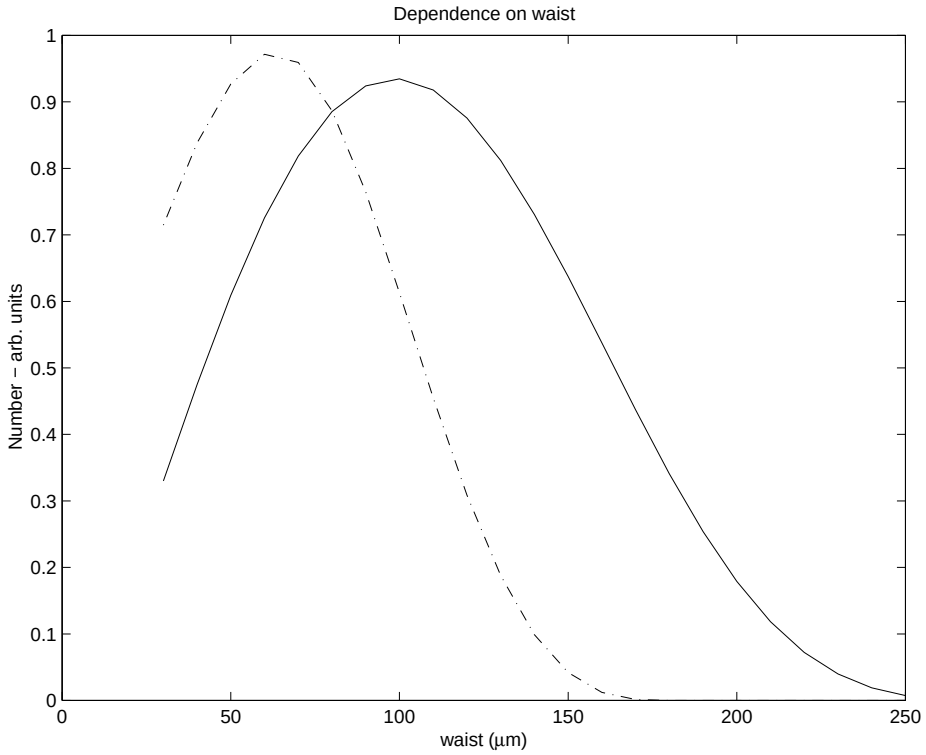

Figure 4.18: Plots illustrating the dependence on waist. Solid curve is for the lattice and dashed curve is for the single focus trap as described in the text.

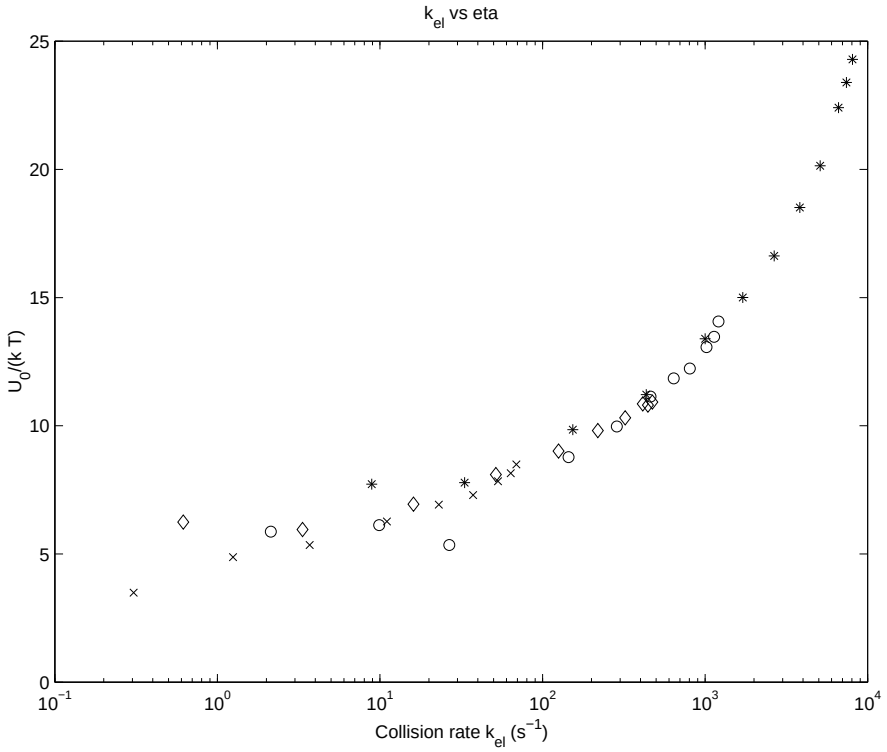

Figure 4.19: Plot illustrating the relation between the elastic collision rate and the ratio of trap depth to temperature. All four systems are included. Asterisks and circles correspond to the lattice and single focus data of configuration A. Diamonds and crosses correspond to the lattice and single focus data of configuration B

evaporation can be sustained giving rise to larger values of η.

Forced evaporation has been attempted in both of the trap configurations discussed here but with limited success. In the single focus case best attempts yielded only a factor of ~ 4 increase in phase space density and was most probably due to stagnation of the evaporation caused by the reduction in collision rate at low powers. In the lattice trap more than an order of magnitude increase could be obtained but small atom numbers prevented further progress. It should be noted that, in these attempts, data was extracted from fluorescent images and so better results could perhaps be achieved via absorptive imaging.

To summarize, in the current system forced evaporation needs to be fast due to the limited background lifetime of ~ 10 seconds. In the single focus trap a reasonably large number of atoms suitable for evaporation can be obtained but the relatively low starting

density means that the process becomes prohibitively slow with the background loss rate dominating at lower powers. Higher densities can be easily achieved in a 1-D lattice but this comes at the expense of a severe reduction in atom number. This is ultimately the crux of the problem: For high densities one wants tight confinement and for large atom number one desires a large volume and these requirements are typically in conflict. The solution is to choose a geometry in which the volume defining the number is different than the confinement volume defining the density. This is provided by a cross beam geometry as described in the next chapter.

Chapter 5

X-Trap : The QUEST for BEC

In the previous chapter we found that increasing the volume of the trap gave the intuitively obvious result that the number of trapped atoms increases, and that tight confinement gives rise to high densities and phase space densities. The single focus trap provides a large trapping volume but lacks the tight confinement in the longitudinal direction. The lattice trap, on the other hand, gives extremely good confinement but this is at the expense of the trapping volume. In an attempt to bring together the best of both worlds we have intersected two single focus traps in a cross beam geometry. In doing this we correct the weak confinement of the single beam trap while maintaining its large loading volume. Based on the investigations discussed in chapter 4 we could well expect to obtain 2 million atoms within this geometry. Furthermore by tightening the focus of the beams one can easily achieve a mean frequency exceeding 1kHz and a total depth of 600μK. From the trends seen in the single focus and lattice data we would thus expect a temperature of $< 50\mu$K. Hence one expects to achieve densities of $\sim 10^{14}\text{atomscm}^{-3}$ and phase space densities exceeding 10^{-3}. These are favorable numbers in view of the scaling laws discussed in chapter two and so the hunt for quantum degeneracy begins.

5.1 Basic Condensate Physics

We begin this chapter with a short discussion on Bose-condensation. Detailed discussions on this topic can be found elsewhere [20], [56], [51], and here we focus on those issues most important to our experiment, particularly regarding the observation of the condensate itself. We start with the standard treatment given in most texts on the ideal (non-interacting) condensate which is followed by a discussion on the effects of interactions. We then discuss

the evolution of the condensate in a time varying potential. Well this thesis does not cover excitations of the condensate arising from a time varying potential, the results can be applied to the simplest case of sudden switch off of the trap relevant to the time-of-flight analysis used exclusively in this work. Finally we remark on the case of a multi-component (spinor) condensate.

5.1.1 The Ideal Bose Gas

The Bose-Einstein Distribution

The thermodynamics of a Bose gas is most easily derived from the grand canonical partition function [44]

$$\mathcal{Z} = \prod_i \left(1 - z\exp(-\beta\epsilon_i)\right)^{-1} \tag{5.1}$$

where $\beta = 1/k_bT$ and z is the fugacity of system, related to the chemical potential, μ, via $z = \exp(\beta\mu)$. Within this framework, the number of particles is determined by

$$N = z\frac{\partial}{\partial z}\ln(\mathcal{Z}) = \sum_i \frac{ze^{-\beta\epsilon_i}}{1 - ze^{-\beta\epsilon_i}} \tag{5.2}$$

which is nothing more than the statement that $N = \sum_i \langle n_i \rangle$ where n_i is the occupation number for the i^{th} state. In order to evaluate this sum we can make the semiclassical approximation whereby the summations are replaced by integrals under the assumption that the thermal energy k_bT is much larger than the energy level spacing $\hbar\omega$. In this approximation we have

$$N = \frac{z}{1-z} + \int_0^\infty \rho(\epsilon)\frac{1}{z^{-1}\exp(\beta\epsilon) - 1} \tag{5.3}$$

where $\rho(\epsilon)$ is the energy density of states. The first term gives the ground state occupation and is separated out since it is given zero weight in the integral term. Thus the integral term gives the number of particles occupying the excited states. For a trapping potential U the density of states is given by

$$\rho(\epsilon) = \frac{2\pi(2m)^{3/2}}{(2\pi\hbar)^3}\int \sqrt{\epsilon - U(\mathbf{r})}\, d^3r, \tag{5.4}$$

where the integration is restricted to the region over which $U(\mathbf{r}) < \epsilon$, so that the excited state fraction may be written as

$$\begin{aligned} N_e &= \frac{2\pi(2m)^{3/2}}{(2\pi\hbar)^3} \int d^3r \int_{U(\mathbf{r})}^{\infty} \sqrt{\epsilon - U(\mathbf{r})} \frac{1}{z^{-1}e^{\beta\epsilon} - 1} \\ &= \frac{2\pi(2m)^{3/2}}{(2\pi\hbar)^3} \int d^3r (k_bT)^{3/2} \sum_{j=1}^{\infty} \exp(j(\mu - U(\mathbf{r}))/k_bT) \int_0^{\infty} d\epsilon \sqrt{\epsilon} e^{-\epsilon j} \\ &= \left(\frac{mk_bT}{2\pi\hbar^2}\right)^{3/2} \int d^3r \sum_{j=1}^{\infty} \frac{\exp(j(\mu - U(\mathbf{r}))/k_bT)}{j^{3/2}} \\ &= \int n(\mathbf{r})\, d^3r \end{aligned} \tag{5.5}$$

Here we have identified the particle density $n(\mathbf{r}) = g_{3/2}\left[ze^{-U/k_bT}\right]/\Lambda^3$ where Λ is the thermal deBroglie wavelength, and generally $g_i(x) \equiv \sum_{j=1}^{\infty} x^j/j^i$. It should be noted that, in the classical limit in which $z << 1$, we have $g_{3/2}(z) \sim z$ so that the density reduces to that described by the classical Maxwell-Boltzmann distribution as expected.

Bose Condensation and the Critical Temperature

At this point it is worth considering a specific example and we choose that of a simple harmonic oscillator as it is relevant to all traps considered in this thesis, at least in the low temperature (or equivalently deep trap) limit. In this case the integration for the excited state occupation can be computed analytically to give

$$N_e = g_3(z) \left(\frac{k_bT}{\hbar\bar{\omega}}\right)^3 \tag{5.6}$$

where $\bar{\omega}$ is the geometrically averaged frequency. Since the occupation numbers $\langle n_i \rangle$ must remain positive, it can be easily seen that $0 \leq z \leq 1$. Furthermore, the function $g_3(z)$ is monotonic and bounded on this interval so that we must have

$$N_e \leq g_3(1) \left(\frac{k_bT}{\hbar\bar{\omega}}\right)^3 \simeq 2.612 \left(\frac{k_bT}{\hbar\bar{\omega}}\right)^3. \tag{5.7}$$

Now, so long as the actual number of particles in the system is less than this limiting value, practically all the particles of the system are distributed among the excited states and the precise value of z can be determined from equation (5.6) with the approximation that $N_e \simeq N$. When the number of particles exceeds this value the result is a dramatic

accumulation of particles in the ground state and this phenomenon is generally referred to as Bose-condensation. For a given number of particles, this onset occurs at a temperature, T_c^0, given by

$$k_b T_c^0 = \hbar\bar{\omega}\left(\frac{N}{g_3(1)}\right)^{1/3}. \tag{5.8}$$

As the system cools below this critical temperature the number of particles in the ground state grows according to

$$\frac{N_0}{N} = 1 - \left(\frac{T}{T_c^0}\right)^3 \tag{5.9}$$

These equations of course depend on the exact geometry of the trapping potential. Results for a variety of potentials can be found in [7].

Strictly speaking our discussion only applies in the thermodynamic (large N) limit. A discussion of finite size effects can be found in [20] and references therein. Basically the effect is to reduce the critical temperature from that given above and is typically negligible for $N > 10^4$.

5.1.2 The Interacting Bose Gas

In the absence of atom-atom interactions the condensate is described by the single particle ground state wave function. Thus the density profile is that of a gaussian having an rms size of $a_{ho} = \sqrt{\hbar/m\omega_{ho}}$ independent of particle number. When interaction effects are included the condensate swells due to self-repulsion and becomes much larger than that predicted from the simple non-interacting picture. Starting from a general many body Hamiltonian description one may apply a mean field approach which leads to the Gross-Pitaevskii equation typically used to describe the trapped condensate.

Mean Field Theory

The many body Hamiltonian describing N interacting bosons confined by an external potential U is given, in second quantization, by [20]

$$\hat{H} = \int d^3r \Psi^\dagger(\mathbf{r})\left[-\frac{\hbar^2}{2m}\nabla^2 + U(\mathbf{r}\right]\Psi(\mathbf{r}) + \frac{1}{2}\int d^3r\, d^3\prime r \Psi^\dagger(\mathbf{r})\Psi^\dagger(\prime\mathbf{r})V(\mathbf{r}-\prime\mathbf{r})\Psi(\prime\mathbf{r})\Psi(\mathbf{r}) \tag{5.10}$$

where $\Psi(\mathbf{r})$ and $\Psi^\dagger(\mathbf{r})$ are the boson field operators that annihilate and create a particle at position $\mathbf{r}$ and V is the two-body interaction potential. The dynamics of the system can then be found by numerical integration of the Heisenberg equation. This approach is somewhat cumbersome and two simplifications are made.

The first simplification involves the interaction potential V. At low energies binary collisions are completely characterized by the s-wave scattering length a_s, independent of the potential V, and for dilute gases these are the only collisions that one needs to consider. Under these conditions one can then replace the potential V with a more convenient form having the same scattering properties, namely $V = g\delta(\mathbf{r} - \prime\mathbf{r})$ where g is related to the scattering length via $g = 4\pi\hbar^2 a_s/m$.

The second simplification is the use of a mean field approach whereby the condensate contribution to the boson field operator is separated out so that we may write $\Psi(\mathbf{r}) = \Phi(\mathbf{r}) + \Psi\prime(\mathbf{r})$ where $\Phi(\mathbf{r}) \equiv \langle\Psi(\mathbf{r})\rangle$. Its modulus fixes the density of the condensate through $n_0(\mathbf{r}) = |\Phi(\mathbf{r})|^2$ and is often referred to as the condensate wave function. When $\Psi\prime(\mathbf{r})$ is small it may be treated as a perturbation, and one obtains, to zeroth order, the equation

$$i\hbar\frac{\partial\Phi}{\partial t} = \left(-\frac{\hbar^2}{2m}\nabla^2 + U + g|\Phi|^2\right)\Phi \tag{5.11}$$

known as the Gross-Pitaevskii (GP) equation. Its validity is based on the condition that the s-wave scattering length be much smaller than the average distance between atoms and that the number of atoms in the condensate is much larger than 1. The latter of these conditions is trivial and the former can be written as $\bar{n}a_s^3 \ll 1$ where $\bar{n}$ is the average density of the gas. In our experiment we have $\bar{n} \sim 10^{14} atoms/cm^3$ and $a_s = 5.77nm$ [12] so that $\bar{n}a_s^3 \sim 10^{-5}$. Thus our use of the GP equation is well justified.

When the condition $\bar{n}a_s^3 \ll 1$ is satisfied the system is said to be weakly interacting or dilute, however this does not mean the effects of the interaction are small. To assess the importance of the interaction one has to compare the relevant energy scales. For densities $n \sim 10^{14}\text{cm}^{-3}$ we have $gn \sim k_b \times 40\text{nK} \sim 2\pi\hbar \times 1\text{kHz}$. Above the critical temperature the relevant energy scale is, of course, just the thermal energy k_bT and so interaction effects can be neglected. On the other hand the relevant energy scale for the condensate is the level spacing $\hbar\omega \sim \hbar \times 2\pi\,100\,\text{Hz}$ and so the behaviour of the condensate is dominated by the interactions.

The Ground State

To obtain the ground state within the mean field theory, one may write the condensate wave function as $\Phi(\mathbf{r},t) = \phi(\mathbf{r})\exp(-i\mu t/\hbar)$ where μ is the chemical potential and ϕ is real and normalized such that $\int d^3r\phi^2 = N_0 = N$. The GP equation then takes the form

$$\left(-\frac{\hbar^2}{2m}\nabla^2 + U + g\phi^2(\mathbf{r}) - \mu\right)\phi(\mathbf{r}) = 0. \tag{5.12}$$

In the absence of interactions this equation reduces to the familiar Schrödinger equation as one might expect. When interactions are included the equation can be numerically integrated, but this is typically unnecessary. In most, if not all, experiments to date the first term in the equation, which represents the kinetic energy, can be neglected in comparison to the mean field energy. In this case the solution is trivially obtained and one has

$$n(\mathbf{r}) = \phi^2(\mathbf{r}) = \frac{\mu - U}{g} \tag{5.13}$$

in the region where $\mu - U \geq 0$ and is zero otherwise. This approximation is often referred to as the Thomas-Fermi (TF) model. The chemical potential μ is then determined from the normalization condition and one finds, for the harmonic oscillator, the expression

$$\mu = \frac{\hbar\bar{\omega}}{2}\left(\frac{15Na}{a_{ho}}\right)^{2/5} \tag{5.14}$$

where $a_{ho} = \sqrt{\frac{\hbar}{m\bar{\omega}}}$ is the rms size of the single particle ground state. To determine the range of validity of the TF model one can simply rescale equation (5.12) in the usual way to obtain the non-dimensional form

$$\left[-\left(\frac{a_{ho}}{8\pi aN}\right)^{4/5}\tilde{\nabla}^2 + \tilde{r}^2 + \tilde{\phi}^2 - \tilde{\mu}\right]\tilde{\phi} = 0 \tag{5.15}$$

where the tilde is used to indicate rescaled quantities and, for simplicity, we have restricted our attention to a spherically symmetric harmonic oscillator. Thus we see immediately that the kinetic energy term may be neglected whenever $8\pi aN/a_{ho} \gg 1$. More generally, for the non-symmetric case, this condition should be satisfied in each direction.

It is also worth noting that the solution of the GP equation (5.12) minimizes the energy functional given by

$$E(n) = \int d^3r\left[\frac{\hbar^2}{2m}|\nabla\sqrt{n}|^2 + nU(\mathbf{r}) + \frac{gn^2}{2}\right] \tag{5.16}$$

and each of the three terms correspond to the kinetic, potential and mean field energies respectively.

Expansion of the Condensate

The time-dependent GP equation (5.11) may be used to determine the behaviour of a condensate in a time varying potential [16]. Details of this can be found in [20] and references therein. Here we simply note that, in the limit $8\pi aN/a_{ho} \gg 1$, the GP equation permits a class of solutions in which the parabolic shape of the Thomas Fermi model is preserved and the radii, R_i, where the density vanishes, scale in time as

$$R_i(t) = R_i(0)b_i(t) = \sqrt{\frac{2\mu}{m\omega_{0i}^2}}b_i(t). \tag{5.17}$$

Here ω_{0i} determines the frequencies at time $t = 0$ and i is used to denote the coordinate axes. Furthermore it can be shown that the functions $b_i(t)$ satisfy the ordinary differential equations

$$\ddot{b}_i + \omega_i^2 b_i - \frac{\omega_{0i}^2}{b_i b_1 b_2 b_3} = 0. \tag{5.18}$$

These equations can be used to simulate the expansion of the gas during time of flight by dropping the second term associated with the confining potential and using the initial conditions $b_i(0) = 1$ and $\dot{b}_i(0) = 0$. In this way one can determine the time evolution of the aspect ratios and cloud size which is easily observed in the experiment.

It worth commenting on the difference between the expansion of a condensate and the expansion of a thermal cloud as the time of flight distribution is a key signature for the onset of condensation. In the case of a thermal cloud the momentum distribution is isotropic, according to the equipartition principle and so the gas expands isotropically. The result is that any thermal cloud will eventually take the form of an isotropic gaussian for expansion times greater than the oscillation periods of the system. For a condensate however the situation is much different which can be easily understood from consideration of a non-interacting gas in an asymmetric harmonic trap. In this case the momentum distribution is no longer isotropic and reflects the asymmetry of the trap so that the cloud expands faster in the most tightly confining direction. The result is that the ballistic expansion of a condensate has an aspect ratio reflecting the geometry of the trap.

5.1.3 Spinor Condensates

So far our discussion has been restricted to a one component gas. However in our experiment this is not the case. Well the atoms are initially pumped into the $F = 1$ manifold, no effort is made to restrict them to a particular m state and so we expect a mixture of all three spin projections. The order parameter, or wave function, representing this multi-component gas is a vector in hyperfine spin space and is thus called a spinor condensate. In this thesis we have not explicitly probed the spinor nature of the condensate, and a detailed discussion on this topic is not needed. A treatment in the spirit of that given for the one component gas gas above can be found in [41] and a detailed discussion of spinor condensates in both theory and experiment is given in [49].

The essential features of these treatments is in the fact that, due to rotational symmetry, the interaction potential for an $F = 1$ spinor is described by two parameters not one as in the the scalar case and we denote these as g_0 and g_2. As in the scalar case these are related to scattering lengths via $g_F = 4\pi\hbar^2 a_F/m$ where a_F is the scattering length in the total spin F channel. The order parameter is written as $\psi = \sqrt{n(\mathbf{r})}\vec{\zeta}$, where $n(\mathbf{r})$ is the density and $\vec{\zeta}$ is a normalized spinor. The ground state structure is found by minimizing the functional

$$K = \int d^3r \left(\frac{\hbar^2}{2m}(\nabla\sqrt{n})^2 + \frac{\hbar^2}{2m}(\nabla\zeta)^2 n - (\mu - U)n + \frac{n^2}{2}(c_0 + c_2 \langle \mathbf{F} \rangle^2) \right), \tag{5.19}$$

where $c_0 = (g_0 + 2g_2)/3$ and $c_2 = (g_2 - g_0)/3$ [41]. The final term gives rise to two distinct forms which depend on the relative sizes of the scattering lengths a_F. For $a_2 > a_0$ the energy is minimized by $\langle \mathbf{F} \rangle = 0$ and the spinor is said to be anti-ferromagnetic or polar. For $a_2 < a_0$ the energy is minimized by $| \langle \mathbf{F} \rangle | = 1$ and the spinor is said to be ferromagnetic which is the situation for ^{87}Rb. In either case the density profile is well approximated by the Thomas-Fermi profile provided the interaction energy dominates as in the scalar case.

5.2 Trapping Frequencies and trap lifetime

We begin our discussion of the cross trap with measurements of the trap frequencies and the trap lifetime. Since the nature of the trap depends on the alignment and intersection of

two beams the trap spectrum can exhibit some unexpected features which was particularly pointed in the initial set up where no attempt was made to ensure the two single focus traps had identical trapping frequencies or equivalently spot sizes. In this section we illustrate a couple of frequency spectrums taken throughout the course of this work. This is followed by a discussion of the trap lifetime which is found to be dominated by three-body losses.

5.2.1 Frequency Spectrum

The potential for the cross beam trap is simply given by the sum of the individual potentials for the single beam constituents. Any interference is removed by shifting the frequency of one beam relative to the other. Assuming each beam is identical it is easy to show that the frequencies at the bottom of the well are given by

$$\omega_s = \sqrt{\frac{4U_0}{mw_0^2}} \quad \text{and} \quad \omega = \sqrt{2}\omega_s \tag{5.20}$$

where U_0 is the depth of the single beam trap. Thus the two lowest frequencies are just the frequencies of the individual traps. This is easy to understand since the longitudinal confinement of one beam is completely negligible relative to the confinement provided by the other. Both beams provide equal confinement in the direction orthogonal to both and thus the frequency in this direction is enhanced. This is of course in theory and in practice the situation is somewhat more complicated with the trap spectrum being different from setup to setup.

In the set up that led to the first observation of a BEC the frequency spectrum at the lowest powers showed a rather extreme splitting. A spectrum taken at 450mW is shown in Fig 5.1 and there are two immediate concerns. The first is the large difference in frequencies not seen at high power. The second problem is in the fact that each frequency is pretty much separated by a factor of two and so one needs to determine if a given frequency is an ω or 2ω frequency. The first problem is not well understood and it is suspected that the effects of beam aberrations and differences in beam sizes become more pronounced at low powers. Eigenvalue analysis for reasonable beam aberrations does not confirm this[1] although the anharmonic, indeed bimodal, nature of the trap geometry brings

[1]Gravity clearly reduces one of the frequencies to zero at a low but finite power but this fall off is very sharp and it would be hard to believe that such a trap could be stable

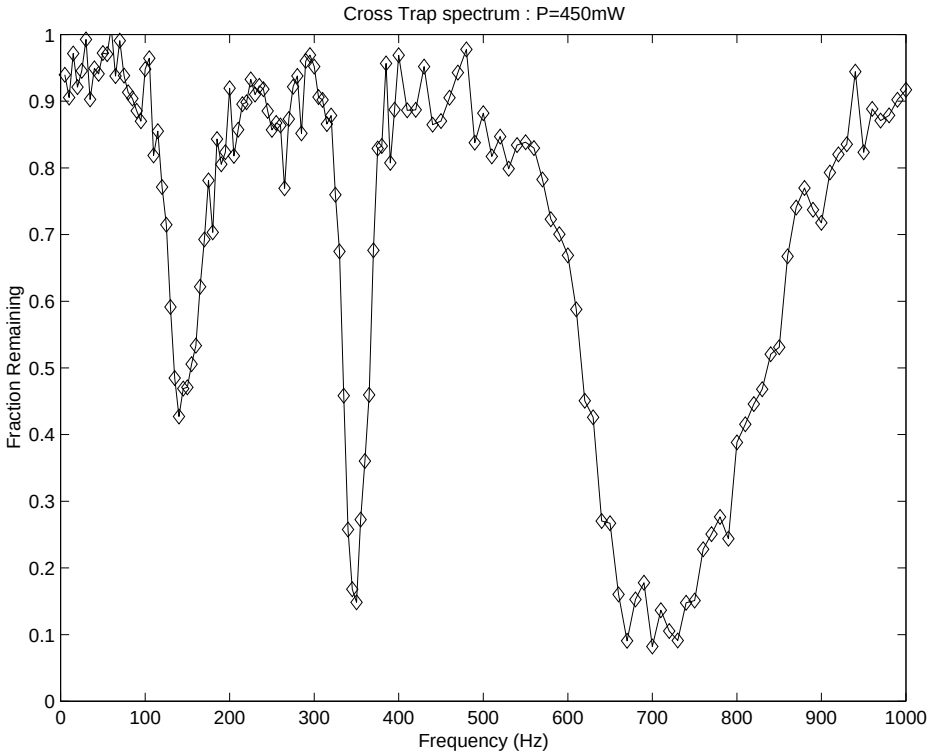

Figure 5.1: A frequency spectrum of the cross trap taken with P=450mW.

into question the validity of such a treatment [46]. A more detailed investigation on the frequency spectrum was discussed earlier and here we note that, well the problem is not well understood, the spectrum was very reproducible and that the highest frequency is consistent with those measured at high power. For this reason we have faith in the fact the spectrum provides reasonable estimates of the true frequencies.

The second problem can be overcome simply by varying the power in each beam and noting the frequency shifts. If the power in both beams is changed the ratios shift slightly indicating they are truly three separate frequencies of the system. In addition, if the power in one beam is shifted with the other unchanged then the relative change in each frequency is different. This can be easily understood by considering how each frequency is influenced by the power in each beam. With reference to Fig 5.2 confinement in the x direction is due solely to the beam propagating in the y direction and vice-versa. Confinement in the z direction is provided by both beams. Thus by changing the power in one beam only one frequency should remain unchanged while the others shift by differing relative amounts consistent with our observations. This splitting was latter investigated by measuring the frequencies at a range of powers in order to observe how the additional frequencies arose. While the spectrum was not equivalent to that relevant to the work in [**?**], it exhibited the same splitting at the lowest powers. The reason for the difference is that the laser initially exhibited two stable modes of operation. At the time these spectrums were taken one of these modes had become unstable and this was the mode relevant to the work cited in [**?**]. In Fig 5.3, 5.4, and 5.5 we show the measured spectrums ranging over powers extending from 0.5W to 9W and apparent in Fig 5.5 is the sharp appearance of a third frequency at P=0.6W. Also note that at the highest power there appears to be only one frequency or though there is some evidence of an additional unresolved frequency which becomes more apparent as the power is lowered. We also note that the second frequency seems largely suppressed despite the fact that the smaller frequency is expected to exhibit a larger resonance based on numerical simulations of parametric excitation within such a geometry. These features are not well understood although it is suspected that beam alignment and abberation play an important role in determining the nature of the spectrum. Nevertheless in Fig 5.6 we show the measured frequencies as a function of power. In this figure we

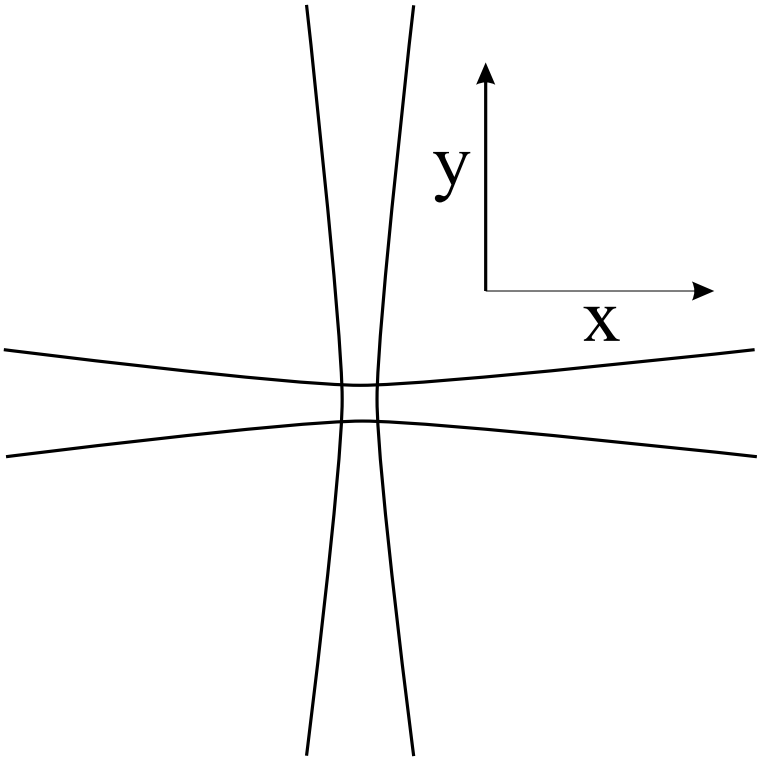

Figure 5.2: Schematic of the cross beam geometry.

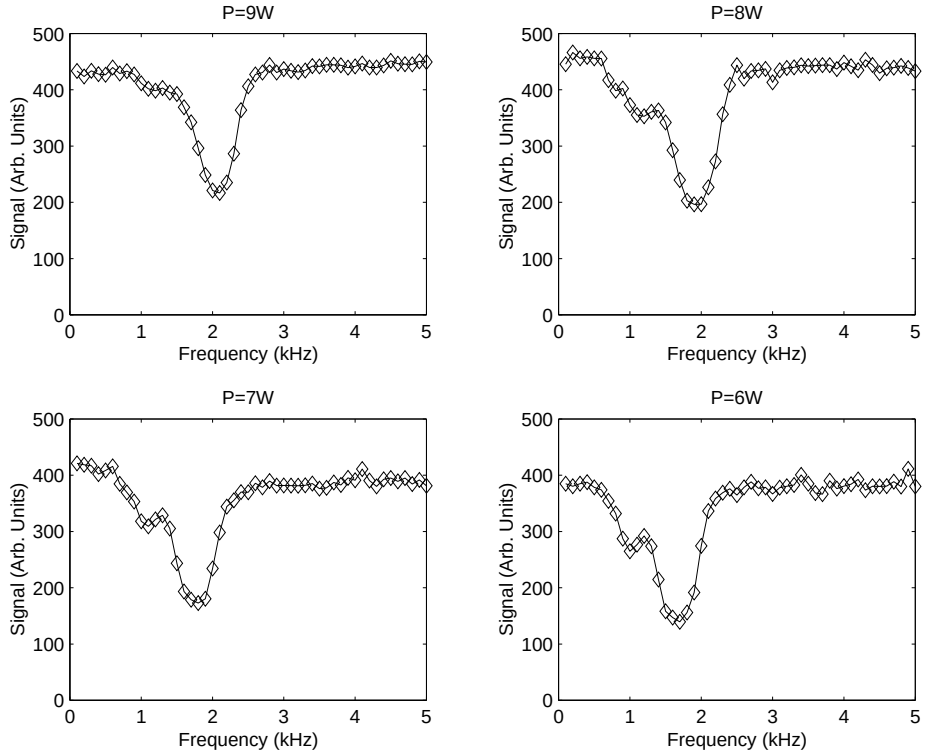

Figure 5.3: Frequency spectrums of the cross trap found via parametric resonance

have omitted the measured frequency at 9W and the additional frequencies at low power. In addition we have plotted the geometrically averaged frequency assuming the smallest frequency is degenerate. The solid curve is the best fit assuming that $\nu \sim \sqrt{P}$. Error bars have been omitted to avoid cluttering figure and the typical uncertainty is about 10%.

Later, on the assumption that beam alignment and differences in beam waists played a role in determining the features of the spectrum, the beam focusses were adjusted so that the measured frequencies of the individual traps, and thus spot sizes, were as equal as practically possible. This resulted in a much more satisfactory spectrum. A typical example at high power is shown in Fig 5.7 which shows the larger resonance at the lowest frequency as expected, and the complete spectrum is shown in Fig 5.8. Under these circumstances no splitting was observed even at low powers lending support to the explanation given earlier for the features of the spectrum. The geometrically averaged frequencies are given Fig 5.9 and the solid curve is the best fit assuming $\nu \sim \sqrt{P}$ as above.

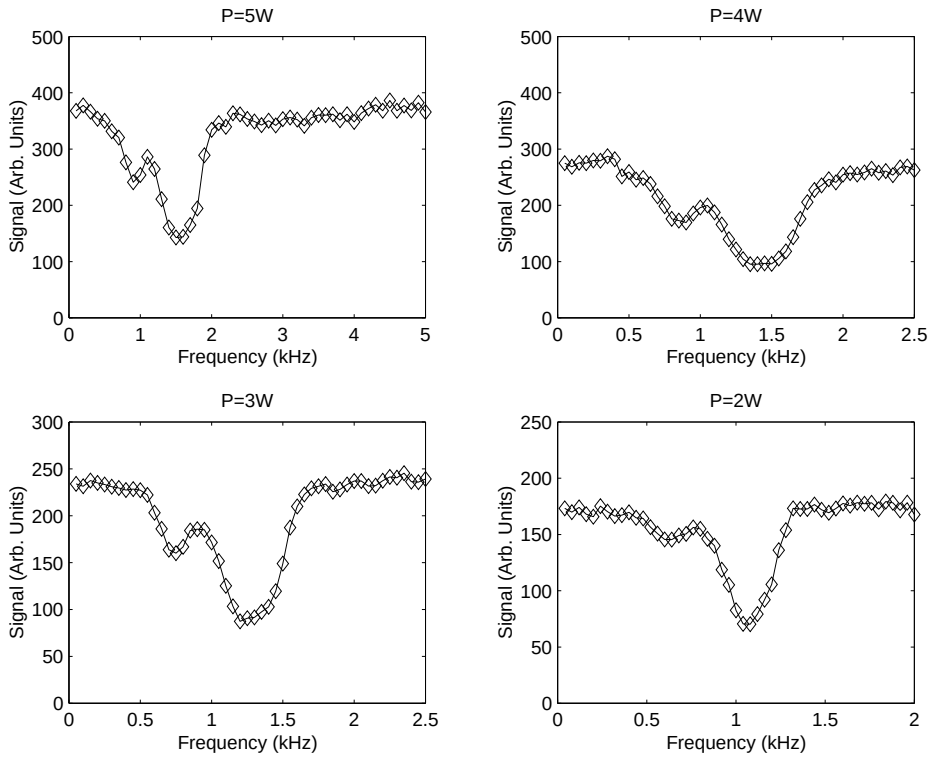

Figure 5.4: Frequency spectrums of the cross trap found via parametric resonance

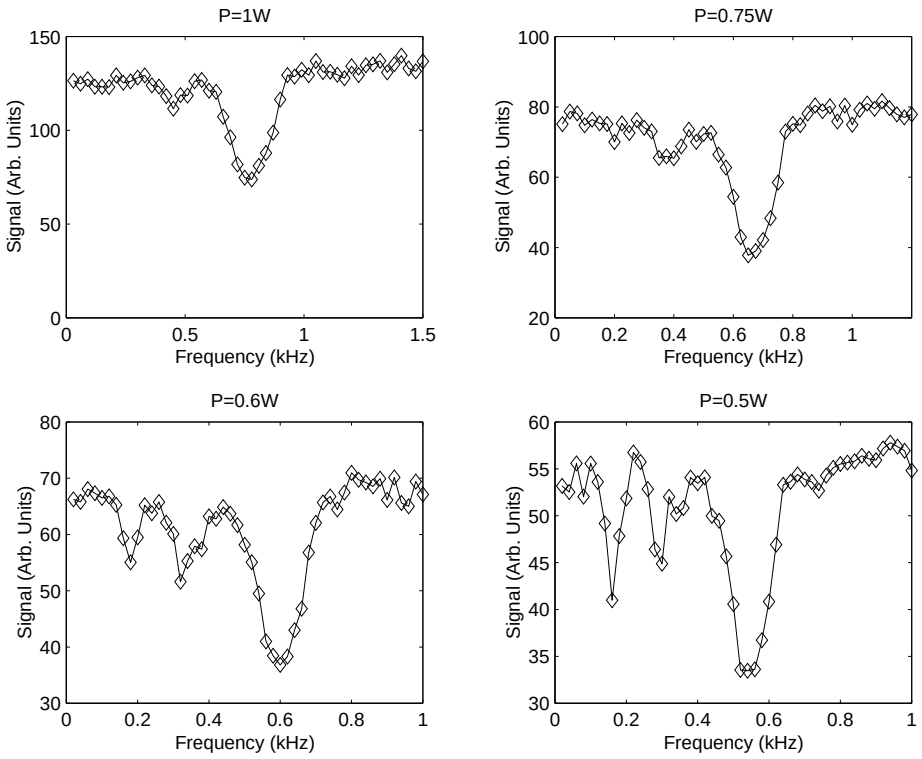

Figure 5.5: Frequency spectrums of the cross trap found via parametric resonance

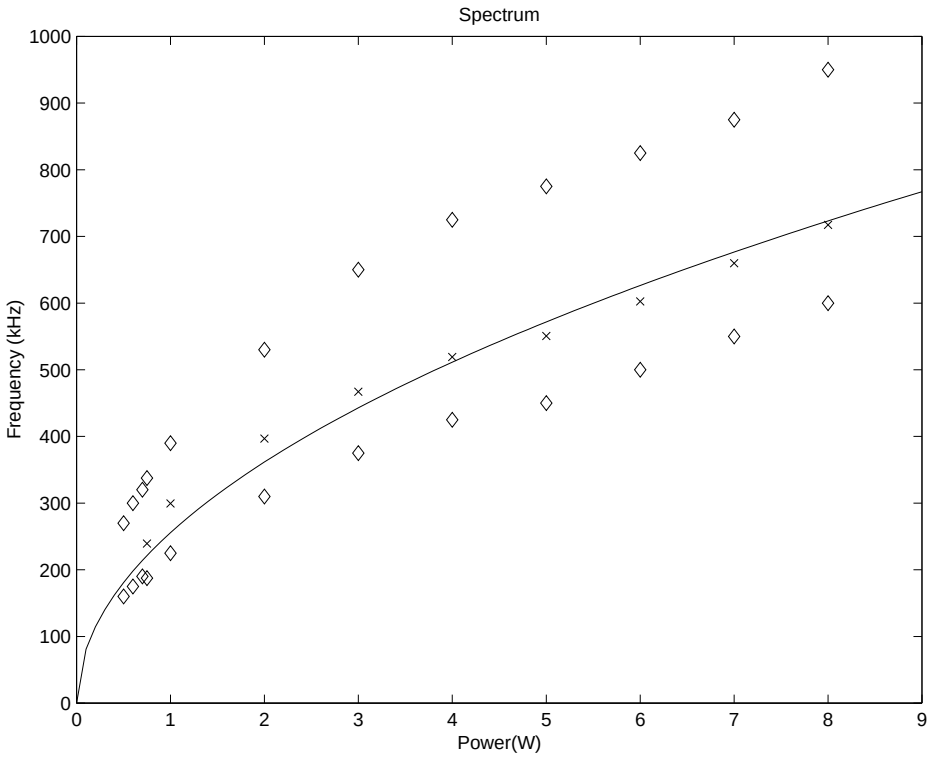

Figure 5.6: Measured frequencies as a function of power. Diamonds are the measured values and crosses are the geometric average assuming degeneracy of the lowest frequency. Solid curve is best fit assuming $\nu \sim \sqrt{P}$

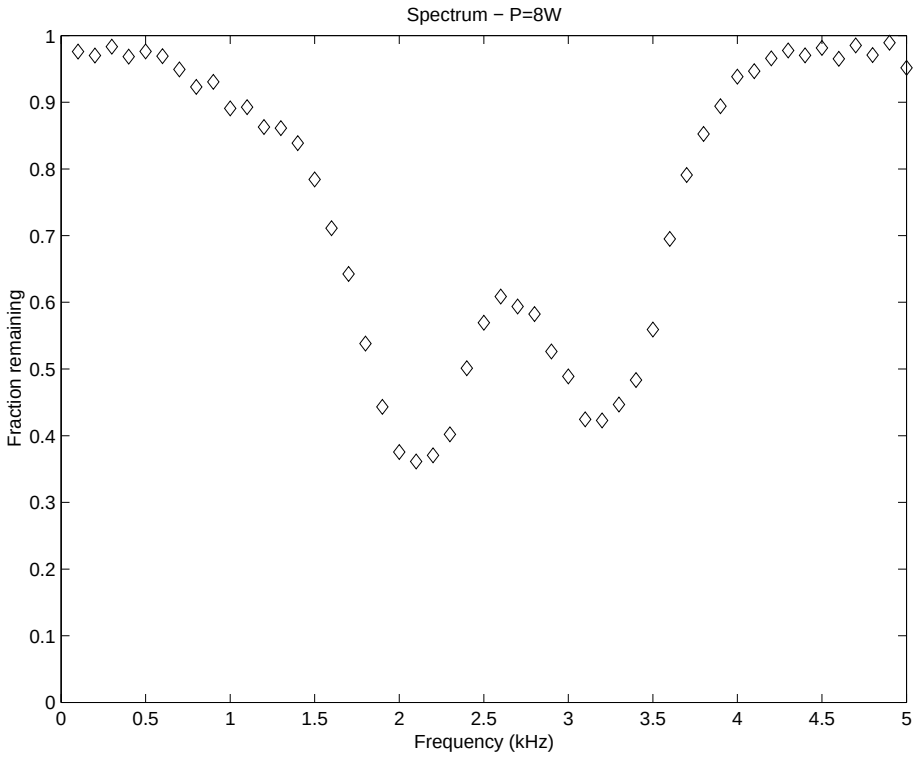

Figure 5.7: Frequency spectrum of the cross trap at high power found via parametric resonance after beams were adjusted to give similar spot sizes

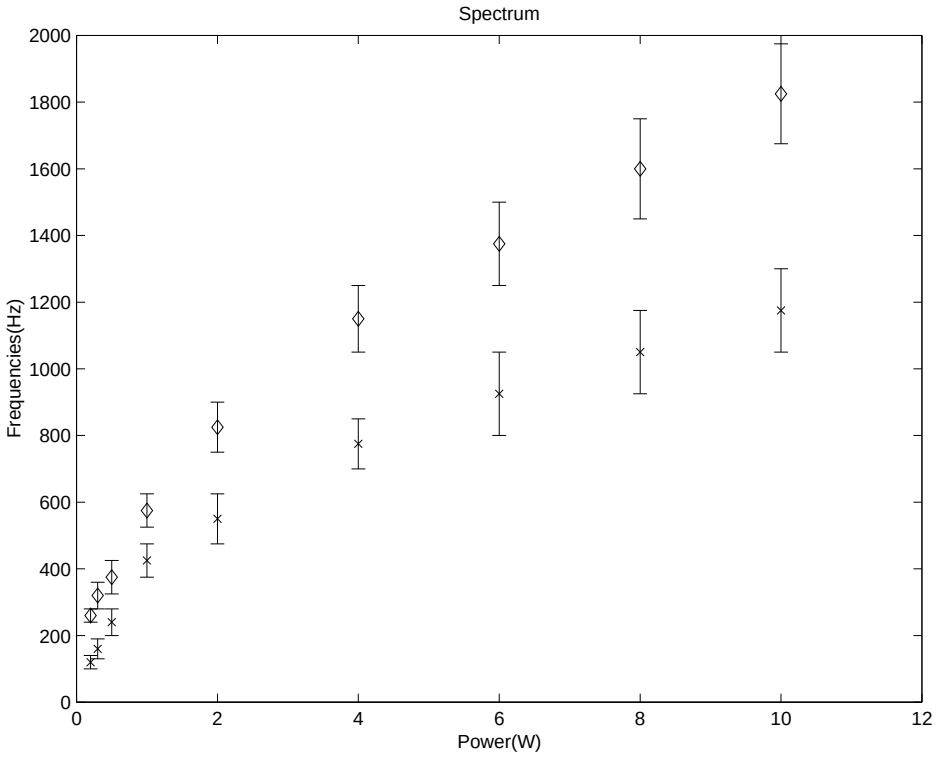

Figure 5.8: Frequencies of the cross trap as a function of power found via parametric resonance after focus adjustment

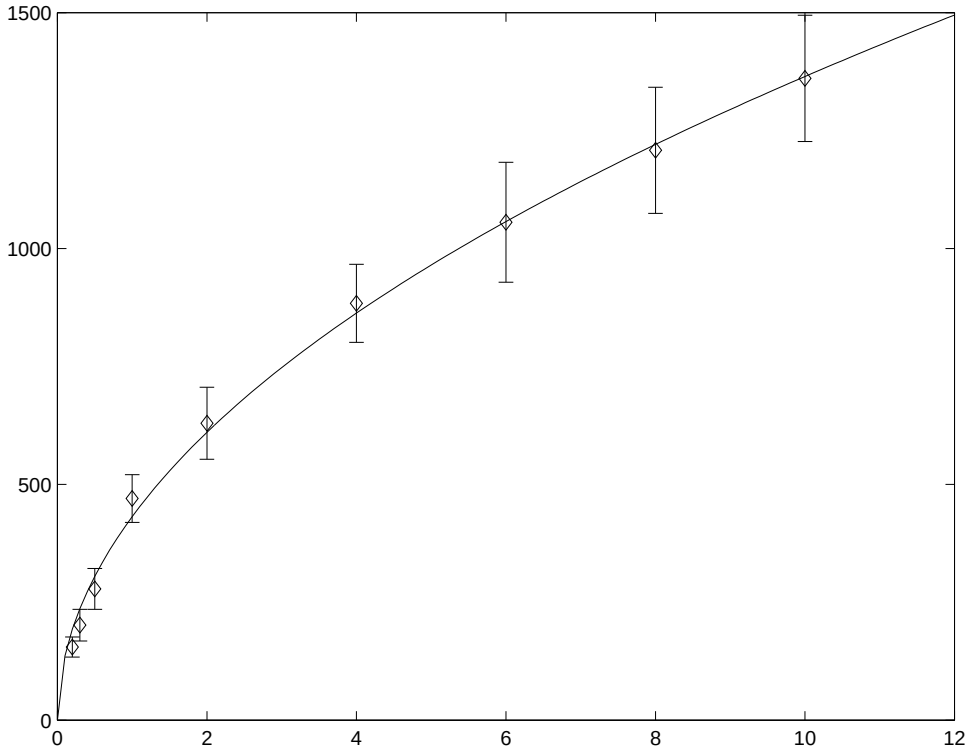

Figure 5.9: Geometrically averaged frequency as a function of power. Solid curve is best fit assuming $\nu \sim \sqrt{P}$

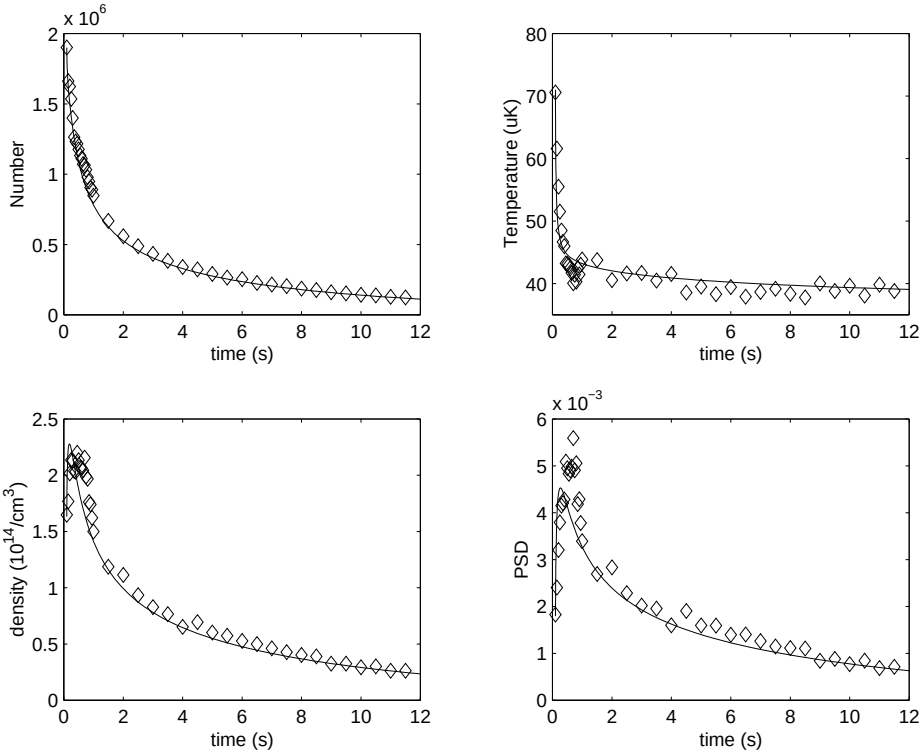

Figure 5.10: Lifetime data for the cross beam trap

5.2.2 Lifetime and three body losses

A typical lifetime curve from the cross beam trap is shown in Fig 5.10 and for clarity we have shown the first 3s of these curves in Fig 5.11 to emphasized the initial dynamics. Taking the final 6 data points on this curve gives a background loss rate of $10(1)Hz$ consistent with the previous traps. This has been validated by monitoring the atom loss for times out to 20 seconds where three-body recombination and evaporation is negligible. The solid curves shown in the figures are given by the model discussed in chapter 2 with the trap depth set to 650μK. This depth is consistent with estimates made based on the measured mean frequency of $\sim$ 1.5kHz but, as one beam is on the diagonal, gravity is expected to reduce this somewhat. Nevertheless in view of the simplicity of the model the results are quite satisfactory.

Given that the initial density exceeds 10^{14}cm^{-3} and that the model indicates that

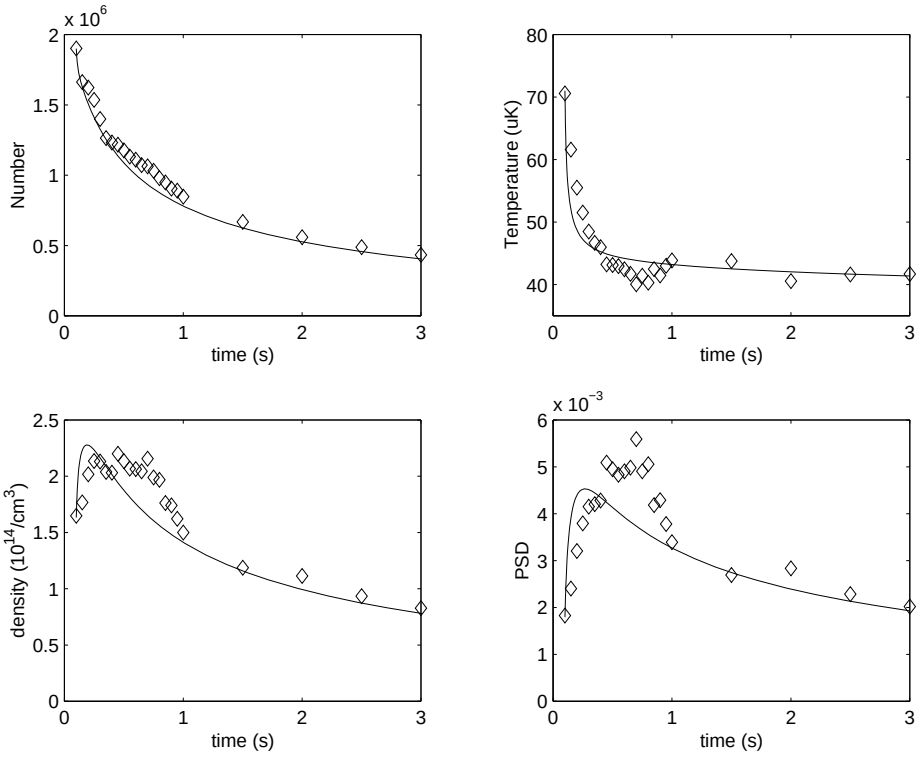

Figure 5.11: Lifetime data showing the first 3 seconds

three body losses dominate the lifetime curve, one should be able to extract a three body loss rate from this data. Well this is complicated by the obvious presence of evaporation we note that the evaporation is clearly negligible after approximately 0.75secs so we proceed using only the data taken at $t \geq 0.75$. Our approach follows that in [14] and we outline this procedure.

In the absence of evaporation processes the rate equation is given by

$$\dot{N} = -\Gamma_b N - L_3 \int_V n^3(\mathbf{x}, t)\, d^3r \tag{5.21}$$

or equivalently by the integral equation

$$\ln \frac{N(t)}{N(0)} + \Gamma_b t = -L_3 \int_0^t \left\langle n^2(\mathbf{x}, t') \right\rangle \, dt' \tag{5.22}$$

where we have defined

$$\left\langle n^2(\mathbf{x}, t') \right\rangle = \frac{1}{N(t')} \int_v n^3(\mathbf{x}, t')\, d^3r. \tag{5.23}$$

Using the harmonic oscillator expression the spatial integral can be computed straightforwardly and the resulting equation can then be written

$$\ln \frac{N(t)}{N(0)} + \Gamma_b t = -\frac{L_3}{3\sqrt{3}} \int_0^t n_0^2 \, dt' \tag{5.24}$$

where n_0 is the peak density. Thus a plot of $\ln \frac{N(t)}{N(0)} + \Gamma_b t$ against $\frac{1}{3\sqrt{3}} \int_0^t n_0^2 \, dt'$ should be a straight line whose slope gives the negative of the three body loss coefficient. Such a plot is given in Fig 5.12. A straight line fit gives a three body loss coefficient of $\sim 10^{-28}\text{cm}^6/\text{s}$ with a confidence interval of just a few percent. The agreement with the theoretical value in [31] is excellent and differs from the measured value in [**?**] by only a factor of two. However the value of the slope depends on the 6^{th} power of the measured mean frequency and the 6^{th} power of the width of the TOF signals so the relative error in the slope is quite large (at least a factor of 2 or 3). In any case the goodness of fit of the data to a straight line in the given plot is a strong indication that three body losses play a dominate roll in the dynamics of the trap.

5.3 The Experiments

Efficient forced evaporation requires selectively ejecting the more energetic atoms from the trap such that the remaining atoms thermalize to a lower temperature with a higher phase

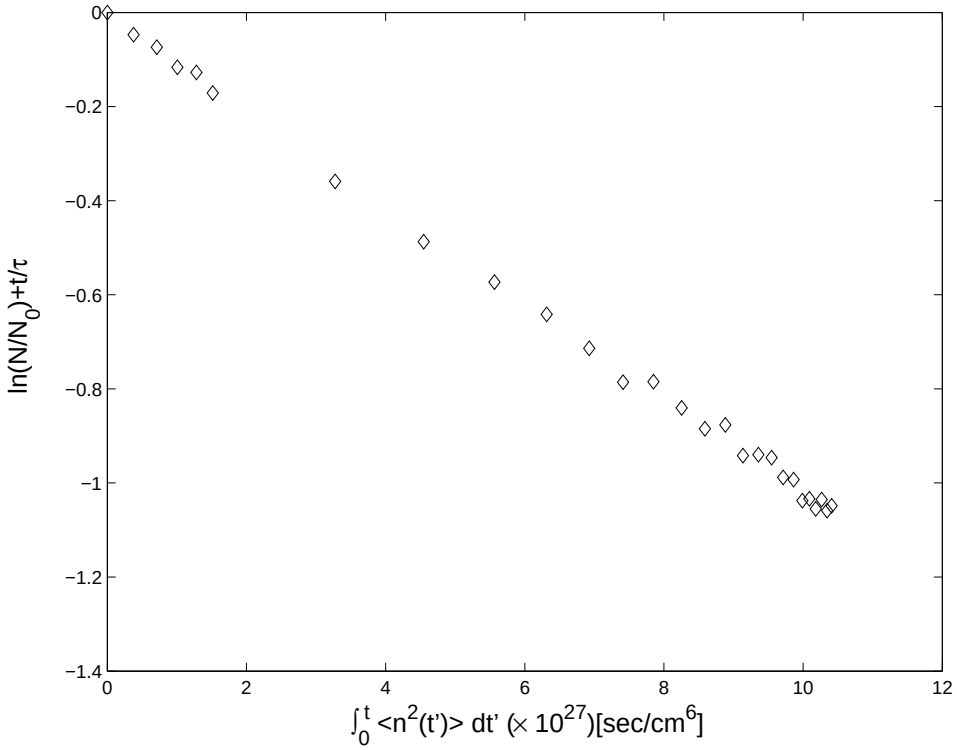

Figure 5.12: Determination of the three body loss rate. Slope of straight line fit gives the negative of the three body loss rate.

space density. In our system the obvious way to do this is to is to lower the trap depth by decreasing the power in the beams. This technique has been used before in a system very similar to ours [1] but with somewhat limited success. The drawback to the method is that lowering the trap depth lowers the elastic collision rate and can eventually lead to a stagnation of the process. In our case the thermalization rate falls by about a factor of 50 during the process but due to the excellent starting conditions it remains fast enough for us to achieve BEC in ~ 2.5 seconds as we describe in this section.

5.3.1 Observation of the Condensate

The experiment itself is straightforward. The trap is loaded as per the standard procedure and, immediately upon loading, the power is ramped down so as to sustain the evaporation process. In the original experiment [**?**], the power was ramped from full power to 1 W in the first second. Over the next second the power was further reduced to some final variable power which was followed by a further half second delay before probing. This scheme was largely a matter of practicality, and after a little software programming we were able to implement more general ramps. It was found that a simple exponential decay gave comparable results provided, of course, that the decay constant was chosen appropriately (typically 400ms to 500ms).

Observation of the transition from thermal cloud to condensate is as simple as lowering the final power in the experiment and Fig 5.13 shows at different final powers for the trapping beams. The first image shows a cloud well above criticality and has the classic isotropic momentum distribution expected from a thermal cloud. As the evaporation proceeds to lower powers, a bimodal distribution appears with a central non-isotropic component characteristic of condensation. As the power is lowered further, the central, non-spherical peak of the distribution becomes more prominent and the spherical pedestal diminishes. At a trap power of 190mW, the resulting cloud is almost pure condensate and contains about 35000 atoms. For lower powers the cloud rapidly diminishes as the trap can no longer support gravity. Line profiles of the images are also given. These profiles are taken along the minor axis of the resulting condensate. Also shown are fits to the thermal part of the cloud.

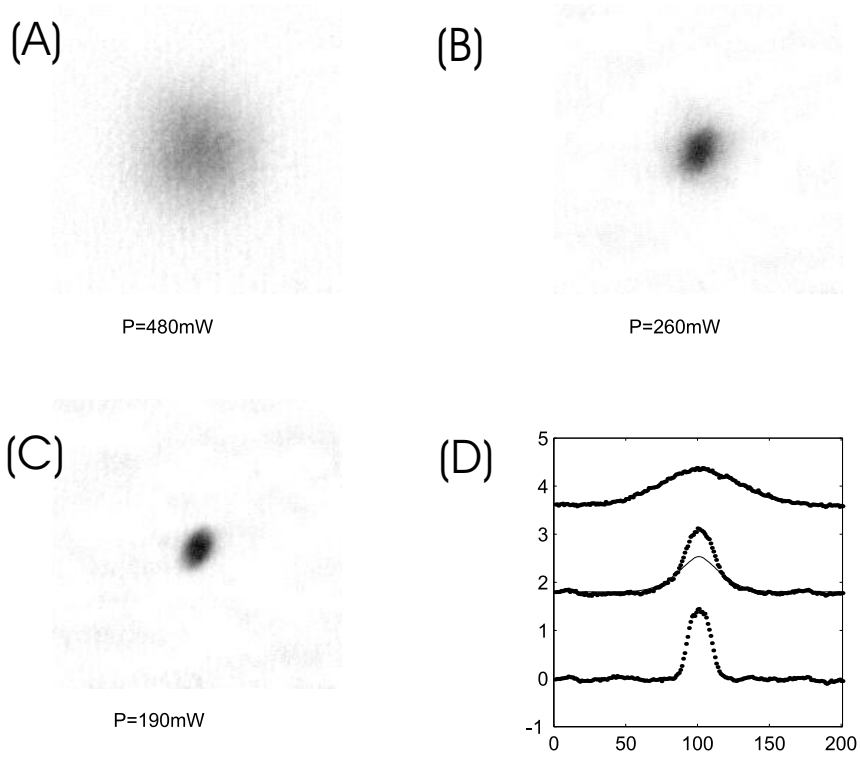

Figure 5.13: Images of the cloud as the final power is reduced. Images were taken after a 10ms ballistic expansion. (a) Thermal cloud (P=480mW), (b) thermal-condensate mixture (P=260mW), (c) pure condensate (190mW), (d) Line profiles taken from the three images illustrating the bimodal distribution

5.3.2 Condensate Expansion

Another feature of a condensate that distinguishes it from a thermal distribution is its behavior under ballistic expansion which reflects the anisotropic momentum distribution. Quantitative comparison with theory requires knowledge of both the trap frequencies and principle axes of the trap, and this can be a difficult task. The principle axes depend on the beam size, ellipticity and alignment and in our system the trap beams are aberrated due to off center propagation through the lenses (required to overlap the beams), and the fact that the beam is not a pure TEM_{00} spatial mode. Furthermore the frequencies of the trap cannot be reliably measured at the lowest powers. If a condensate is formed the excitation spectrum can be altered by its presence [20] and if it is not the signal is too small to provide a useful spectrum. As a compromise we measure the trap frequencies above the critical temperature and rely on the scaling of the frequencies with power. For the data shown here we have used the set up in which no frequency splitting was observed. At P = 200mW we measured frequencies of 120Hz and 260Hz and so the estimated frequencies at P = 100mW are 85Hz and 185Hz.

Using these frequencies we may use equation (5.18) to determine the expansion coefficients b_i. In addition we can use equations (5.14) and (5.17) to determine the chemical potential and radii of the condensate. In Fig 5.14 we show the aspect ratio that one would expect and also plotted is the measured values. In Fig 5.15 we show the absolute sizes, both measured and theory. We note that the measured sizes are somewhat larger than predicted (by about $15-20\%$). A slight calibration error in the camera magnification could contribute to this, but most likely it is due to a systematic error in determining the frequency. As we have noted earlier the measured frequencies could well be expected to be lower than the real frequencies due to the anharmonic nature of the potential.

5.3.3 Growth of the Condensate

Once criticality has been reached the condensate fraction should grow according to equation (5.9) where the critical temperature T_c is given in equation (5.8). Determining the temperature and condensate fraction is done using 2D fits to the absorptive images as

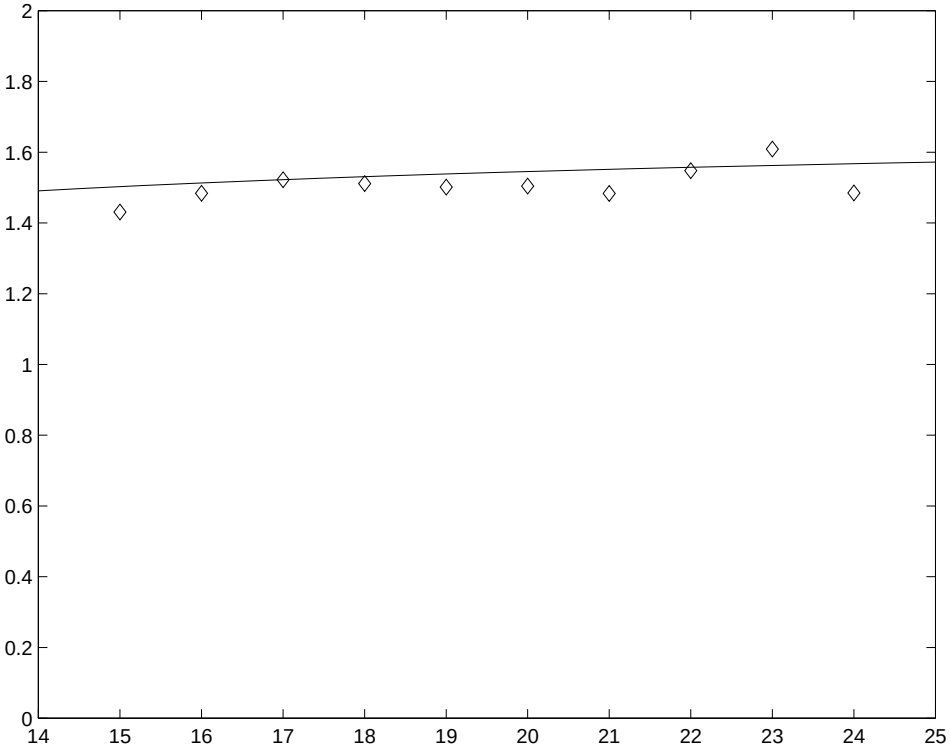

Figure 5.14: Evolution of the aspect ratio of the cloud during time of flight - both measured and theory

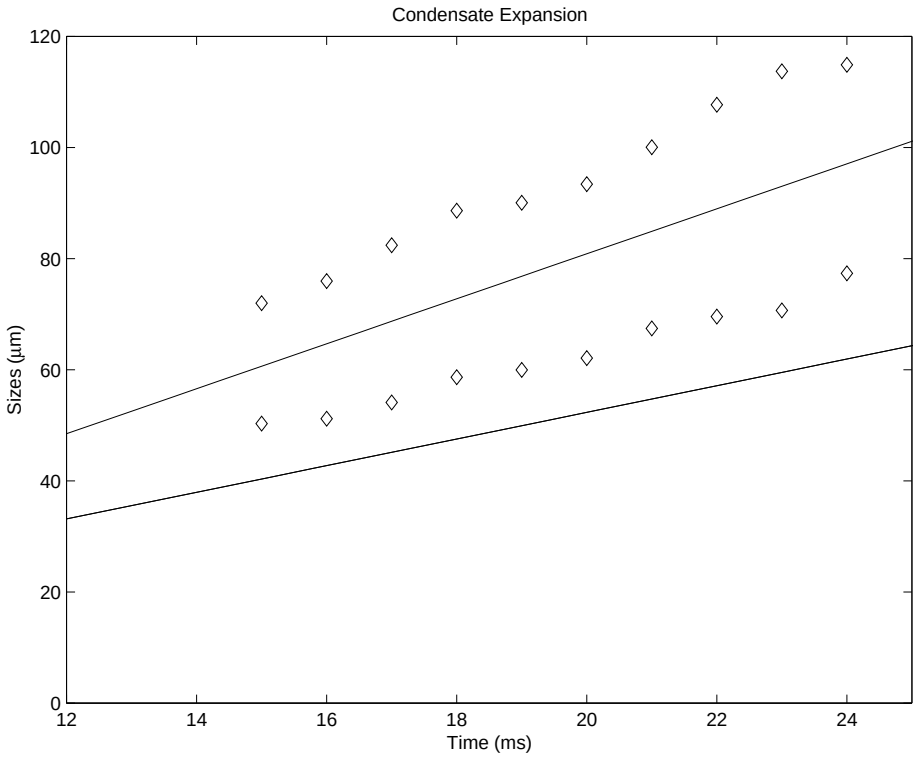

Figure 5.15: Plots illustrating the expansion of the condensate - both measured and theory. The discrepancy between theory and experiment is possibly due to measurement error in the frequencies - see text.

described in [82],[51]. Briefly the integrated density profile is fitted to the form

$$\tilde{n} = a_{th} g_2 \left[e^{-\frac{r^2}{2\sigma^2}} \right] + a_c max \left(1 - \frac{x^2}{\sigma_x^2} - \frac{y^2}{\sigma_y^2}, 0 \right)^{3/2} \tag{5.25}$$

The first term describes the bose-enhanced thermal distribution and the second term describes the condensate density profile according to the Thomas-Fermi limit. With this fitting function comes two implicit assumptions worth noting. The first is the isotropic nature of the thermal cloud which is valid provided the expansion time $\tau = 10$ms satisfies $(\omega\tau)^2 \gg 1$. From the measured frequencies the lowest frequency considered is 50Hz giving $\omega\tau \sim 3$ so the assumption is reasonable. The second assumption concerns the condensate term. This term is found by integrating the Thomas-Fermi density profile along a principle axis. Well this is perfectly valid in all other BEC systems where the principle axes are well known, this should be treated with some caution in our system where the principle axes are unknown due to beam abberation. However if one takes an ellipsoid and integrates it through an arbitrary axis the resulting distribution is well approximated by the form given in equation (5.25) particularly for the aspect ratios found here. Finally, we work in a rotated coordinate system and restrict the aspect ratio in a manner consistent with the pure condensate found at the lowest powers. The results concerning the condensate fraction are plotted in Fig 5.16. Also plotted is the theoretical curve for the purposes of comparison. The agreement is reasonable given the scatter in the data and the fact that the mean frequency may not precisely follow the scaling with power used in determining the critical temperature.

5.3.4 Condensate Lifetime

In Fig 5.17 we plot the number of atoms in the condensate as a function of time from which we infer a lifetime of about $3 \sim 4$ seconds. This is significantly shorter that the 10 second lifetime measured above at high power and for the single beam geometries. There are a number of possible reasons for the reduced lifetime, and we discuss each of these in turn. Firstly, in magnetic traps, significant heating and subsequent reduction in lifetime is known to occur due to the presence of a diffuse cloud of hotter atoms commonly referred to as the oort cloud. In our trap it is plausible that the wings of the trap may provide an

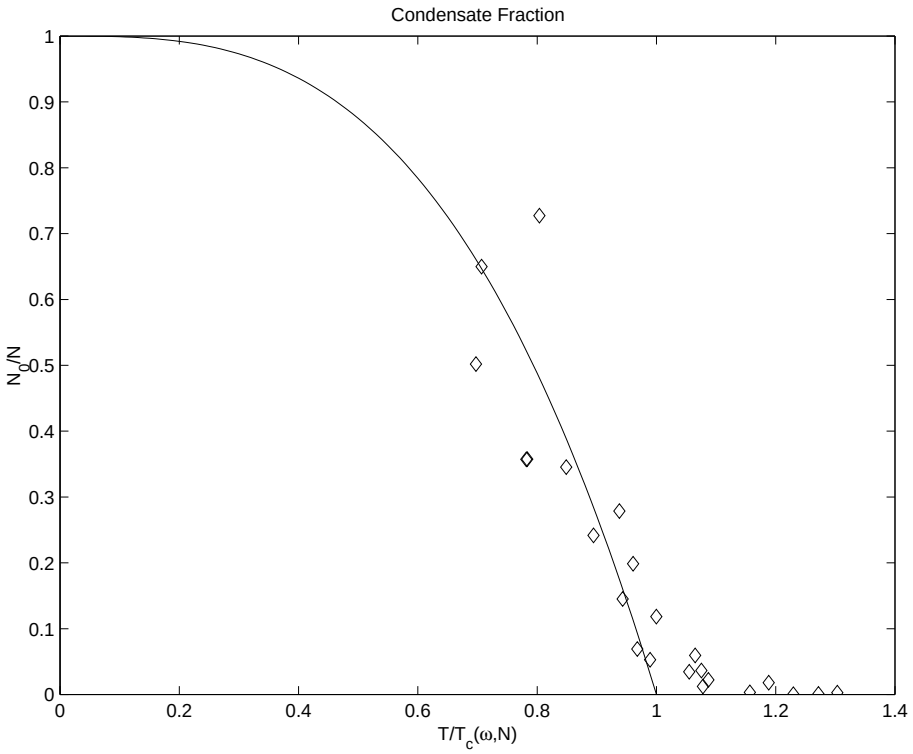

Figure 5.16: Plot showing the growth of the condensate as a function of scaled temperature

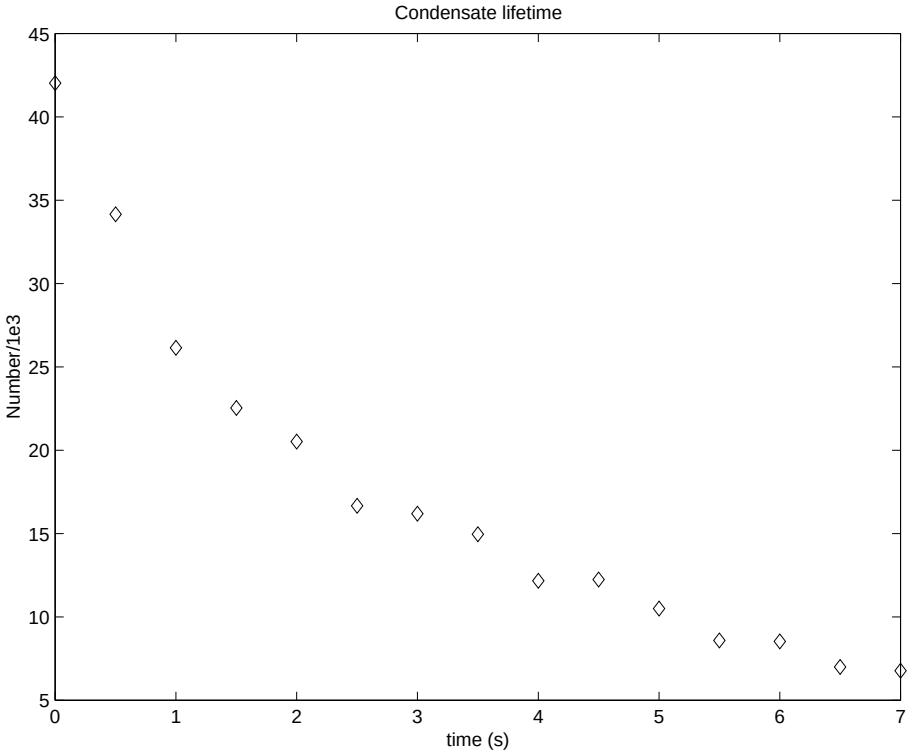

Figure 5.17: Plot showing the decay of the condensate with time. From this data we estimate a lifetime of $3 \sim 4$ seconds

analogous situation. After loading, a small fraction of atoms can be detected in the wings by absorptive imaging. However, as time proceeds the wings dissipate and we have been unable to detect these atoms at low power. Furthermore, the wings are not expected to support atoms at the lowest trap depths due to the effects of gravity.

A second possible mechanism is three body losses observed at high powers and has been seen in a number of experiments. From the estimated frequencies and measured number of atoms we infer a peak density of $1.610^{14}\text{atomscm}^{-3}$. For a ^{87}Rb condensate in the $|F = 1, m_F = -1 >$ state the three body loss coefficient has been measured at $5.8(1.9) \times 10^{-30}\text{cm}^6/\text{s}$ [14] giving an initial loss rate of $\sum 0.05\text{s}^{-1}$. Enhancement of the three-body loss rate and trap heating due to secondary collisions has been discussed in the literature (see [38], and [10]) with an eight-fold increase in the three body rate being reported in [78]. However, these regimes are only applicable to large condensates or those

confined to very deep traps so it is unlikely that three-body recombination is responsible for the observed decay.

A third possibility is trap instability stemming from laser fluctuations in both intensity and position. Attempts to observe heating at higher powers in the thermal cloud showed residual cooling. However since evaporation cannot be simply switched off this result is somewhat inconclusive. Furthermore heating due to laser fluctuations would be frequency specific and therefore depend on the power. As a practical matter it is not possible to have a useable thermal cloud at the powers where condensation is achieved simply because the signal is very low making data extraction unreliable.

Finally, it should be noted that off-resonant scattering from the MOT beams may well contribute to the problem. In setting up the system it was found that the finite extinction ratio of the AOM's caused a considerable decrease in the trap lifetime which was remedied by shuttering the repump light. The measured extinction ratio of the AOM's exceeds 40dB and the net power delivered to the chamber is thus estimated to be $\sim 10\mu$W. From the spatial characteristics of the beams we thus estimate a total intensity of $0.002\mathrm{I}_{sat}$. Since this light is 6.8GHz detuned the estimated scattering rate is $7.510^{-3}\mathrm{s}^{-1}$ giving a net heating of $\sim$ 3nK/s. This heating is obviously negligible for any thermal cloud but the mean field energy of the condensate is estimated to be 60nK. Thus stray light may well contribute to the rapid decay. In future experiments this should be ruled out by using RF switches to improve the isolation of the AOM's or by using shutters to eliminate the problem altogether.

5.3.5 The M-State Situation

Throughout the work involved in this thesis no consideration was ever given to the distribution amongst the Zeeman sub-levels. For technical reasons associated with the extinction ratio of the AOM's, the atoms were transferred to the $F = 1$ ground state manifold, but this was done by simply leaving the MOT beams on after shuttering the repump. Thus no optical pumping to a specific m-state should be expected. Having achieved BEC without regard to this fact it is therefore of interest to probe the m-state distribution. This is done in a fairly simplistic manner. After loading a bias field is switched on and after the conden-

Figure 5.18: Image taken of condensate expansion in a magnetic field gradient

sate is released the MOT coils are switched on and the force induced by the field gradient is enough to separate the spin components. The resulting image is shown in Fig 5.18. Assuming the circularly polarized probe optically pumps the atoms so that they scatter the same number of photons we infer a 3:1:1 weighting of the $m_F = -1, 0, 1$ sub-states. In the current system we are unable to probe the spin mixture in the initial thermal cloud as the components do not cleanly separate. Thus we cannot be sure if the measured distribution is a consequence of the condensation process or arises from some pumping process during loading. Given the nature in which the atoms are loaded the latter possibility seems unlikely. A plausible explanation for the M-State distribution would be the presence of field gradients within the chamber which would give rise to state dependent potentials. If the zero of the field is located within say 1mm of the trap center this would give rise to favorable evaporation from the $m = 0, 1$ states leaving a predominate population in the $m = -1$ state as observed. Further evidence of this was found when the power was reduced until all

three clouds diminished completely. When this was done the $m = 1$ cloud disappeared first followed quickly by the $m = 0$ and then the $m = -1$ as the power was reduced. Further evidence of this effect was found by implementing evaporation with the MOT coils turned on which left the entire population in the $m = -1$ state. With regards to expected gradients, the ion pump spec-sheet indicates that it would give a field gradient of ~ 25mG/cm at the trap. Over 1mm this corresponds to an energy of just ~ 200nK. Additionally the coils used to cancel residual fields do not have a strictly Helmholtz geometry so that, if the trap is off-center with respect to these coils, there can be an appreciable gradient from them. Assuming a displacement of 1mm we would estimate a field gradient comparable to that from the ion pump. Given that these gradients give rise to such small energy shifts across the relevant length scales it would be likely that the effect would manifest itself at the lowest trap depths. However in monitoring the populations as one crosses the condensation point we have seen no significant change in the measured distribution. The spinor nature will be the subject of future investigations.

5.3.6 The Evaporation Process

In this experiment we ramp the power down using a exponential ramp with a time constant of 500ms. At variable powers the ramp is stopped and the sample probed. This is essentially what was done above but here we explore the entire range of powers spanned during the ramp. Temperature is measured by fitting the absorptive images to a two dimensional gaussian which is sufficient as we restrict our attention here to temperatures above criticality.

It is difficult to compare the data to the scaling laws discussed earlier as it is unclear what constitutes the effective trap depth. The reason for this is simply because of the roll gravity plays as the power is ramped down particularly as it pertains to the diagonal beam. Due to gravity the diagonal beam cannot itself support the atoms at powers on the order of $1 \sim 2$W. Thus at low powers the trap depth would be closer to that of the single beam. We illustrate this in Fig 5.19 where we plot the depth of the cross trap including gravity vs. the depth of the single beam trap in the absence of gravity. In addition it is unclear that the wings of the trap even play a roll in the evaporation during the ramp down. In [1] it was argued that atoms which escape from the central region but remain confined by the wings

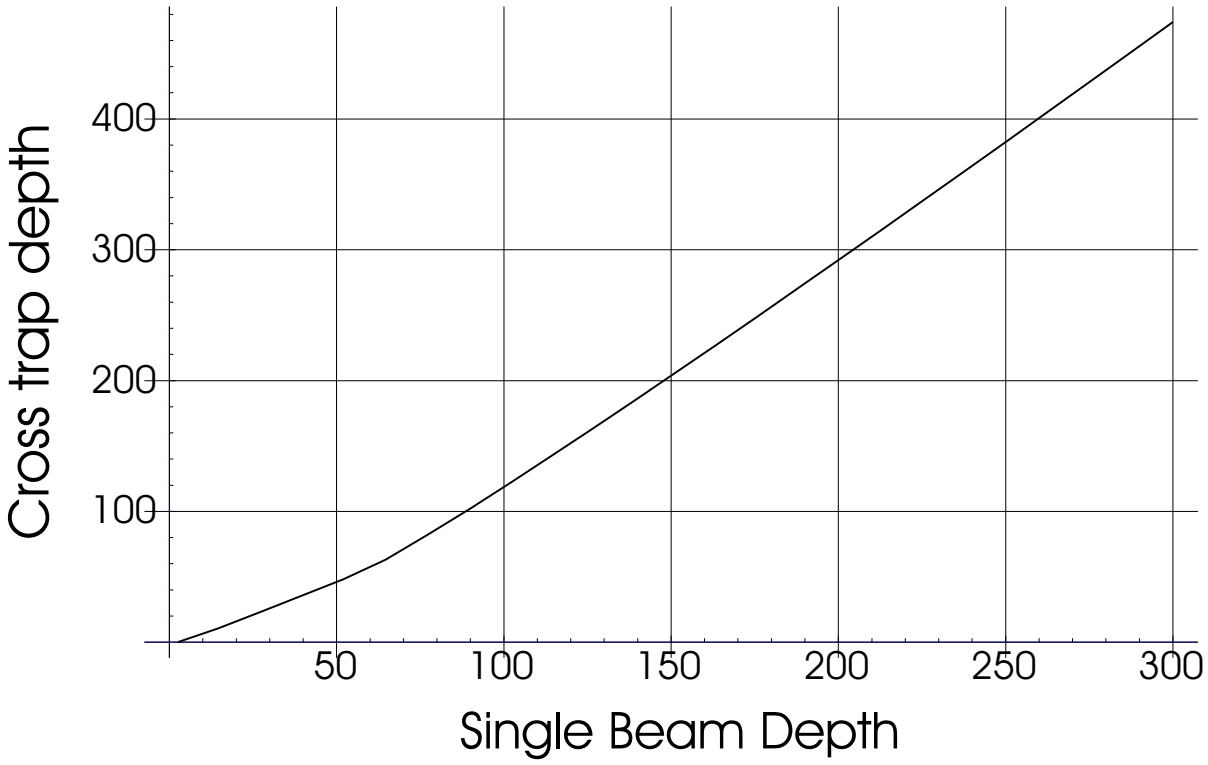

Figure 5.19: Plot showing the depth of the cross trap as a function of the depth of the single focus trap. Both are expressed in units of μK

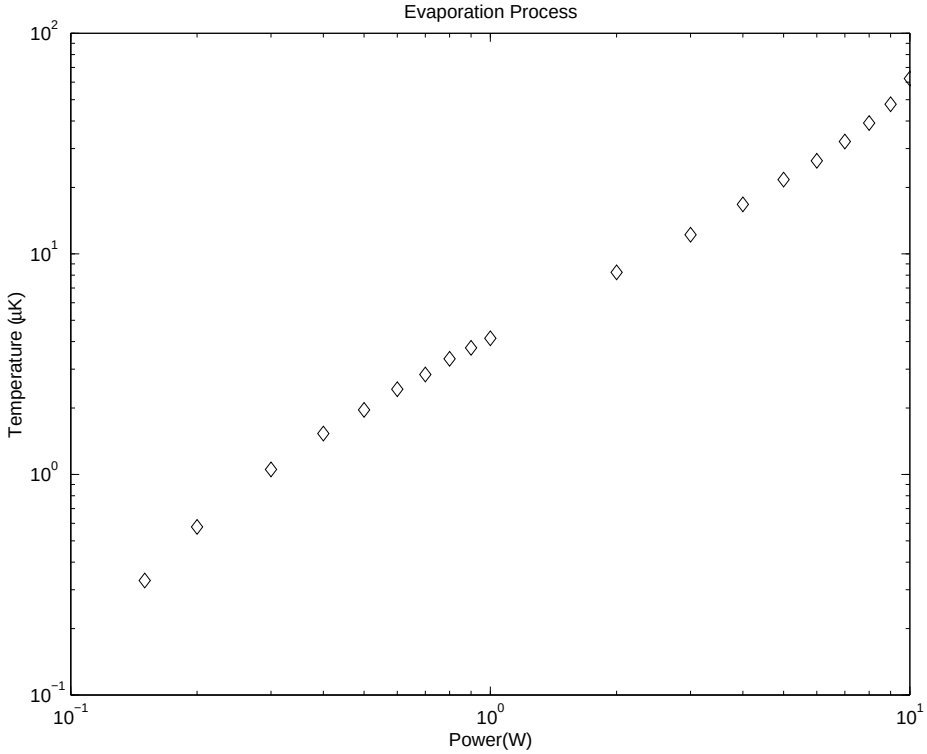

Figure 5.20: Plot showing the temperature as a function of power during the evaporation process.

would not play a significant role in the evaporation dynamics and due to the similarity of the trap geometries the same can be expected in our system. Nevertheless, as we see in Fig 5.20, there is an approximately linear relationship between power and temperature indicating a reasonably constant value of η. Further, in Fig 5.21, we plot the power vs psd on a loglog plot and shows a roughly linear trend as predicted by the scaling laws discussed earlier. Finally, in order to compare the simple harmonic oscillator model with experiment without the ambiguity associated with the trap depth we show in Fig 5.22 the temperature vs psd on a loglog plot. The agreement is not so unreasonable considering the shortcomings of the model.

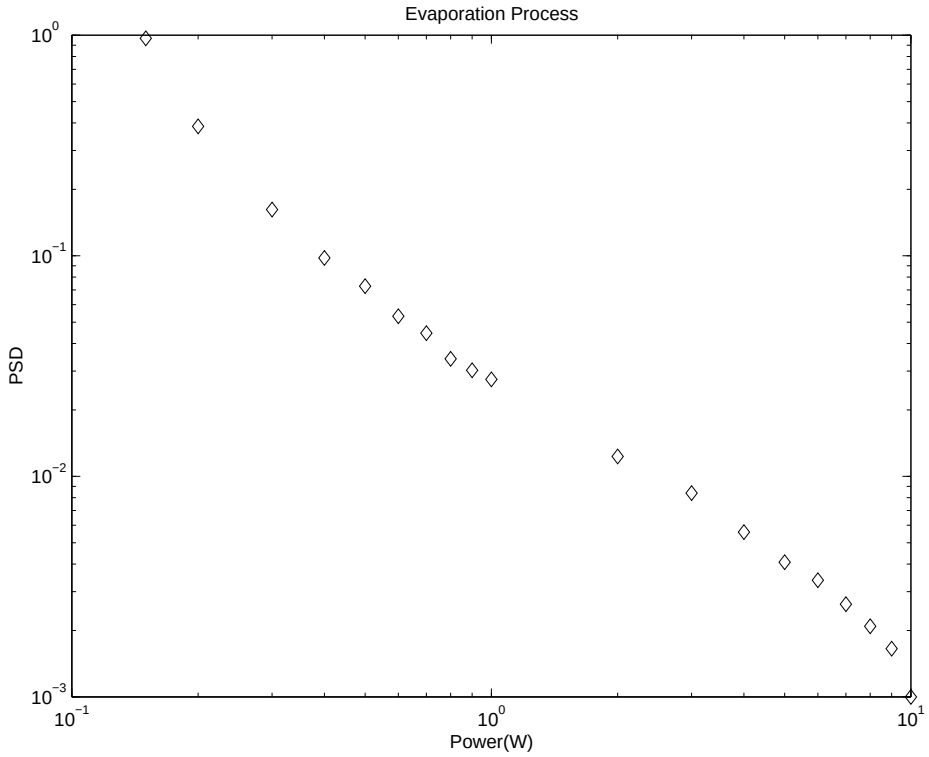

Figure 5.21: Plot showing the phase space density as a function of power during the evaporation process.

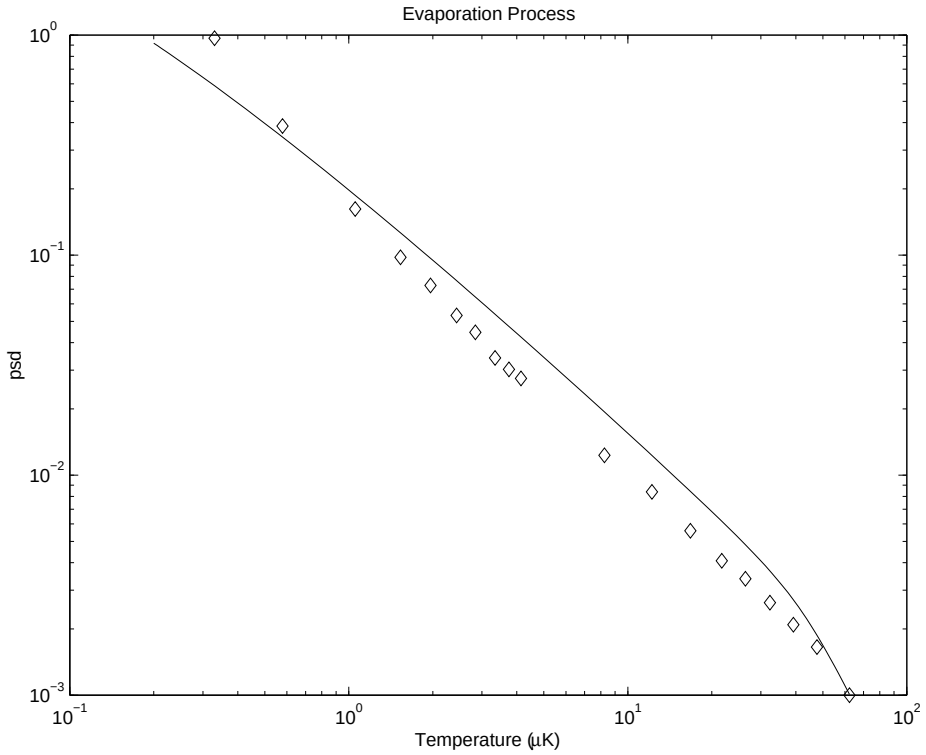

Figure 5.22: Plot showing the phase space density as a function of temperature during the evaporation process. The solid curve is taken from the SHO model derived earlier.

5.4 A Comparison With Other Work

To our knowledge there is only one other experiment that can be directly compared to ours, namely that done by Steven Chu's group at Stanford [1]. This experiment was in many respects identical to ours and it is worthwhile to compare the two. In their experiment a 10W Nd:YAG laser ($\lambda = 1.06\mu$m) was used for the trapping laser for sodium atoms. Each beam had a maximum power of 4W and had a minimum waist of 15μm. In terms of the actual evaporation itself the experiments are quite comparable. With a factor of 20 change in the power, as in their experiment, we observe a factor of 50 increase in the phase space density compared to their quoted factor of 28 with the difference most likely due to the way in which phase space density in computed. In this thesis we have always used the fact that $\rho \sim N\omega^3/T^3 \sim NP^{1.5}/T^3$ and applying this to their results gives an estimated increase of ~ 48. The three most notable differences between these experiments are the scattering rate from the trapping beams, the lifetime of the trap and, most importantly, the initial conditions.

The scattering rate from the Nd:YAG laser at the highest powers used was quoted at about 1.6 photons per second whereas in our system it is practically zero. Well the scattering rate did give rise to an observed heating in their system it is most likely inconsequential to the forced evaporation in which the power, and therefore scattering rate, is significantly reduced on the time scale of the initial scattering rate. This same comment applies to the lifetime of their trap which varied inversely to the power. At the lowest powers the lifetime was comparable to that of our system where no dependence on power has been observed.

The most significant difference between the experiments is, of course, in the initial conditions. Our initial densities are almost two orders of magnitude higher, resulting in faster evaporation, and the starting phase space density is higher by a factor of 10. Furthermore we start with 2×10^6 atoms compared to their 5000 which ultimately means we can lower the power further and still maintain a viable signal. Indeed in our system we have been able to change the power by a factor of 150 compared to their factor of 20. Thus our superior starting conditions mean we have less work to do with more power to do it.

It is worth speculating why there were so few atoms in their experiment. This work involved sodium and the MOT operates on the $3^2\mathrm{S}_{1/2} - 3^2\mathrm{P}_{3/2}$ which has an associated

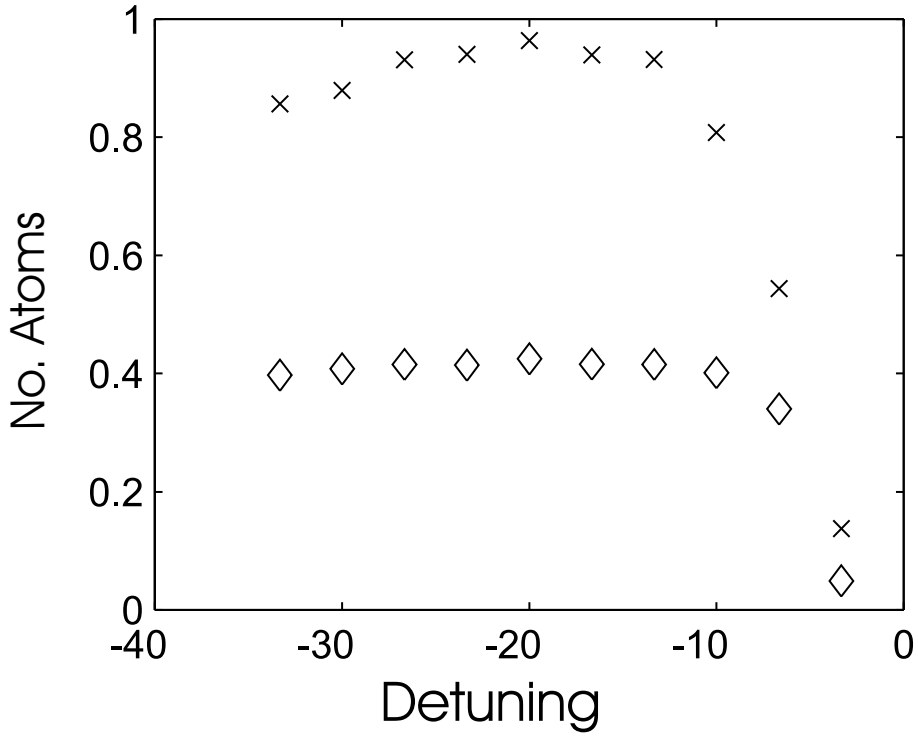

Figure 5.23: The significance of detuning the beams during loading. Crosses show the number of atoms after 300ms and the diamonds show the number of atoms after 1 second

wavelength of 589.16nm. Thus the trapping potential will, to a good approximation, be proportional to the static polarizability, α_s[84]. Now the difference in α_s between the $3^2S_{1/2}$ ground state and $3^2P_{3/2}$ excited state is a factor of 2.2 [28]. With a trap depth of 900μK $\sim$ 19MHz one would then expect the atoms at the trap center to be stark shifted by 22MHz. This exceeds the detuning used for their MOT (15 MHz) so that atoms would actually be repelled from the trap center. Thus only the edge of the trap would be loaded successfully. To illustrate the significance of detuning the beams we plot the number of atoms vs. detuning in Fig 5.23 for our system. The two sets of data correspond to different times at which the measurements are made and in either case we see that the number is severely reduced when operating near the detuning typically used in a MOT.

Chapter 6

Some Final Remarks

In this thesis we have discussed our investigations of quasi-electrostatic traps or QUEST's. These studies lead us to a new method by which to create a Bose condensate that frees one from the constraints imposed on the magnetic trappers. The relatively low initial densities achieved in magnetic traps means that the initial evaporation proceeds slowly placing stringent requirements on the background pressure in the vacuum. The typical time to create a condensate in a magnetic trap is $30-60$ seconds and requires a background limited lifetime measured in minutes. In our system the job is done in $2-3$ seconds with a background limited lifetime of about 10 seconds.

An additional constraint imposed on the magnetic trapper is in what they may actually trap. Typically they are restricted to a particular m-state of a single hyperfine level with only a handful of experiments being able to investigate multi-component condensates. Furthermore, to investigate spinor condensates, researchers had to resort to transferring a condensate made in a magnetic trap to an optical trap and then using the method of adiabatic rapid passage to distribute the condensate among the hyperfine sub-levels. In our system we have no such prejudice on the internal state of the atom and the spinor condensate can be formed directly in the optical trap.

In this chapter we begin by summarizing our investigations and then contrast and compare our efforts with those of others. In doing so we will hopefully provide some insight into why the experiment succeeds where others have failed and explain the 'mystery' behind our excellent starting conditions [60].

6.1 Summary

The work involved in this thesis started with the construction of an all optical laser trapping system which enabled us to explore a number of QUEST geometries ranging from the simple single focus trap to the more ambitious 6 beam configuration. The appeal of this system is its simplicity, employing standard diode laser technologies and an off-the-shelf CO_2 laser. Well custom built CO_2 lasers, designed for the purpose of scientific research, have been used by other researchers, we have found that the SYNRAD1, designed for cutting and engraving, is a practical alternative for atom trapping and cooling. Indeed this same design has been used by others to achieve lifetimes exceeding one minute which is more than sufficient for most experiments in this field of research. Well the lifetime of our system is only 10 seconds, it is most probably limited by the vacuum and has proved sufficient for our purposes.

Our initial investigations began with a complicated 6 beam geometry with the hope of creating a system with tight confinement in all three dimensions and a ground state energy of 1μK. With the negligible scattering rate from the trapping beams, and the fact that the excited state of the atom is more tightly bound than the ground state, such a system would provide unique conditions for the prospect of achieving quantum degeneracy by laser cooling techniques only [32]. However this system lacked a clear signature expected of a 3-D structure and exhibited a certain degree of instability. This system was thus abandoned and investigations on more simple structures began.

When determining the lifetime of these more simple traps, the temperature was monitored, in addition to the number, and it became clear that evaporation was clearly an important factor determining the final temperature achieved in these traps. Furthermore this evaporation occurred on fairly rapid timescales ($\sim$ 1 second) giving rise to the possibility of achieving BEC via forced evaporation. In this system forced evaporation proceeds by ramping down the power in the beam which reduces the elastic collision rate slowing down the process. Thus high initial phase space densities and collision rates are vital ingredients for success in this type of system. Determining these properties as a function of power indicated the intuitively obvious fact that what was needed was a trap exhibiting both tight confinement and large trapping volume. For normal traps, those in which each dimension is well characterized by a single length scale, these features are contradictory: Large volume

requires a large length scale and tight confinement requires a small length scale.

To overcome this restriction the solution was to create a trap that is characterized by two length scales, one that determines the capture volume, and one that determines confinement. This is precisely what is provided by the cross trap. Loading volume is then pretty much defined by the sum of the volumes given by each single beam trap. Confinement, on the other hand, is determined by the intersection region provided the temperature is low enough so that, in (quasi-)equilibrium, all the atoms are restricted to this region. Such temperatures are largely unavoidable in this system due to the natural or free evaporation process and the result is very high initial densities and collision rates.

The initial conditions obtained in the cross trap seemed very promising for the achievement of condensation. Subsequent forced evaporation by lowering the power in the beams validated this and condensation by all optical means is now a reality.

6.2 The secret of our success

Loading the CO_2 trap is achieved by standard laser cooling techniques which are generally accepted as being density limited due to light assisted collisions, photo-association and re-absorption of scattered radiation. Thus the densities we achieve seem somewhat surprising. In [60] the initial conditions we achieve were quoted as being a mystery that remains to be solved with a number of researchers offering possible explanations. Here we offer two possible mechanisms both of which most likely play a role determining the high densities we see in the experiment.

The first possibility involves a dark spot mechanism which has been used by a number of researchers to increase the density obtained in a MOT to $\sim 10^{12}/cm^3$. In this technique the repump beam is shadowed at the center of the MOT or transiently reduced in intensity. This increases the fraction of atoms in the lower hyperfine state which does not interact with the cooling light and thus reduces the light assisted loss mechanisms. In our trap we implement a transient dark spot during loading but the trap itself induces an additional dark spot effect due to the induced stark shift. This is because the trapping potential is proportional to the static polarizability, α_s, which is different for the ground state and

excited state. Specifically, for the ground state we have $\alpha_s = 5.3 \times 10^{-39}\mathrm{m}^2\mathrm{C/V}$ and for the excited state we have $\alpha_s = 1.3 \times 10^{-38}\mathrm{m}^2\mathrm{C/V}$ thus the excited state experiences a larger shift by a factor of approximately 2.5. For the cross beam trap we estimate a depth for the ground state of $600\mu\mathrm{K} \sim 2\Gamma$ so that the atom experiences a blue detuning of $\sim 3\Gamma$. Since the repump is nominally on resonance and well below the saturation intensity we expect a reduction in the saturation parameter by almost a factor of 40.

One of the limitations of the dark spot which keeps densities to a relatively low value of $\sim 10^{12}/cm^3$ is repump scatter rendering the shadow less effective. This limitation is circumvented in our trap as it is the detuning of the atom which effects the dark spot mechanism. However, this is not the full story and in [87] it was noted that effective dark spots for the larger alkalis, particularly Cesium and Rubidium, required forced depumping with an additional laser beam. Thus, well the dark spot effect may help, it is most probably not the only contributing factor to the high densities obtained. We now offer an additional mechanism which is in the spirit of the treatment given in [73] and was touched on in chapter 4.

When laser cooling into a conservative traps it is intuitively appealing to assume the resulting density distribution is a direct consequence of the laser cooling process. However, in this system at least, it is not obvious that the densities obtained arise from this mechanism alone. Indeed, from the lifetime curves of any of the traps it is clear that evaporation dynamics after the cooling light is extinguished cannot be simply ignored. The earliest one can reliably extract data in our system is $50 - 100$ms which is longer than typical collision and oscillation times of the system. Thus it is very possible that the 'initial' distributions measured in this system stem from a redistribution of the energy after the cooling light has been extinguished. We illustrate this point using a very simple argument.

Suppose the cross beam trap is filled to a depth U_0 with atoms at a uniform density of $10^{12}/\mathrm{cm}^3$ where U_0 is the depth of a single beam trap[1]. Assuming a beam waist of $\sim 40\mu$m and a trap depth $U_0 = 300\mu$K it is relatively straight forward to show that the number of atoms is $\sim 2.3 \times 10^6$ with an average potential energy of $\sim 0.7U_0$. In thermal equilibrium this energy must be redistributed according to the equipartition principle. Assuming a harmonic

[1]This picture is consistent with images taken immediately after loading

oscillator approximation for the final distribution we thus have $0.7NU_0 = 3Nk_bT$ giving $T = 70\mu$K which is roughly consistent with our simple harmonic oscillator approximation. Well this is a very simplistic treatment, these numbers are in fair agreement with our observations. Numerical simulations of the type described in [3] have been performed by fellow student Su Yi and validate this rough calculation. In this simulation 3 million atoms with an initially uniform density of $10^{12}/\text{cm}^3$ at the center of the trap are left to thermalize. The result is a peak density of $10^{14}/\text{cm}^3$ after 50ms evolution. In this simulation the velocity distribution takes a longer time to reach a thermal distribution but this is most likely due to the extreme initial condition of all the atoms being completely stationary.

The initial conditions are the key to our success in achieving BEC and here we have presented two possible mechanisms to explain why we obtain densities typically considered beyond the reach of standard laser cooling techniques. In the present set up it is difficult to verify these as valid mechanisms as better imaging would be needed to directly probe the density profile during loading. Nevertheless the simple arguments mentioned above are physically appealing and do explain some of the qualitative features of the data as discussed in chapter 4. Furthermore these arguments illustrate the important point that one should be wary of jumping to the conclusion that high densities measured after laser cooling are a direct consequence of the laser cooling itself. This is particularly so if the delay between cooling and probing is larger than a collision or oscillation time of the system in which case redistribution processes can play a significant role. Thus it is fair for us to say we laser cool into the trap and achieve high densities but we cannot lay claim to the achievement of high density laser cooling. Well this may seem somewhat moot it has to be realized that laser cooling at high densities remains an important problem in this field. The point we make is that we have perhaps not solved this problem but merely found a means to bypass it.

6.3 Improvements to the current experiment

The X-trap experiment was implemented in a very straightforward manner and there is much room for improvement. The two major improvements pertain to the choice of trapping laser and the vacuum chamber design. Here we discuss these two points in turn.

6.3.1 The trapping laser

While the synrad1 laser has sufficed for the work done in this thesis it would be of interest to have more power available in the beams. The Coherent E DIOS LC-100NV laser is spec'ed to have $\geq 100W$ of power with a better mode quality than the Synrad1. Using one of these lasers instead we could then increase the beam power by a factor of at least 5 greatly increasing the possibilities available to the experimenter. With this much power one could achieve frequencies of $\sim$ 4kHz giving a Lamb-Dicke parameter $\eta \sim 1$ for which ground state cooling mechanisms have been identified [69]. Alternatively, and keeping within the spirit of the work done in this thesis, larger beam sizes could be used well maintaining either the trap depth or the trapping frequencies. This would possibly lead to larger condensates and perhaps even the creation of a condensate directly in an optical lattice[2].

Another possibility is to keep the waist small so as to realize a system in which the Stark shift of the atomic resonance greatly exceeds the linewidth of the atom. Well such a situation would mostly likely hinder the loading scheme used in this work, other possibilities can be envisaged. For example, in [75] it was shown that a MOT could be formed using cooling on the $F = 1 \rightarrow F' = 0$ transition while repumping on the $F = 2 \rightarrow F' = 1$ line. If one was to implement this by repumping on the $F = 2 \rightarrow F' = 2$ instead, the effect of a large Stark shift would be to shift the repump beams to a cooling configuration on the $F = 2 \rightarrow F = 3$ transition, like that used in this thesis, and the MOT beams would be shifted to the repump transition line $F = 1 \rightarrow F' = 1$. If successful this could bypass one major problem associated with the loading scheme used here, namely the dissipation of the MOT under the loading configuration. One would obtain the best of both worlds: Efficient capture outside the trap and efficient cooling inside.

With regards to our remarks at the end of chapter 5 it may well be possible to implement the X-trap experiment using a more user friendly wavelength for which more standard optics apply. If so this would certainly be an advantage. CO_2 laser optics can be expensive, as is the laser itself, and ZnSe windows limit the chamber bake out to 200^oC. Given the simplicity of the experiment it would be well worth the effort to investigate this

[2]Although technical problems associated with returning 100W of power to the laser may make this prohibitive.

as a possibility and, if successful, would make BEC studies as accessible as is the MOT.

6.3.2 Chamber Design

Most of the shortcomings of the experiment stem from the chamber design itself and much more could be achieved with a more appropriately designed chamber[3]. Basically the chamber is far larger than it needs to be and the viewports protrude out to such an extent that they restrict the imaging capability. By moving to a more compact design it should be possible to move the focusing optics outside the chamber. This would simplify the task of aligning the cross beam trap immensely and also make it possible to directly characterize the beam at its focus. In the present system we need to rely on inferences made by the characterization of the trap. This is undesirable since, for example, it is known that the anharmonic nature of the trap can shift the measured frequencies from those present at the bottom of the well.

The second and more important advantage of having a more compact design is the improvement that can be gained in the imaging capability. A factor of π increase in resolution would make in situ imaging a possible and worthwhile alternative. This would mean that the one could, via phase contrast imaging, monitor the evolution of the trap during loading and thus possibly shed light on the origins of the ultra-high densities we obtain. Verifying the mechanism proposed in the previous section would have important consequences as it could show that trap dynamics after cooling has terminated are as significant, if not more so, than the cooling processes themselves. Well our investigations in which we varied the power in the trapping beams provided circumstantial evidence supporting this idea, in situ imaging would provide direct, incontrovertible evidence of this fact.

6.4 Future Directions

Having made a condensate directly in an optical trap the natural question is what role might the result have in future research? Magnetic trapping has become a very well developed technology and condensates with 10^6 atoms are now somewhat routine. In our system it is

[3]In fairness to the designer it was not designed with the intention of making a BEC in a cross beam dipole trap.

unlikely that such large condensates could be made but it does offer the advantages of being technically simple, fast, and amenable to those species that cannot be easily confined in a magnetic trap. A noteworthy example is that of spinor condensates which simply cannot be held in a magnetic trap. Spinor condensates have been extensively studied by transferring a condensate to a dipole trap and then using the method of adiabatic rapid transfer to distribute the condensate among the hyperfine sub-levels. Our system would vastly simplify such experiments and, additionally, provide the opportunity to study directly the formation of such a condensate.

We have argued above that a more user friendly wavelength of $1.06\mu m$ may well suffice to achieve condensation via this technique. If this could be shown to be possible it would make the study of BEC far more accessible as no special technology or equipment would be needed beyond that needed for a MOT. Furthermore our technique has a somewhat less stringent requirement on the vacuum which is important for applications in which ultra high vacuum conditions are difficult to achieve.

Finally the technique need not be limited to a cross beam geometry. All that is needed is a geometry which incorporates a large loading volume and tight confinement. Such geometries are easily created by optical potentials. By superimposing a deep single focus trap with a weak lattice it may be possible to cool the atoms down into the lattice and thereby create an array of condensates directly in a lattice.

Appendix A

Evaporation Model

Here we give the explicit expressions for each of the terms used in the evaporation model discussed in chapter 2. These terms are most simply expressed in terms of incomplete gamma functions defined by

$$P(a,x) = \frac{1}{\Gamma a}\int_0^x t^{a-1}e^{-t}\,dt \tag{A.1}$$

It is also convenient to define the ratio of these functions, that is,

$$R(a,x) = \frac{P(a+1,x)}{P(a,x)} \tag{A.2}$$

and we note that all of this functions have limiting values of one as $\eta \to \infty$.

A.1 Evaporation terms

We first introduce the rate γ_{ev} defined by

$$\gamma_{ev} = \frac{m\bar{\omega}^3\sigma}{\pi^2 U_0} \tag{A.3}$$

where m is the mass, $\bar{\omega}$ is the geometrically averaged frequency, σ is the elastic cross-section, and U_0 is the trap depth. Using this rate we have

$$\dot{N}_{ev} = -\gamma_{ev}\left[\frac{\eta P(3,\eta) - 4P(4,\eta)}{P(3,\eta)^2}\right]\eta e^{-\eta}N^2 \tag{A.4}$$

and

$$\begin{aligned}\dot{\eta}_{ev} = -\gamma_{ev}&\left(\eta + \frac{\eta P(3,\eta) - 4P(4,\eta) - P(5,\eta)}{\eta P(3,\eta) - 4P(4,\eta)} - 3R(3,\eta)\right)\\ &\times\left(\frac{\eta P(3,\eta) - 4P(4,\eta)}{12P(5,\eta)P(3,\eta) - 9P(4,\eta)P(4,\eta)}\right)\eta^2 e^{-\eta}N\end{aligned} \tag{A.5}$$

A.2 Three body loss terms

We first introduce the rate γ_{3B} given by

$$\gamma_{3B} = L\left(\frac{m\bar{\omega}^2}{2\sqrt{3}\pi U_0}\right)^3 \tag{A.6}$$

and two integral expressions

$$f_1(\eta) = \sqrt{\frac{54}{\pi}}\int_0^{\sqrt{2\eta}} u^2 e^{\frac{3}{2}}(P(\frac{3}{2},\eta-\frac{u^2}{2}))^3\,du \tag{A.7}$$

$$f_2(\eta) = \sqrt{\frac{27}{8\pi}}\int_0^{\sqrt{2\eta}} u^2 e^{\frac{3}{2}}(P(\frac{3}{2},\eta-\frac{u^2}{2}))^2\left(3P(\frac{5}{2},\eta-\frac{u^2}{2})+u^2P(\frac{3}{2},\eta-\frac{u^2}{2})\right) \tag{A.8}$$

both of which are calculated numerically and have limiting values of one as $\eta \to \infty$. In terms of these quantities we have

$$\dot{N}_{3B} = -\gamma_{3B}\eta^3 N^3 f_1(\eta) \tag{A.9}$$

$$\dot{\eta}_{3B} = -\frac{\gamma_{3B}}{3}\eta^4 N^2\left[\frac{3f_1(\eta)R(3,\eta)-2f_2(\eta)}{R(3,\eta)(4R(4,\eta)-3R(3,\eta))}\right]. \tag{A.10}$$

The numerical integrations can be avoided by simply replacing the term in square brackets by its asymptotic value of 1 and $f_1(\eta)$ by one. This is equivalent to ignoring truncation effects which is a reasonable approximation for the values used in the text.

A.3 Terms due to potential changes

We have $\mathcal{N} = U_0^2/(6(\hbar\bar{\omega})^3)$ and remembering that $\bar{\omega} \propto \sqrt{U_0}$ we obtain

$$\dot{N}_\theta = \frac{\eta^3 e^{-\eta}}{4P(3,\eta)} N\frac{\dot{U}_0}{U_0} \tag{A.11}$$

$$\dot{\eta}_\theta = -\eta\frac{\dot{U}_0}{U_0}\left[\frac{\eta^3 e^{-\eta}(1+\eta-3R(3,\eta))-6P(3,\eta)}{12P(4,\eta)(4R(4,\eta)-3R(3,\eta))}\right] \tag{A.12}$$

Note that if η is large then we have

$$\dot{\eta}_\theta = \eta\frac{1}{2}\frac{\dot{U}_0}{U_0} \tag{A.13}$$

consistent with a simple adiabatic change of the potential with no atom loss.

Appendix B

SHO Approximation

Here we discuss the validity of the approximations used to estimate densities and phase space densities throughout this thesis. The approximation essentially assumes an infinitely deep harmonic oscillator and as we shall see this approximation can be quite crude. We use the truncated Boltzmann distribution as discussed in [64] and throughout it is assumed, without loss of generality, that the potential is zero at the trap center

B.1 General Form of the Distribution

For an infinitely deep well, a thermal gas is described by the phase space distribution

$$f_0(\mathbf{r},\mathbf{p}) = n_0\Lambda^3 \exp\left(-(U(\mathbf{r}) + p^2/2m)/k_bT\right) \tag{B.1}$$

where n_0 is the peak density and $\Lambda = (2\pi\hbar^2/mk_bT)^{1/2}$ is the thermal de Broglie wavelength. Integration over momentum space leads to the well known density distribution function.

$$n(\mathbf{r}) = n_0 \exp(-U(\mathbf{r})/k_bT) \tag{B.2}$$

For a finite depth trap strict equilibrium is not possible as it is accompanied by continuing evaporation. However the gas can be well characterized by a quasi thermal equilibrium in which the phase space distribution above is restricted to that part of phase space in which the energies are less than the trap depth. This leads to the modification

$$n(\mathbf{r}) = n_0 \exp(-U(\mathbf{r})/k_bT) P(3/2, (\epsilon_t - U(\mathbf{r}))/k_bT) \tag{B.3}$$

where $P(3/2, x)$ is the incomplete gamma function introduced in Appendix A and ϵ_t is the trap depth. n_0 is no longer the peak density, rather we have $n(0) = n_0 P(3/2, \epsilon_t/k_bT) \leq n_0$,

but $n_0\Lambda^3$ still remains a proper measure of the phase space density. Thus to find the appropriate expressions for phase space density and density it remains to find n_0 which can be found by integrating the spatial density over all space and equating the result to the number of trapped atoms, i.e.

$$N = \int_V n_0 \exp(-U(\mathbf{r})/k_bT) P(3/2, (U_0 - U(\mathbf{r}))/k_bT)\, d^3r \tag{B.4}$$

Calculation of this integral can be facilitated by introducing $V(U)$ which is the volume of space contained by the equipotential surface U. This reduces the 3 dimensional integral to the one dimensional form

$$N = \int_0^{\epsilon_t} n_0 \exp(-U/k_bT) P(3/2, (\epsilon_t - U)/k_bT) \frac{dV}{dU}\, dU \tag{B.5}$$

and in what follows it is convenient to write the potential in the non-dimensional form $U = U_0 u$ so that we have

$$N = \int_0^{\beta} n_0 \exp(-\eta u) P(3/2, \eta(\beta - u)) \frac{dV}{du}\, du \tag{B.6}$$

Here we have adopted a slightly different set of definitions from that in [64]. Specifically we have defined $\eta = U_0/k_bT$ and $\beta = \epsilon_t/U_0$. Typically $\beta = 1$ and the definitions coincide. However in the case of the single focus and cross trap it is necessary to choose $\beta < 1$ for reasons to be discussed.

B.2 Single Focus

It is relatively straight forward to show that

$$\frac{dV}{du} = \frac{\pi w_0^2 z_r}{3} \sqrt{\frac{u}{1-u}} \frac{3-2u}{(1-u)^2} \tag{B.7}$$

so that we have

$$N = \frac{\pi w_0^2 z_r}{3} \int_0^{\beta} n_0 \exp(-\eta u) P(3/2, \eta(\beta - u)) \sqrt{\frac{u}{1-u}} \frac{3-2u}{(1-u)^2}\, du \equiv \frac{\pi w_0^2 z_r}{3} f(\eta, \beta). \tag{B.8}$$

Using the known expressions for the trap frequencies, this equation can be rewritten as

$$N \left(\frac{m\bar{\omega}^2}{2\pi k_b T} \right)^{3/2} = n_0 \frac{2}{3\sqrt{\pi}} \eta^{3/2} f(\eta, \beta) \tag{B.9}$$

Recognizing the left-hand side of the equation as the harmonic oscillator approximation to the density, n_{HO}, we may then write the true density as

$$n(0) = n_0 P(3/2, \beta\eta) = \left(\frac{3\sqrt{\pi}}{2} \frac{P(3/2, \beta\eta)}{\eta^{3/2} f(\eta, \beta)} \right) n_{HO}. \tag{B.10}$$

The term in brackets is thus the depth dependent correction factor for the density. Unfortunately the integral represented by $f(\eta, \beta)$ is divergent for $\beta = 1$ due to a pole in the integrand at $u = 1$. Typically an approximation is used for the potential such that the integral converges. Here we simply set $\beta < 1$ which in effect simulates approximately the effect of gravity which truncates the potential at $u < 1$. For the single focus trap discussed in chapter 4 the appropriate upper limit for the integral can be shown to be ~ 0.8 but we note that in general this depends on U_0. Specifically, if we write $\alpha = mgw/U_0 \ll 1$, then it can be shown that the true depth is approximately $U_0(1 + \alpha^2/4 - (\alpha^2/e)^{1/3})$.

Since the phase space density is given by $n_0\Lambda^3$ it is reasonably straightforward to show that the true phase space density is given by

$$\rho = \left(\frac{3\sqrt{\pi}}{2} \frac{1}{\eta^{3/2} f(\eta, \beta)} \right) \rho_{HO}. \tag{B.11}$$

For most η values considered the correction factor for both densities is essentially the same and could be as much as a factor of two. It should be noted that the difference in correction factors for the two densities is always $P(3/2, \beta\eta)$ independent of the trap geometry and, since this is practically one for most values of η of interest we focus only on the expressions for density. Fig B.1 shows this correction factor as a function of η for $\beta = 0.8$.

B.3 Lattice

For the lattice trap we have

$$\frac{dV}{du} = \frac{\pi w_0^2}{k} \frac{\arccos\sqrt{1-u}}{1-u} \tag{B.12}$$

and the expression for the peak density is thus

$$n(0) = n_0 P(3/2, \beta\eta) = \left(\frac{\sqrt{\pi}}{2} \frac{P(3/2, \beta\eta)}{\eta^{3/2} f(\eta, \beta)} \right) n_{HO}. \tag{B.13}$$

where $f(\eta, \beta)$ is now given by

$$f(\eta, \beta) = \int_0^\beta n_0 \exp(-\eta u) P(3/2, \eta(\beta - u)) \frac{\arccos\sqrt{1-u}}{1-u}\, du \tag{B.14}$$

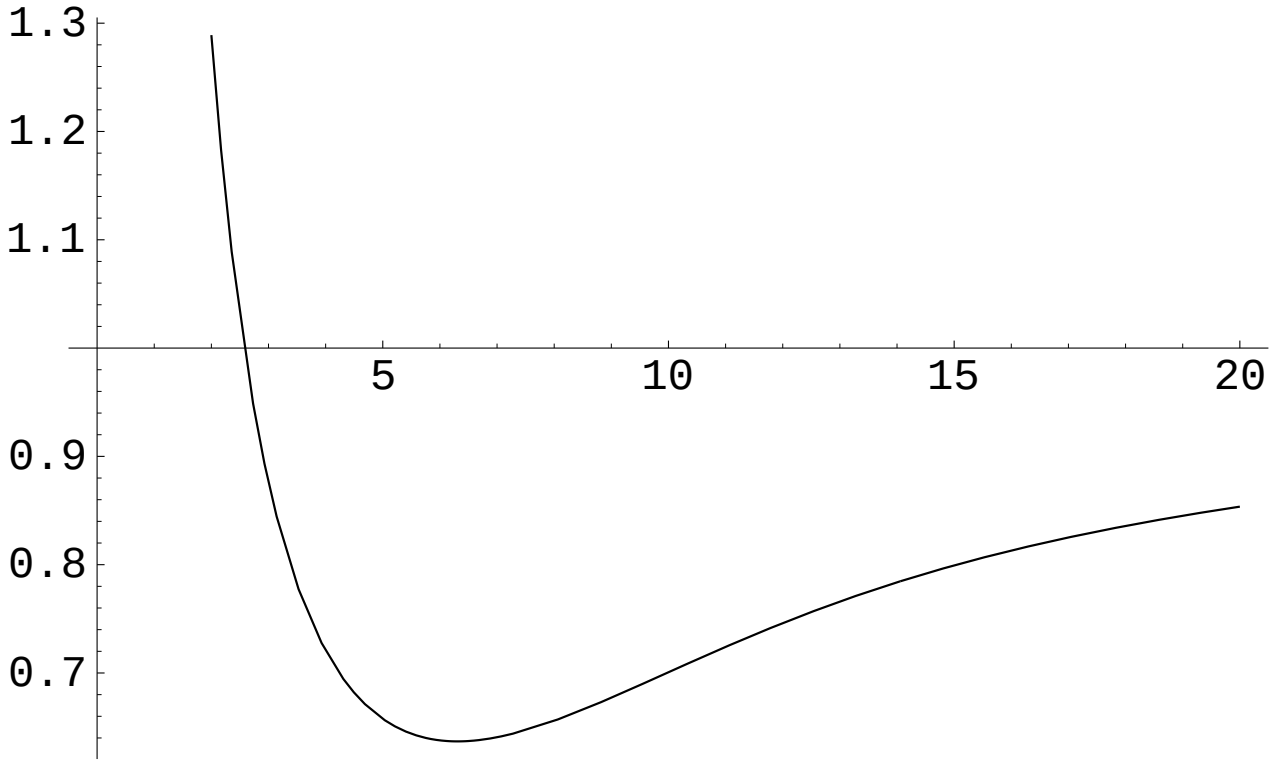

Figure B.1: Correction factor for single beam trap

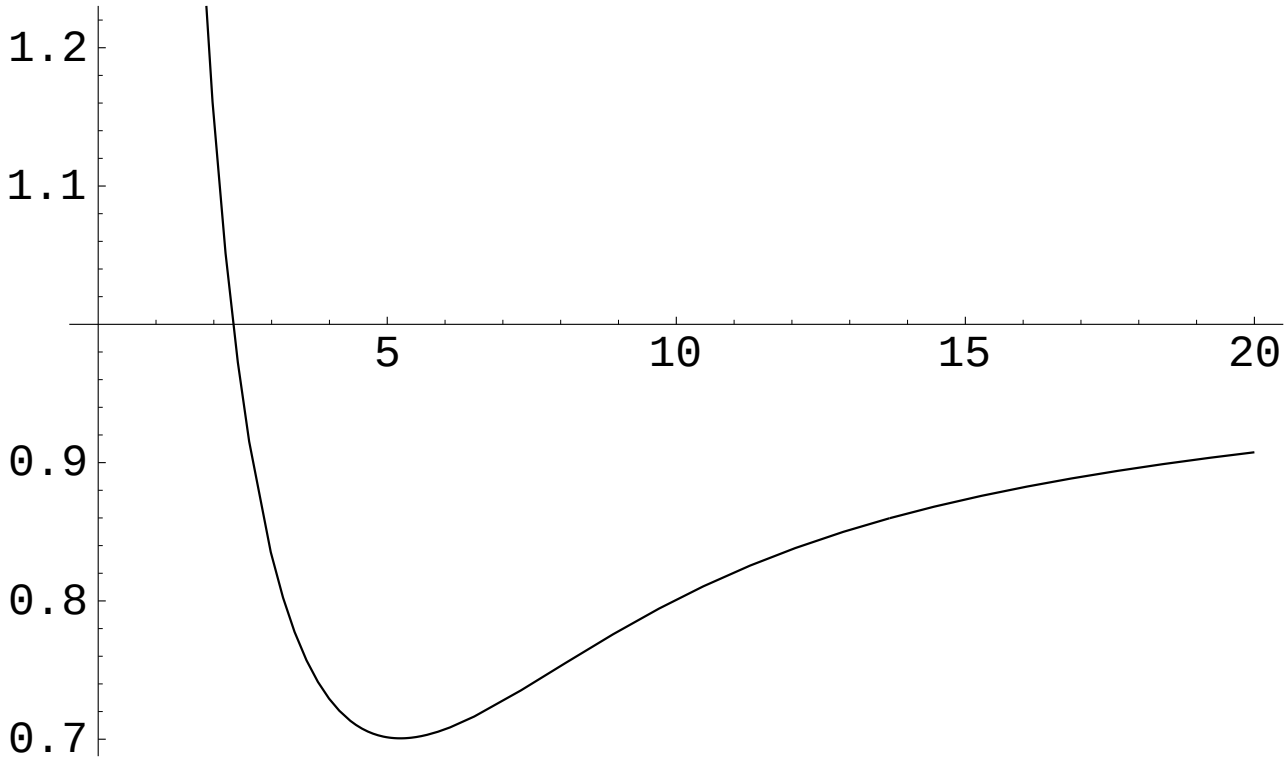

Figure B.2: Correction factor for lattice trap

In this case the integral converges for $\beta = 1$ and the inclusion of gravity is not needed. Fig B.2 shows the dependence of the correction factor on η

B.4 Cross

For the cross trap we have not been able to find an analytical expression for $\frac{dV}{du}$ and so it is calculated numerically. The trap is completely characterized by $\kappa = \pi w_0/\lambda$, which is the ratio of the rayleigh range to the waist, and by the trap depth U_0 for the single beam. Here we choose $\kappa = 12$ which is appropriate for a waist of $\sim 40\mu$m used in the experiment. By scaling each length coordinate by w_0 we may write

$$\frac{dV}{du} = w_0^3 \rho_v(u). \tag{B.15}$$

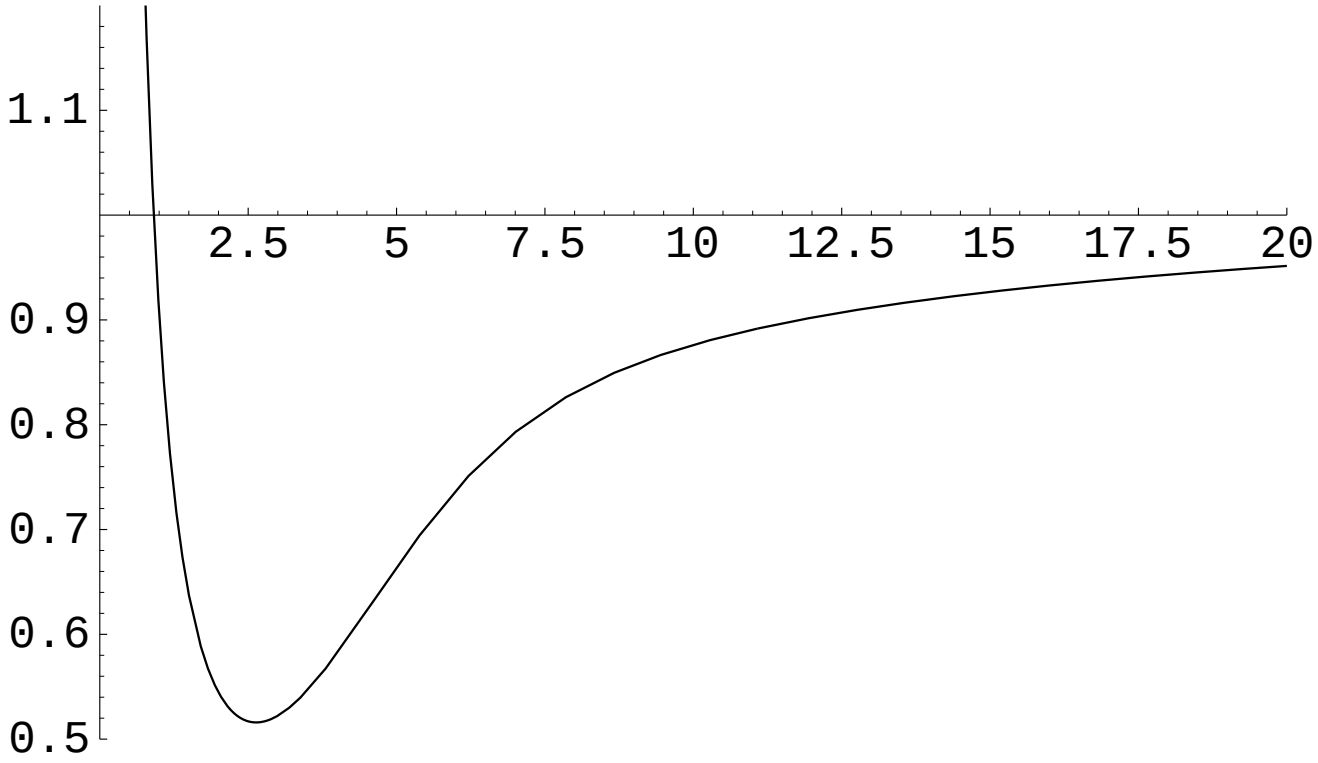

Figure B.3: Correction factor for cross trap

By normalizing $\frac{dV}{du}$ in this fashion we can then write the peak density as

$$n(0) = \frac{\pi^{3/2}}{4} \frac{P(3/2, \beta\eta)}{\eta^{3/2} f(\eta, \beta)} \tag{B.16}$$

where the integral $f(\eta, \beta)$ is given by

$$f(\eta, \beta) = \int_0^\beta n_0 \exp(-\eta u) P(3/2, \eta(\beta - u)) \rho_v(u)\, du \tag{B.17}$$

In this expression we have used $\eta = U_0/k_b T$ and $\beta = \epsilon_t/U_0$ as before but U_0 is now the depth of a single beam trap. As in the case of the the single beam trap β depends on U_0 and at full power $\beta \sim 1.5$. Fig B.3 illustrates this case. From the life time curves in chapter 5 we estimate that evaporation stagnates at $\eta \sim 8$ and so the correction in this case is is much smaller than for the previous two cases.

Finally it is worth while at this point to estimate what percentage of the atoms are actually present in the wings of the cross beam structure. An atom is free to move in the

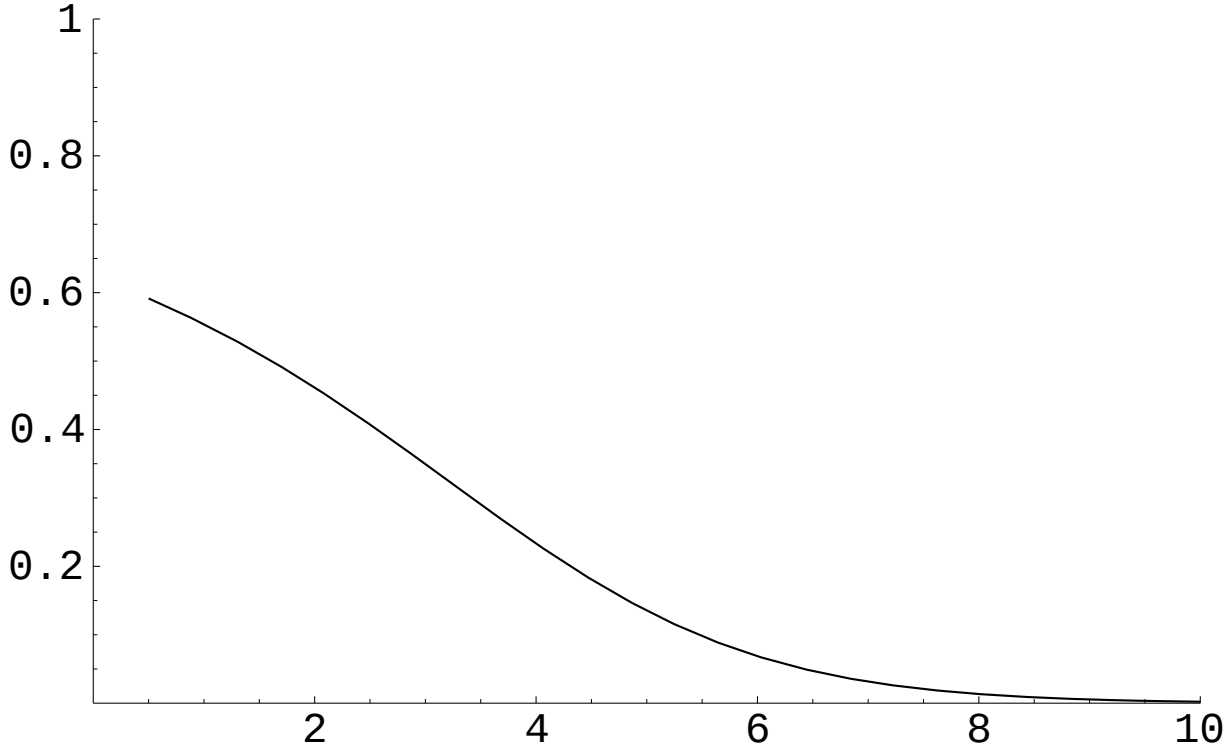

Figure B.4: Fraction of the trapped atoms in the wings

wings if it has an energy greater than U_0 and so the number of atoms in the wings is given by

$$N_{wings} = w_0^3 n_0 \int_1^\beta \exp(-\eta u) P(3/2, \eta(\beta - u)) \rho_v(u)\, du \tag{B.18}$$

Since the total number of atoms is

$$N = w_0^3 n_0 f(\eta, \beta) \tag{B.19}$$

we have

$$\frac{N_{wings}}{N} = \frac{1}{f(\eta, \beta)} \int_1^\beta \exp(-\eta u) P(3/2, \eta(\beta - u)) \rho_v(u)\, du. \tag{B.20}$$

In fig B.4 we plot this ratio as a function of η for a truncation $\beta = 1.5$. The choice of 1.5 is motivated by the fact the one of the beams lies on the diagonal which lowers the truncation significantly.

Bibliography

[1] C. S. Adams, H. J. Lee, Nir Davidson, Mark Kaesevich, and S. Chu. Evaporative cooling in a cross dipole trap. *Phys. Rev. Lett.*, 74(18):3577–3580, 1995.

[2] Kyungwon An. *The Microlaser: Study of laser oscillation with one atom in an optical resonator*. PhD thesis, MIT, 1995.

[3] H. Wu an C. J. Foot. Simulating evaporation. *J. Phys. B*, 29:L321, 1996.

[4] M. H. Anderson, J. R. Ensher, M. R. Matthews, C. E. Wieman, and E. A. Cornell. Observation of bose-einstein condensation in a dilute atomic vapor. *Science*, 269:198–201, 1995.

[5] M. H. Anderson, W. Petrich, J. R. Ensher, and E. A. Cornell. Reduction of light-assisted collision loss rate from a low-pressure vapor-cell trap. *Phys. Rev. A*, 50(5):R3597, 1994.

[6] A. Aspect, E Arimondo, R. Kaiser, N. Vansteenkiste, and C. Cohen-Tannoudji. Laser cooling below the one photon recoil energy by velocity selective coherent population trapping. *Phys. Rev. Lett.*, 61(7):826, 1988.

[7] Vanderlei Bagnato, David E. Pritchard, and Daniel Kleppner. Bose-einstein condensation in an external potential. *Phys. Rev. A.*, 35(10):4354–4358, 1987.

[8] S. Bali, K. M. O'Hara, M. E. Gehm, S. R. Granade, and J. E. Thomas. Quantum-diffractive background collisions in atom-trap heating and loss. *Phys. Rev. A*, 60(1):R29, 1999.

[9] M. D. Barrett, J. A. Sauer, and M. S. Chapman. All-optical formation of an atomic bose-einstein condensate. *Phys. Rev. Lett.*, 87(1):010404, 2001.

[10] H. C. W. Beijerinck. Heating rates in collisionally opaque alkali-metal atom traps: Role of secondary collisions. *Phys. Rev. A*, 62:063614, 2000.

[11] Kirstine Berg-Sorensen. Kinetics for evaporative cooling of a trapped gas. *Phys Rev. A*, 55(2):1281–1287, 1997.

[12] H. M. J. M. Boesten, C. C. Tsai, J. R. Gardner, D.J. Heinzen, and B. J. Verhaar. Observation of a shape resonanace in the collision of two cold ^{87}rb atoms. *Phys. Rev. A.*, 55:636, 1997.

[13] C. C. Bradley, C. A. Sackett, J. J. Tollett, and R. G. Hulet. Evidence of bose-einstein condensation in an atomic gas with attractive interactions. *Phys Rev. Lett.*, 75(9):1687–1690, 1995.

[14] E. A. Burt, R. W. Ghrist, C. J. Myatt, M. J. Holland, E. A. Cornell, and C. E. Wieman. Coherence, correlations and collisions: What one learns about bose-einstein condensates from their decay. *Phys. Rev. Lett.*, 79(3):337–340, 1997.

[15] Y. Castin, C. I. Cirac, and M. Lewenstein. Reabsorption of light by trapped atoms. *Phys. Rev. Lett.*, 80(24):5305, 1998.

[16] Y. Castin and R. Dum. Bose-einstein condensates in time dependent traps. *Phys. Rev. Lett.*, 77(27):5315–5319, 1996.

[17] Y Castin, H. Wallis, and J. Dalibard. Limits of doppler cooling. *J. Opt. Soc. Am. B*, 6(11):2046, 1989.

[18] J. I. Cirac, R. Blatt, and P. Zoller. Laser cooling of trapped ions in a standing wave. *Phys. Rev. A*, 46(5):2668, 1992.

[19] J. I. Cirac, M. Lewenstein, and P. Zoller. Collective laser cooling of trapped atoms. *Europhys. Lett.*, 35(9):647–651, 1996.

[20] Franco Dalfovo, Stefano Giorgini, Lev P. Pitaevskii, and Sandro Stringari. Theory of bose-einstein condensation in trapped gases. *xxx.lanl.gov/cond-mat*, 9806038v2, 1998.

[21] J. Dalibard and C. Cohen-Tannoudji. Dressed-atom approach to atomic motion in laser light: the dipole force revisited. *J. Opt. Soc. Am. B*, 2(11):1707–1720, 1985.

[22] J. Dalibard and C. Cohen-Tannoudji. Laser cooling below the doppler limit by polarization gradients: simple theoretic models. *J. Opt. Soc. Am. B*, 6(11):2023, 1989.

[23] J. Dalibard, J. M. Raimond, and J. Zinn-Justin, editors. *Fundamental systems in quantum optics*. North-Holland, 1990.

[24] Nir Davidson, H. J. Lee, Mark Kaesevich, and S. Chu. Raman cooling of atoms in two and three dimensions. *Phys. Rev. Lett.*, 72(20):3158–3161, 1994.

[25] K. B. Davis, M. O. Mewes, M. R. Andrews, N. J. van Druten, D. S. Durfee, D. M. Kurn, and W. Ketterle. Bose-einstein condensation in a gas of sodium atoms. *Phys Rev. Lett.*, 75(22):3969–3973, 1995.

[26] Ivan H. Deutsch and Poul S. Jessen. Quantum-state control in optical lattices. *Phys Rev. A*, 57(3):1972–1986, 1998.

[27] R. Dum, P. Marte, , T. Pellizzari, and P. Zoller. Laser cooling to a single quantum state in a trap. *Phys. Rev. Lett.*, 73(21):2829, 1994.

[28] Christopher R Ekstrom, Jörg Schmiedmayer, Michael S. Chipman, Troy D. Hammond, and David E. Pritchard. Measurement of the electric polarizability of sodium with an atom interferometer. *Phys. Rev. A*, 51(5):3883–3888, 1995.

[29] George Ellis. *Control Systems Design Guide*. Academic Press, Inc, 1991.

[30] H. Engler, T. Weber, M. Mudrich, R. Grimm, and M. Weidemüller. Very long storage times and evaporative cooling of cesium atoms in a quasielectrostatic dipole trap. *Phys. Rev. A*, 62:031402, 1999.

[31] B. D. Esry, Chris H. Greene, and Jr. James P. Burke. Recombination of three atoms in the ultracold limit. *Phys. Rev. Lett.*, 83(9):1751–1754, 1999.

[32] S. Friebel, C. D'Andrea, J. Walz, M. Weitz, and T. W. Hänsch. CO_2 laser optical lattice with cold rubidium atoms. *Phys. Rev. A*, 57:R20–R23, 1998.

[33] S. Friebel, R. Scheunemann, J. Walz, T. W. Hänsch, and M. Weitz. Laser cooling in a CO_2 laser optical lattice. *Applied Phys. B*, 67:699–704, 1998.

[34] M. E. Gehm, K. M. O'Hara, T. A. Savard, and J. E. Thomas. Dynamics of noise-induced heating in atom traps. *Phys. Rev. A*, 58(5):3914, 1998.

[35] K. E. Gibble, S. Kasapi, and S. Chu. Improved magneto-optic trapping in a vapor cell. *Optics Letters*, 17(7):526–528, 1992.

[36] J. P. Gordon and A. Ashkin. Motion of atoms in a radiation pressure trap. *Phys. Rev. A*, 21:1606, 1980.

[37] Rudolf Grimm, Matthias Weidemüller, and Yurri B. Ovchinnikov. Optical dipole traps for neutral atoms. *xxx.lanl.gov - physics/9902072*, 1999.

[38] D. Guery-Odelin and G. V. Shlyapnikov. Excitation-assited inelastic processes in trapped bose-einstein condensates. *Phys. Rev. A*, 61:013605, 1999.

[39] D. J. Han, M. T. DePue, and D. S. Weiss. Loading and compressing cs atoms in a very far-off-resonant light trap. *Phys. Rev. A.*, 63:023405, 2001.

[40] Dian-Jiun Han, Steffen Wolf, Steven Oliver, Colin McCormick, Marshall T. Depue, and D. S. Weiss. 3d raman sideband cooling of cesium atoms at high density. *Phys. Rev. Lett.*, 85(4):724, 2000.

[41] Tin-Lun Ho. Spinor bose condensates in optical traps. *Phys. Rev. Lett.*, 81:742, 1998.

[42] P. Horowitz and W. Hill. *The Art of Electronics*. Cambridge University Press, 1989.

[43] Zhen Hu. *Quantum optics with cold atoms - nonlinear spectroscopy and road toward single-atom trap*. PhD thesis, MIT, 1995.

[44] K Huang. *Statistical Mechanics*. Wiley, New York, 1963.

[45] Tetsuya Ido, Yoshitomo Isoya, and Hidetoshi Katori. Optical-dipole trapping of sr atoms at a high phase-space density. *Phys Rev. A*, 61:061403, 2000.

[46] R. Jàuregui, N. Poli, G. Roati, and G. Modugno. Anharmonic parametric excitation in optical lattices. *Phys. Rev. A*, 64:033403, 2001.

[47] P. S. Jessen and I. H. Deutsch. Optical lattices. *Advances in atomic molecular and optical physics*, 37:95–136, 1996.

[48] Mark Kaesevich and S. Chu. Laser cooling below a photon recoil with three-level atoms. *Phys. Rev. Lett.*, 69(12):1741–1744, 1992.

[49] W. Ketterle. Spinor condensates and light scattering from bose-einstein condensates. *cond-mat*, 0005001, 1999.

[50] W. Ketterle, K. B. Davis, M. A. Joffe, A. Martin, and D. E. Pritchard. High densities of cold atoms in a dark spontaneous-force optical trap. *Phys. Rev. Lett.*, 70(15):2253, 1993.

[51] W. Ketterle, D. S. Durfee, and D. M. Stamper-Kurn. Making, probing and understanding bose-einstein condensates. *cond-mat*, 9904034v2, 1999.

[52] Wolfgang Ketterle and N. J. Van Druten. Evaporative cooling of trapped atoms. *Advances in atomic, molecular, and optical physics*, 37:181–236, 1996.

[53] S. J. M. Kuppens, K. L. Corwin, K. W. Miller, T. E. Chupp, and C. E. Wieman. Loading an optical dipole trap. *Phys. Rev. A*, 62:013406, 2000.

[54] L. D. Landau and E. M. Lifschitz. *Mechanik*. Akademie-Verlag, Berlin, 1964.

[55] H. J. Lee, C. S. Adams, Mark Kaesevich, and S. Chu. Raman cooling of atoms in an optical dipole trap. *Phys. Rev. Lett.*, 76(15):2658–2661, 1996.

[56] Anthony J. Leggett. Bose-einstein condensation in the alkali gases: Some fundamental concepts. *Rev. Mod. Phys.*, 73(2):307–355, 2001.

[57] V. S. Letokhov, M. A. Ol'shanii, and Yu B ovchinnikov. Laser cooling of atoms: a review. *Quantum Semiclass. Opt.*, 7:5–40, 1995.

[58] P. D. Lett, W. D. Phillips, S. L. Rolston, C. E. Tanner, R. N. Watts, and C. I. Westbrook. Optical molasses. *J. Opt. Soc. Am. B*, 6(11):2084, 1989.

[59] P. D. Lett., R. N. Watts, C. I. Westbrook, W. D. Phillips, P. L. Gould, and H. J. Metcalf. Observation of atoms laser cooled below the doppler limit. *Phys. Rev. Lett.*, 61(2):169, 1988.

[60] B. G. Levi. Magnetic forces need not apply: Bec can be made in an optical trap. *Physics Today*, pages 20–22, July 2001.

[61] K. G. Libbrecht, R. A. Boyd, P. A. Willems, T. L. Gustavson, and D. K. Kim. Teaching physics with 670 nm diode lasers - construction of stabilized lasers and lithium cells. *Am. J. Phys.*, 63(8):729–737, 1995.

[62] K. G. Libbrecht and J. L. Hall. A low-noise high-speed diode laser current controller. *Rev. Sci. Instrum.*, 64(8):2133–2135, 1993.

[63] K. Lindquist, M. Stephens, and C. Wieman. Experimental and theoretical study of the vapor-cell zeeman optical trap. *Phys. Rev. A*, 46:4082, 1992.

[64] O. J. Luiten, M. W. Reynolds, and J. T. M. Walraven. Kinetic theory of the evaporative cooling of a trapped gas. *Phys Rev. A*, 53(1):381–389, 1996.

[65] K. B. MacAdam, A. Steinbach, and C. Wieman. A narrow-band tunable diode laser system with grating feedback, and a saturated absorption spectrometer for cs and rb. *Am. J. Phys.*, 60(12):1098–1111, 1992.

[66] I. Marzoli, J. I. Cirac, R. Blatt, and P. Zoller. Laser cooling of trapped three-level ions: Designing two-level systems for sideband cooling. *Phys. Rev. A*, 49(4):2771, 1994.

[67] Harold J. Metcalf and Peter van der Straten. *Laser Cooling and Trapping*. Springer-Verlag, 1999.

[68] H. J. Miesner, D. M. Stamper-Kurn, M. R. Andrews, D. S. Durfee, S. Inouye, and W. Ketterle. Bosonic stimulation in the formation of a bose-einstein condensate. *Science*, 279:1005, 1998.

[69] G. Morigi, J. I. Cirac, M. Lewenstein, and P. Zoller. Ground-state cooling beyond the lamb-dicke limit. *Europhys. Lett.*, 39(1):13–18, 1997.

[70] C. Munroe, D. M. Meekhof, B. E. King, S. R. Jefferts, W. M. Itano, D. J. Wineland, and P. Gould. Resolved-sideband raman cooling of a bound atom to the 3d zero-point energy. *Phys Rev. Lett.*, 75(22):4011, 1995.

[71] K. M. O'Hara. *Optical Trapping and Evaporative Cooling of Fermionic Atoms.* PhD thesis, Duke University, 2000.

[72] K. M. O'Hara, S. R. Granade, M. E. Gehm, T. A. Savard, S. Bali, C. Freed, and J. E. Thomas. Ultrastable CO_2 laser trapping of lithium fermions. *Phys. Rev. Lett.*, 82(21):4204–4207, 1999.

[73] K. M. O'Hara, S. R. Granade, M. E. Gehm, and J. E. Thomas. Loading dynamics of CO_2 laser traps. *Phys. Rev. A*, 63:043403, 2001.

[74] P. W. H. Pinkse, A. Mosk, M. Weidemüller, M. W. Reynolds, T. W. Hijmans, and J. T. M. Walraven. One-dimensional evaporative cooling of magnetically trapped atomic hydrogen. *Phys Rev. A*, 57(6):4747–4760, 1997.

[75] E. Raab, M. Prentiss, A. Cable, S. Chu, and D. Pritchard. Trapping of neutral sodium atoms with radiation pressure. *Phys. Rev. Lett.*, 59:2631, 1987.

[76] T. A. Savard, K. M. O'Hara, and J. E. Thomas. Laser-noise-induced heating in far-off resonance optical traps. *Phys. Rev. A*, 56(2):R1095, 1997.

[77] R. Scheunemann, F. S. Cataliotti, T. W. Hänsch, and M. Weitz. Resolving and addressing atoms in individual sites of a CO_2 laser optical lattice. *Phys. Rev. A*, 62:051801, 1998.

[78] J. Schuster, A. Marte, S. Amtage, B. Sang, G. Rempe, and H. C. W. Beijerinck. Avalanches in a bose-einstein condensate. *Phys. Rev. Lett.*, 87(17):170404, 2001.

[79] D. Sesko, T. Walker, C Monroe, A. Gallagher, and C. Wieman. Collisional losses from a light-force atom trap. *Phys. Rev. Lett.*, 63(9):961, 1989.

[80] Anthony E. Siegman. *Lasers.* University Science Books., 1986.

[81] D. M. Stamper-Kurn, H. J. Miesner, A. P. Chikkatur, S. Inouye, J. Stenger, and W. Ketterle. Reversible formation of a bose-einstein condensate. *Phys Rev. Lett.*, 81:2194, 1998.

[82] Dan M. Stamper-Kurn. *Peeking and poking at a new quantum fluid: Studies of gaseous Bose-Einstein condensates in magnetic and optical traps.* PhD thesis, MIT, 2000.

[83] S. Stenholm. A semi-classical theory of laser cooling. *Rev. Mod. Phys.*, 58:699, 1986.

[84] J. R. Yeh T. Takekoshi and R. J. Knize. Quasi-electrostatic trap for neutral atoms. *Optics Communications*, 114:421–424, 1995.

[85] R. Taieb, R. Dum, J. I. Cirac, P. Marte, and P. Zoller. Cooling and localization of atoms in laser-induced potential wells. *Phys. Rev. A*, 49(6):4876, 1994.

[86] T. Takekoshi and R. J. Knize. Co_2 laser trap for cesium atoms. *Optics Letters*, 21(1):77–79, 1996.

[87] C. G. Townsend, N. H. Edwards, K. P. Zetie, C. J. Cooper, J. Rink, and C. J. Foote. High-density trapping of cesium atoms in a dark magneto-optical trap. *Phys. Rev. A*, 53(3):1702, 1996.

[88] P. Jeffery Ungar, D. S. Weiss, E. Riis, and S. Chu. Optical molasses and multilivel atoms: theory. *J. Opt. Soc. Am. B*, 6(11):2058, 1989.

[89] T. Walker, D. Sesko, and C. Wieman. Collective behaviour of optically trapped neutral atoms. *Phys. Rev. Lett.*, 64(4):408–411, 1990.

[90] C. D. Wallace, T. P. Dinneen, Kit-Yan N. Tan, T. T. Grove, and P. L. Gould. Isotopic difference in trap loss collisions of laser cooled rubidium atoms. *Phys. Rev. Lett.*, 69(6):897, 1992.

[91] D. S. Weiss, E. Riis, Y. Shevy, P. Jeffery Ungar, and S. Chu. Optical molasses and multilivel atoms: experiment. *J. Opt. Soc. Am. B*, 6(11):2073, 1989.

[92] Carl E. Wieman and Leo Hollberg. Using diode lasers for atomic physics. *Rev. Sci. Instruments.*, 61(1):1–20, 1991.

[93] D. Wineland and W. Itano. Laser cooling of atoms. *Phys. Rev. A.*, 20:1521, 1979.

[94] Steffen Wolf, Steven J. Oliver, and D. S. Weiss. Suppression of recoil heating by an optical lattice. *Phys. Rev. Lett.*, 85(20):4249, 2000.